UNIVERSITÀ
DEGLI STUDI
FIRENZE

International Doctorate in Atomic and Molecular Photonics

CYCLE XXXIII

COORDINATOR Prof. Francesco Saverio Cataliotti

An NV center as an open quantum system - noise spectroscopy and quantum thermodynamics

Academic Discipline (SSD) Fis/03 Fisica della Materia

Supervisor
Dr. Nicole Fabbri

Nicole Fabbri

Doctoral Candidate
Dr. Santiago Hernández Gómez

Co-supervisor
Prof. Paola Cappellaro

Paola Cappellaro

Coordinator
Prof. Francesco Saverio Cataliotti

Years 2017/2020

An NV center as an open quantum system – noise spectroscopy and quantum thermodynamics

by

Santiago Hernández Gómez

Submitted to the European Laboratory for Non-linear Spectroscopy
on December, 2020, in partial fulfillment of the requirements
for the degree of Doctor in Philosophy in
International Doctorate in Atomic and Molecular Photonics

Abstract

The investigation of open quantum systems is extremely wide-ranging and permeates fields as diverse as condensed matter physics, quantum optics, and quantum computation, with the goal of understanding the foundations of decoherence and advancing the performance of quantum-based technologies. A precise knowledge of the interaction of a quantum system with its environment is a crucial prerequisite to effectively hinder the detrimental effect of decoherence via selective decoupling, or to gain partial or full control of the environment itself, enabling complex information transfer and storage protocols that involve entanglement. These techniques represent an asset for the realization of quantum-enhanced devices. However, studying the coupling between a quantum system and its (classic or quantum) environment is often limited by the same lack of information and control that inspires the study in the first place. Thus, a quantum system that is highly controllable and that can be used to gain information on the environment constitutes an attractive tool to approach these problems.

This thesis tackles these challenges by exploiting the Nitrogen-Vacancy (NV) center in diamond, which is an ideal candidate for many quantum technologies. The NV center has emerged as a prominent platform to realize quantum-enhanced sensors with unprecedented combination of high sensitivity and spatial resolution at room temperature. In addition, its outstanding spin properties and optical addressability make the NV center an ultra stable quantum platform with tunable interaction with its environment.

This thesis addresses two complementary objectives: develop quantum control protocols of the NV spin dynamics to accurately characterize the NV environment, and develop new tools to investigate the thermodynamics aspect of the spin dynamics in contact with an engineered energy reservoir.

Part I presents a quantum control protocol designed to spectrally characterize the complex environment of a NV spin qubit, which can be applied even in the case of relatively short coherence times. Specifically, we test this method on the nuclear spin environment of an NV center in bulk diamond, composed by single nuclear spins coherently coupled with the NV spin, and a larger nuclear spin-bath that collectively induce dephasing on the NV spin qubit. The applied control is capable of partially decoupling the system from its environment, hence allowing to selectively characterize the strength of each of the noise components. In addition, the environment behavior can be tuned by the amplitude of an external bias magnetic field. In the weak coupling regime, i.e., for a relatively high bias field, the coupling with the spin-bath can be modeled as a classical stochastic field. With the proposed protocol we were able to identify the local spin environment, and to reconstruct the noise spectral density associated with the spin bath, in spite of the strong decoherence it induces in the system. Critically for quantum sensing applications, we proved that the spin qubit dynamics can be predicted by the reconstructed noise model, even under quantum control sequences that differ from the ones used for the spectral noise characterization. At lower bias fields, the quantum nature of the bath is more pronounced. In this strong coupling regime, the spin-bath dynamics depends on the quantum control applied to the NV spin. Although less commonly present in quantum sensing applications, the study of this regime is important from a fundamental point of view. In this case we have found that at least two different classical noise models are needed to properly describe the spin coherence, depending on the kind of quantum control.

The second part of this thesis is dedicated to the study of energy exchange mechanisms for an open quantum system in the framework of quantum fluctuation relations. As a novel toolbox in this field, we used the NV center spin subject to trains of short laser pulses to investigate the interplay of externally-applied quantum measurements and internal dissipative dynamics, under which the system asymptotically approaches to a non-thermal stationary state. The quantum measurements and the tunable dissipation channel stem, respectively, from spin-preserving optical transitions and from optical pumping of the spin, both caused by the interaction with short laser pulses. In addition, the spin is coherently driven by on resonance microwave radiation that defines the Hamiltonian of the system, generating the so-called dressed states. First, we have studied the case of a spin qubit, where our experimental results, supplemented by numerical simulations, show the validity of the energy exchange fluctuation relation. This demonstrates that the quantum dissipative map emulates the interaction with an effective thermal reservoir, with a pseudo-temperature defined by the properties of the fixed point of the dissipative map. Then we have extended our research to the case of a three level quantum system, a spin qutrit. In such case, the dissipative map can no longer be associated with effective thermalizing dynamics. Instead, we demonstrate that the map can be modeled as an intrinsic feedback process, where different Lindbladian dynamics are applied to the system depending on the result of a quantum measurement. We experimentally demonstrate the validity of a generalized version of the quantum Jarzynski-Sagawa-Ueda relation, involving irreversible non-thermal dissipative dynamics. As for the qubit case, the three level quantum system asymptotically approaches to an out-of-equilibrium steady state as a result of the dissipative map. We proved, experimentally and in theory, that this feature of the dissipative quantum dynamics gives origin to an energy exchange fluctuation relation, where a unique energy scale factor (macroscopic parameter) is defined in terms of the system initial and steady out-of-equilibrium asymptotic states. These findings pave the way to the investigation of energy exchange mechanisms in arbitrary open quantum systems.

The methods and results obtained in this thesis can be beneficial for the realization of different quantum devices, such as quantum sensors and quantum thermal machines. More broadly, they can find applications in different experimental quantum settings, ranging from quantum gases, to superconductive qubits, and ions.

Contents

List of Figures

List of Tables

Introduction

Color centers in diamond — optically-active point defects — have emerged in the last decade as notable platform for quantum technologies. Among color centers, the negatively charged Nitrogen-Vacancy (NV) center [1, 2] has stood out as a solid-state spin qubit thanks to a high degree of coherent control, ultra-long spin coherence time, remarkable fluorescence photostability, as well as optical addressability, initialization and readout, all of which can be achieved at room temperature [3–7]. The wide range of applications for NV centers includes its use for quantum memories [8, 9]; biocompatible quantum sensors [10, 11] of magnetic and electric fields [12, 13], temperature[14, 15], rotation [16], strain and pressure [17]; and very recently as a platform to study quantum thermodynamics [18, 19], among others. The spin qubit, formed by the NV center ground state, has remarkably long lifetime compared to any other solid-state platform, with longitudinal relaxation times $T_1 \sim 6$ ms at room temperature and $T_1 \sim 1$ s at cryogenic temperature ($T = 77$ K) [6, 20]. This long-lived spin system, protected by the diamond lattice, represents an outstanding platform to be used as a spin-based quantum magnetometer capable of detecting nuclear spin clusters [21, 22] or even single nuclear spins [23–25].

In this thesis, a single NV center in diamond is used as an open quantum system in order to characterize the interaction with its environment.

Quantum sensing

NV centers have proven to be powerful magnetometers, capable of measuring very localized ultra weak AC fields, achieving sensitivities of the order of $\mathrm{pT}/\sqrt{\mathrm{Hz}}$ with ensemble devices [14, 26] in ambient conditions. However, as for any other practical device, the operation of NV-based quantum sensor is prone to limitations and imperfections: The high sensitivity to the magnetic environment makes NV spins very precise sensors, but the same interaction with the environment constitutes also a limit to the device sensitivity by reducing the coherence of the quantum states [27]. Characterizing the interaction of the NV spin with its environment is therefore critical to realize a robust quantum device: A full understanding of the qubit environment enables the development of effective strategies against decoherence, including optimized dynamical decoupling (DD) sequences [28–30] and quantum error correction codes [31]. Moreover, part of the environment — such as close-by nuclear spins — may display a coherent coupling to the qubit and thus provide an additional resource to enhance sensing performance [32–34].

The first part of this thesis [Part I] is dedicated to the development of a quantum control (QC) protocol that can unravel the characteristics of a complex environment, comprising both unknown coherently coupled quantum systems, and a larger quantum bath. This study shows that the acquired knowledge of the bath can be used to reliably predict the qubit dynamics even under drivings that differ from the ones used for noise spectroscopy, an essential feature for quantum sensors.

Quantum thermodynamics

The high degree of control and optical addressability make the NV spin a useful platform also to address fundamental open research questions. The connection between statistical properties of out-of-equilibrium dynamical systems, thermodynamics quantities and information theory has been deeply investigated in classical and quantum systems and codified in terms of fluctuation relations (FRs) [35–41]. However, in open quantum systems, despite several contributions [42–47], such connection is far from being completely understood, especially regarding the competition between thermal and quantum fluctuations. The latter assumes a paramount role at the nanoscale, for example, for developing quantum thermal engines [18, 48] or studying information–energy conversion [49, 50].

The experimental study of quantum fluctuation relations requires a high degree of control on the quantum system, long enough coherence time to detect the system dynamics, and possibly a partially controlled reservoir to put the system in contact with. These requirements impose several difficulties, even in the case of closed quantum systems only a small set of different platforms have been used to verify FRs, ranging from single ions [51–53], superconducting qubits [54], ensemble of cold atoms/atom chip [55], and liquid-state nuclear magnetic resonance setups [56].

The study of FRs for open quantum systems is even more challenging. At the best of my knowledge, this kind of studies have only been done with liquid-state nuclear magnetic resonance setups [57] and with an NV center in diamond [19, 58]. The latter corresponds to the research presented in the second part of this thesis [Part II], where we use the orbital ground state of an NV center as a spin qubit or qutrit to investigate the energy exchange mechanisms with an engineered non-thermal reservoir, by reconstructing the characteristic function [59] of the energy variation along the thermodynamic process. The interaction between this quantum system and the reservoir is conditioned to the presence of short laser pulses, that act as projective measurements followed by an irreversible optical pumping mechanism, that is treated as a dissipation channel. The combined effect of projective measurements and dissipation can create or destroy quantum coherence during the system dynamics, an effect that goes beyond the classical description. Moreover, they induce irreversible dissipative dynamics on the quantum system, that cannot be described as classical thermalizing dynamics. Exploiting the NV center as a spin qubit, we have found that this dissipative map is equivalent to putting the system in contact with a pseudo-thermal reservoir, hence the exchange fluctuation relation correctly describe the statistics of the energy variation. When employing all the three ground-state NV spin projections as a spin qutrit, the analogy of pseudo-thermal states is no longer valid. To correctly describe the experimental findings, it was necessary to find a generalization of the existing FRs. In particular we extended the Jarzynski-Sagawa-Ueda relation – originally devised for closed systems subject to a conditioned unitary dynamics — to a conditioned dissipative dynamics.

Our results establish the NV center as an ideal platform for quantum thermodynamics.

Contents of this thesis

Chapter 1 is an introduction to the main properties of an NV center in diamond, and to how this experimental platform can be used as a highly controllable quantum system. After this introductory chapter, the thesis is divided in two parts.

Part I of the thesis is dedicated to the spectral characterization of the spin environment of a single NV center, formed by the nuclear spin of carbon-13 impurities in the diamond.

In Chapter 2, we present a quantum control (QC) protocol for the NV qubit spin that can unravel the characteristics of this complex environment. This is achieved by characterizing the interaction with coherently coupled nearby nuclear spins, and with a larger spin bath.

Part II: Quantum thermodynamics

The second part of this thesis is devoted to the study of energy exchange fluctuation relations for non-thermal dissipative dynamics using as a quantum system the orbital ground state of an NV center. Chapter 3 introduces the formalism of fluctuation relations (FR), and the main concepts and tools used to understand how to experimentally test FRs. Chapter 4 describes the use of a single NV center subject to trains of short laser pulses, to realize a two-level quantum system under stochastic-dissipative dynamics. The action of laser pulses on the NV spin realize quantum projective measurement accompanied by a partial optical pumping that realizes in practice a dissipation channel, effectively described as the contact with a pseudo-thermal reservoir. In this Chapter, I present also the experimental measurement of the characteristic function of the energy variation that occurs during the induced thermodynamic process, which enables the first demonstration of the energy exchange fluctuation relation for an open quantum system. The content of this chapter (Ch. 4) has been partially published in Ref. [19].

Whilst two-level systems grant the possibility of studying pseudo-thermal states, a quantum system with higher dimension provides an ideal playground towards the study of non-thermal dissipative dynamics. In Chapter 5 we will use the orbital ground state of the NV center as a three-level quantum system, in order to gain more insight on how to characterize the dynamics induced by dissipative non-thermal dynamics. We will propose, and demonstrate the validity of two different FRs that correctly describe this quantum dissipative map, both of which are generalizations of previously known FRs.

Acronyms

$\mu-$**pos**	Micropositioner (translation stage)
AXY-N	Adaptive XY-N (dynamical decoupling sequence)
CP	Carr-Purcell (dynamical decoupling sequence)
DD	Dynamical decoupling
ESR	Electron spin resonance
FFT	Fast Fourier transform
FR	Fluctuation relation
FT	Fluctuation theorem
FWHM	Full width half maximum
JSU	Jarzynski-Sagawa-Ueda (fluctuation relation)
G-JSU	Generalized Jarzynski-Sagawa-Ueda (fluctuation relation)
mw	Microwave
n$-$**pos**	Nanopositioner (translation stage)
NMR	Nuclear magnetic resonance
NSD	Noise spectral density
NV	Nitrogen vacancy
PL	Photo-luminescence
POVM	Positive-operator valued measure
QC	Quantum control
QFR	Quantum fluctuation relation
QFRHE	Quantum fluctuation relation for heat engines
rf	Radio-frequency
RNG	Random number generator
RUM	Random unitary map
SE	Spin-echo
SPD	Single photon detector
SSE	Stationary state in the energy basis
UDD	Uhrig dynamical decoupling (dynamical decoupling sequence)
ZFS	Zero-field-splitting

List of publications

This is a list of the publications originated from the research developed during my three year PhD. The publications are listed in chronological order.

1. S. Hernández-Gómez, F. Poggiali, P. Cappellaro, and N. Fabbri, Noise spectroscopy of a quantum-classical environment with a diamond qubit, Phys. Rev. B 98, 214307 (2018).

2. S. Hernández-Gómez, F. Poggiali, P. Cappellaro, and N. Fabbri, in *Quantum Nanophotonic Materials, Devices, and Systems 2019*, Vol. 11091, International Society for Optics and Photonics (SPIE, 2019) pp. 31 – 39.

3. F. Poggiali, S. Hernández-Gómez, P. Cappellaro, and N. Fabbri, in *Quantum Information and Measurement (QIM) V: Quantum Technologies* (Optical Society of America, 2019) p. S3C.2.

4. S. Hernández-Gómez, F. Poggiali, P. Cappellaro, and N. Fabbri, in *Proceedings of the International School of Physics "Enrico Fermi"*, Vol. 204, Societa' Italiana di Fisica (IOS Press, 2020) pp. 245 – 249, research article.

5. S. Hernández-Gómez, S. Gherardini, F. Poggiali, F. S. Cataliotti, A. Trombettoni, P. Cappellaro, and N. Fabbri, Experimental test of exchange fluctuation relations in an open quantum system, Phys. Rev. Research 2, 023327 (2020).

6. S. Hernández-Gómez and N. Fabbri, Quantum Control for Nanoscale Spectroscopy With Diamond Nitrogen-Vacancy Centers: A Short Review, Frontiers in Physics 8, 652 (2021)

7. S. Hernández-Gómez, N. Staudenmaier, M. Campisi, and N. Fabbri, Experimental test of fluctuation relations for driven open quantum systems with an NV center, arXiv:2103.03904 [quant-ph] (2021).

8. S. Hernández-Gómez, S. Gherardini, N. Staudenmaier, F. Poggiali, M. Campisi, A. Trombettoni, P. Cappellaro, F. S. Cataliotti, and N. Fabbri, Nonthermal energy fluctuations of a diamond spin qutrit with feedback-controlled dissipative dynamics (*in preparation*).

Chapter 1

An introduction to NV centers: Properties and experimental implementation

The main goal of this chapter is to present the necessary bases to understand how to use the electronic spin of an NV center in diamond as an experimental platform to study quantum phenomena. Section 1.1 is dedicated to present the NV center energy level structure and its optical properties, as well as to describe how to interact with and manipulate its ground spin triplet state. In section 1.2 I provide a concise description of the experimental setup, and discuss in more detail the implementation of a versatile microwave system to control the NV electronic spin dynamics, entailing amplitude and phase modulation. At this point, the description of some basic experiments together with their results are included in section 1.3, to set the necessary bases for more complex experiments described in the following Chapters. The last two sections are devoted to present a detailed protocol to align the external bias magnetic field with the NV center quantization axis [Sec. 1.5], and to characterize the NV center photodynamics [Sec. 1.4] via numerical solution of the master equation that describes the interaction of the NV center with a green laser.

1.1 Nitrogen-vacancy centers overview

The NV center is formed by a substitutional nitrogen atom adjacent to a vacancy in the diamond lattice with C_{3v} symmetry around one of the four [111] crystallographic directions, as schematized in Fig. 1.1(a). Among the three possible charge states (NV^- , NV^0 , and NV^+), the negatively charged NV^-—hereafter referred to as NV for simplicity—is the most widely investigated for quantum technology applications, thanks to its favorable internal energy structure and photophysics [2], which enable optical initialization and readout, and coherent manipulation with long coherence time, as discussed below.

The NV energy structure, shown in Fig. 1.1(b), consists in electronic orbital ground (${}^3A_2$) and excited (${}^3E$) triplet levels separated by 1.945 eV, and two intermediate ${}^1E$ and ${}^1A_1$ singlet levels [2]. At room temperature, the triplet ground-state population —distributed according to Maxwell-Boltzmann distribution into the three spin projections $m_S = 0, \pm 1$— can be transferred to the excited levels by irradiation of the center with green laser (532 nm) though a process involving a combination of radiative absorption and non-radiative relaxation processes that also entails vibronic bands. A direct spin-preserving radiative decay from the excited to

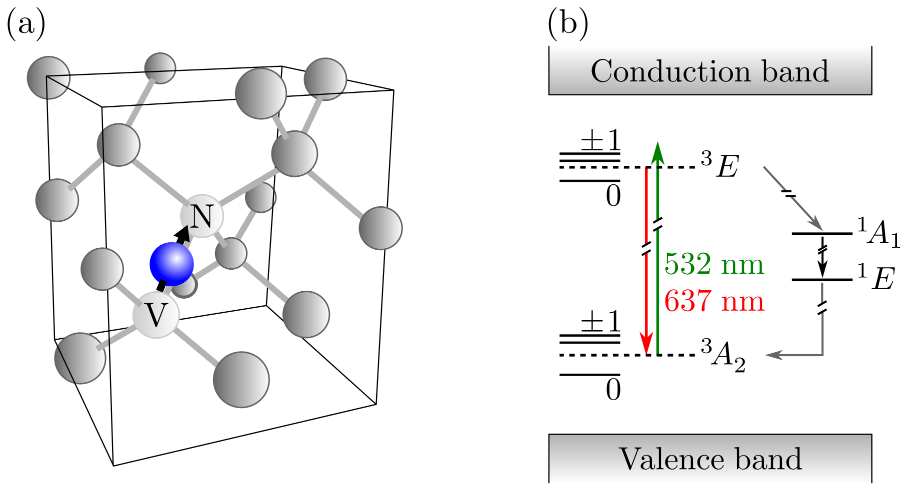

Figure 1.1: **(a)** Scheme of the diamond lattice structure holding an NV center. **(b)** Energy level structure of the NV center.

the ground level (with zero-phonon-line of 637-nm wavelength) is accompanied by non-radiative non-spin-preserving decay through the long-lifetime singlet levels $^1A_1$ and ^1E (see Fig. 1.1(b)). The different decay rates for the different spin projections in the non-radiative decay channel yield the optically initialization of the system into the $m_S = 0$ state of the ground level. The same decay mechanism enables spin state readout thanks to different photoluminescence intensities of the $m_S = 0$ and $m_S = \pm 1$ states. A detailed description of the NV center photodynamics, together with a numerical model based on solving a Lindbladian master equation, can be found in Sec. 1.4.

1.1.1 Spin Hamiltonian

The electron spin of the NV ground state (which is not affected by spin-orbit coupling), in the presence of an external magnetic field, is mainly influenced by spin-spin interaction and electron Zeeman shift. The ground-state spin Hamiltonian reads

$$\mathcal{H}_{(S)} = \mathbf{S} \cdot \mathbf{D} \cdot \mathbf{S} + \gamma_{\mathrm{e}} \mathbf{B} \cdot \mathbf{S} \tag{1.1}$$

where $\mathbf{B}$ is the external bias magnetic field, $\mathbf{D}$ is the spin-orbit interaction tensor (or zero-field splitting tensor) that depends on the symmetry of the crystal field [60], and γ_e is the electronic gyromagnetic ratio. For simplicity from now on, unless explicitly stated, we assume $\hbar = 1$. The tensor $\mathbf{D}$ is symmetric by definition, hence the first term in the spin Hamiltonian can be rewritten as $\mathbf{S} \cdot \mathbf{D} \cdot \mathbf{S} = D_x S_x^2 + D_y S_y^2 + D_z S_z^2$ [60]. For the orbital ground state of an NV center in diamond $D_{\mathrm{g}} \equiv D_z \simeq 2.87$ GHz, and the other two tensor elements, D_x and D_y, can be neglected [61]. The electronic spin-spin interaction within the NV separates the energy of $m_S = 0$ from the degenerate $m_S = \pm 1$ within the ground-state, with zero-field-splitting (ZFS) D_{g}. On the other hand, the static bias magnetic field removes the degeneracy of levels $m_S = \pm 1$ and modifies their energies via Zeeman effect. In addition, hyperfine interaction with the nitrogen nuclear spin $\mathbf{I}$ induce further splitting of each electronic spin state. In all the cases used during this study the nitrogen atom forming the NV center was an isotope ^{14}N, with $I = 1$. The ^{14}N nuclear quadrupole moment $Q = 4.945$ MHz [62–66] together with the external static bias magnetic field remove the degeneracy of the nuclear spin projections $m_I = 0, \pm 1$, while the hyperfine interaction between the electronic and nuclear spins is ruled by the tensor $\mathbf{A}$. All this is summarized into the NV center ground level ($^3A_2$) Hamiltonian

$$\mathcal{H}_{\mathrm{g}} = D_{\mathrm{g}} S_z^2 + \gamma_{\mathrm{e}} \mathbf{B} \cdot \mathbf{S} + Q I_z^2 + \gamma_{\mathrm{n}} \mathbf{B} \cdot \mathbf{I} + \mathbf{S} \cdot \mathbf{A} \cdot \mathbf{I} \tag{1.2}$$

where the last three terms are associated with the hyperfine structure. In this equation $\gamma_n = 0.308$ kHz/G is the gyromagnetic ratio of the ^{14}N nucleus. In the experiments described in this thesis, the external bias magnetic field $\mathbf{B}$ is aligned with the electronic spin quantization axis, determined by the symmetry axis of the NV center, in which case $\mathbf{B} = B_z \hat{\mathbf{z}}$. See Sec. 1.5 for details on the procedure used to align the field in the experiment. The hyperfine interaction term in Eq. (1.2) can be separated into the parallel and orthogonal components

$$\mathbf{S} \cdot \mathbf{A} \cdot \mathbf{I} = A_{\parallel} S_z I_z + A_{\perp} \left(S_x I_x + S_y I_y \right) \tag{1.3}$$

where $A_{\parallel} = -2.16$ MHz [63, 64] and $A_{\perp} = 2.62$ MHz [67].

Introducing the notation E_{m_S,m_I} for the energy of the state $|m_S, m_I\rangle$, then the energy difference between the $m_S = 0$ and one of the $m_S = \pm 1$ states for a given m_I is

$$\Delta E_{m_I}^{(\pm)} = E_{\pm 1, m_I} - E_{0, m_I} = D_{\mathrm{g}} \pm \gamma_{\mathrm{e}} B_z \pm A_{\parallel} m_I. \tag{1.4}$$

A microwave (mw) excitation can be used to selectively address one of these transitions, which can be monitored via the photoluminescence readout. An example of this is shown in Fig. 1.2, where the photoluminescence (PL) intensity is plotted in terms of the mw frequency in order to observe each of the possible electronic spin transitions in the NV center ground state. More details on this kind of measurement will be discussed in Sec. 1.3.2.

Therefore, the two level systems $\{|0, m_I\rangle, |\pm 1, m_I\rangle\}$ that can be coherently driven and optically initialized and readout, fulfills all the requirements to be used as a qubit. In the presence of a continuous near-resonance microwave excitation, the spin Hamiltonian in the mw rotating frame that describes the dynamics of this qubit is

$$\mathcal{H}_{\Omega,\delta} = \frac{1}{2} \left(\Omega \sigma_x + \delta \sigma_z \right) \tag{1.5}$$

where Ω is the Rabi frequency, δ is the mw detuning with respect to the transition, and $\sigma_{x,z}$ are the Pauli matrices. This Hamiltonian will be useful to describe the mw-induced qubit gates realized in the experiments presented in this thesis.

1.2 Experimental setup

In this section we briefly describe the experimental setup used for the control of NV centers in diamond at room temperature. More details can be found in Ref. [68]. A simplified scheme of the used experimental setup is shown in Fig. 1.3(a). The experiment is controlled using a Matlab-based control code.

A single deep NV center is found inside an electronic-grade bulk diamond (Element6), with nitrogen concentration [^{14}N] < 5 ppb. The NV center is optically addressed at ambient conditions with a home-built scanning confocal microscope. The excitation light is a green laser that induces a transition from the ground to the excited level. For the experiments described in this thesis, the green light source shall be able to generate pulses ranging from nanoseconds to microseconds. During the first half of the present work, this was achieved using a cw laser and an AOM,

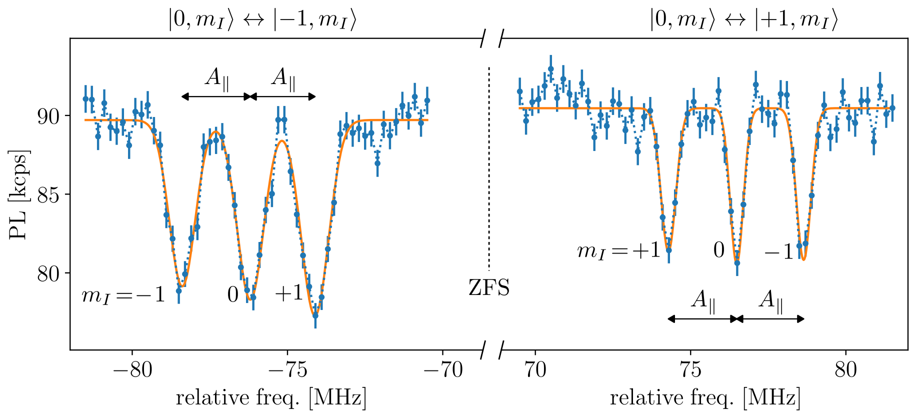

Figure 1.2: Experimental spectrum showing the microwave induced transitions $|0, m_I\rangle \longrightarrow |\pm 1, m_I\rangle$ for each of the different hyperfine levels of a single NV center formed with a ^{14}N isotope. The vertical scale shows the photoluminescence (PL) intensity in kilo-counts-per-second (kcps), while the horizontal axis represents the mw frequency relative to the ZFS. The different width and depth of the transition lines in the left-hand-side ($m_S = -1$) and right-hand-side ($m_S = +1$) graphs is caused by a variation in the emission efficiency of the antenna, delivering the mw, in terms of the mw frequency, hence resulting in a different power broadening of the transition lines. During this experiment, the amplitude of the external magnetic field was $B_z \simeq 27.2$ G.

as described in Ref. [68]. During the last year of the present work, we used a diode laser[1] that can be modulated in intensity with an external trigger, reaching pulses as short as a couple of nanoseconds, with rise/fall times < 2 ns. This laser is controlled by a Marker signal output of an Arbitrary Waveform Generator[2] (AWG).

The fluorescence emitted by the NV is collected by the second objective of the confocal microscope and sent to a single photon detector (SPD). A dichroic mirror allows the transmission of the red light, while reflecting the green light. A band pass filter removes the remaining transmitted green light. The SPD voltage is registered with a DAQ card.

A static bias magnetic field is generated with a permanent magnet, that is fixed to a rotatory mount which in turn is mounted on an XYZ Translation Stage[3]. The magnetic field strength at the NV center position is mainly tuned by moving the magnet in the Z-direction. To align the magnetic field with the spin quantization axis it is necessary to move the X- and Y-direction of the stage, and the rotatory mount. More details about this are present in section 1.5.

The diamond is mounted on an XYZ translation stage (nanopositioner) for fine movements to locate and track single NV centers, and on an XY translation stage (micropositioner) to move to different regions of the diamond.

1.2.1 Spin driving

The NV electronic spin can be controlled with near-resonant microwave (mw) radiation. The frequency, phase and amplitude of the mw defines the specific driving

---

[1] DLnsec 520 nm, *LABS-electronics*.

[2] AWG5000, *Tektronix*.

[3] PT3A/M, *Thorlabs*.

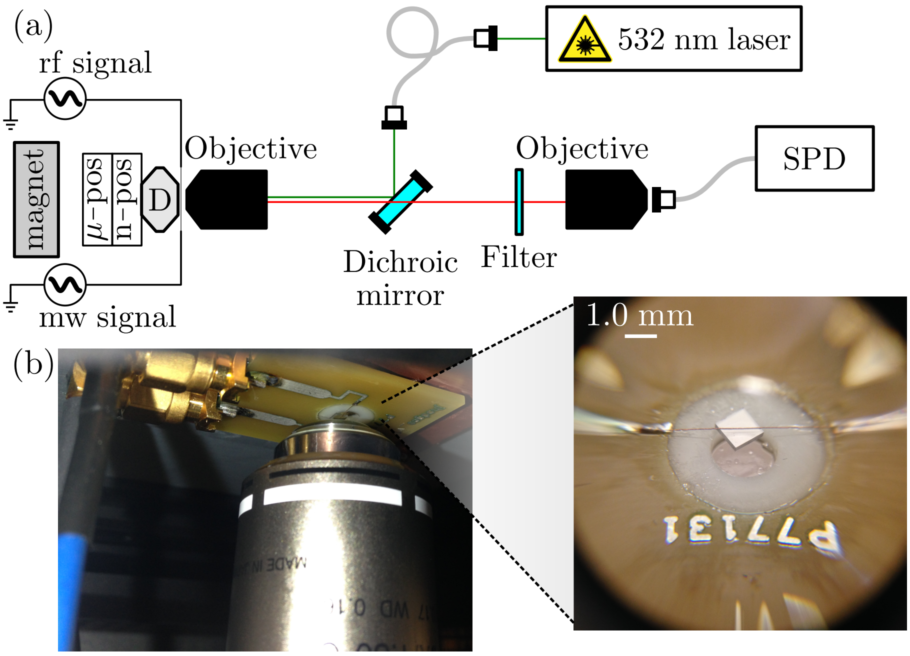

Figure 1.3: Experimental setup. **(a)** Simplified scheme of a room temperature NV experimental setup for single NVs. The NV centers are optically addressed by a confocal microscope, while its electronic spin and nearby nuclear spins are driven by mw and rf excitation, as explained in the text. The diamond (D) is mounted on a nanopositioner (n−pos) and a micropositioner (μ−pos). **(b)** Photograph of the diamond mounted on the translation stage, above the microscope objective. In the zoomed photo, the copper wire (antenna) on top of the diamond is visible.

applied to the NV spin (see also Eq. (1.5)). In a similar fashion, radiofrequency (rf) radiation can be used to coherently drive the nitrogen nuclear spin [Eq. (1.3)].

In the experiment, an antenna placed in proximity of the diamond chip, see Fig. 1.3(b), delivers on-resonant or near-resonant mw and rf radiation. The rf is directly generated from an analog output of the AWG. The mw frequency is generated with a signal generator[4] (SG), and modulated with two analog outputs of the AWG.

The SG has an In-phase Quadrature (IQ) modulation option, where the output signal is the result of combining two signals with the same frequency but with a $\pi/2$ phase difference, each one modulated with the I and Q input signals. Assuming that the SG frequency is set to be $\omega_1/2\pi$, the amplitude of the input I signal is $A(t)$, and the amplitude of the input Q signal is $B(t)$, then the final output is $IQ(t) = A(t)\sin\omega_1 t + B(t)\sin(\omega_1 t + \pi/2) = A(t)\sin\omega_1 t + B(t)\cos\omega_1 t$. This means that, if we apply an amplitude modulation such that $A(t) = \frac{a+b}{2}\cos(\omega_2 t - \phi)$ and $B(t) = \frac{a-b}{2}\sin(\omega_2 t - \phi)$, then the SG output signal will be

$$IQ(t) = \frac{a}{2}\sin((\omega_1 + \omega_2)t - \phi) + \frac{b}{2}\sin((\omega_1 - \omega_2)t + \phi). \tag{1.6}$$

This expression is quite useful because it allows to easily set the effective frequency of the modulated signal. For example:

- Summing frequency: $\phi = 0$, $a = 2$, and $b = 0$ implies $IQ(t) = \sin(\omega_1 + \omega_2)t$.
- Frequency difference: $\phi = 0$, $a = 0$, and $b = 2$ implies $IQ(t) = \sin(\omega_1 - \omega_2)t$.
- Balanced bi-chromatic signal: $\phi = 0$, $a = 1$, and $b = 1$ implies $IQ(t) = \frac{1}{2}\left(\sin(\omega_1 + \omega_2)t + \sin(\omega_1 - \omega_2)t\right)$.
- Unbalanced bi-chromatic signal: $\phi = 0$, $a \neq b$, $a \neq 0$, and $b \neq 0$ implies $IQ(t) = \frac{a}{2}\sin(\omega_1 + \omega_2)t + \frac{b}{2}\sin(\omega_1 - \omega_2)t$.

In addition, the global phase of the output can be controlled. For example, assuming $\omega_2 = 0$, and $b = 0$, if a Pauli-X gate is applied with phase ϕ, then a second similar pulse with phase $\phi + \pi/2$ would correspond to a Pauli-Y gate.

Notice that the I and Q input signal amplitudes must be selected carefully to ensure that their sum in quadrature is $\sqrt{A^2(t) + B^2(t)} \leq 0.5$ V. This is because the SG output amplitude is $A_{\mathrm{SG}}\sqrt{A^2(t) + B^2(t)}/(0.5\ \mathrm{V})$, where A_{SG} is the SG preset amplitude. In addition, the AWG analog output operation frequency range is DC-130 MHz, this means that $\omega_2/2\pi \leq 130$ MHz.

1.3 Spin control via magnetic resonance: basic experiments

This section introduces the basic magnetic resonant techniques that are at the basis of all the experiments involving the NV spin and that are routinely used to precalibrate the electronic quantum gates.

As explained in Sec. 1.1, the electronic spin qubit can be coherently driven with a near-resonant field (see Eq. (1.5)). A very powerful tool to understand the

---

[4] SG384, *Stanford Research Systems.*

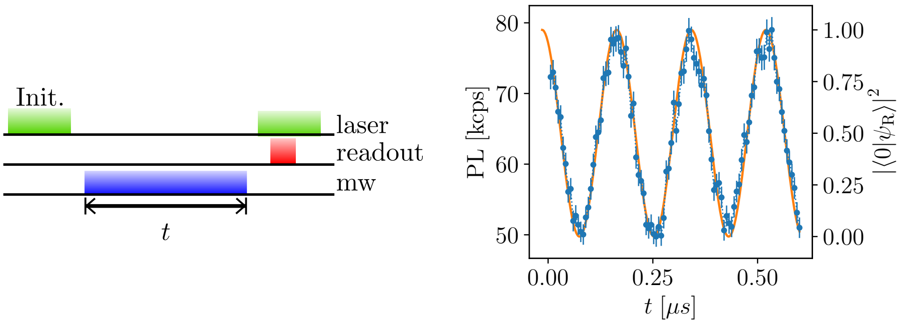

Figure 1.4: Rabi experiment. **(a)** Rabi experiment sequence scheme. **(b)** The measured photoluminescence (PL) intensity (blue circles) is plotted in terms of the microwave pulse duration. A cosine function is fitted to the data (solid line), and the frequency obtained as a result of the fit corresponds to the Rabi frequency. In this particular dataset, the Rabi frequency was approximately 5.62 MHz.

dynamics of the driven two level system is the so called Bloch sphere, which is a three dimensional representation of the state of a qubit. The points resulting from the intersection of the sphere with each of the X,Y,Z axis represent respectively the eigenstates of the operators $\sigma_x, \sigma_y, \sigma_z$. Any pure state of the qubit is represented as a point in the sphere surface. The unitary evolution of a state, consequence of a given Hamiltonian (written as a sum of Pauli matrices) corresponds to a rotation on the Bloch sphere along the direction defined by the Hamiltonian eigenstates.

1.3.1 Rabi experiment

In order to apply quantum operations, or quantum gates, to the qubit spin, it is necessary to characterize how fast the system is driven by mw control field. This is achieved by measuring the Rabi oscillations.

In the presence of on-resonance mw radiation, the qubit spin rotates around a direction orthogonal to the quantization axis. Due to the symmetry of the spin, we can assume without loss of generality that the rotation axis is σ_x [Eq. (1.5)]. Hence, by changing the duration of the mw driving, and measuring the residual population of the $|0\rangle$ state, one can observe a coherent oscillation, also known as Rabi oscillation. An example of this is shown in Fig. 1.4. The acquired data corresponds to the PL intensity as a function of the duration of the mw driving. This data is normalized with respect to the PL intensity of the $m_S = 0$ state and the $m_S = -1$ state, to obtain the residual population of the $|0\rangle$ state $|\langle 0|\psi_\mathrm{R}\rangle|^2$, with $|\psi_\mathrm{R}\rangle = e^{-i\Omega t \sigma_x}|0\rangle$ being the resulting state after applying a unitary evolution operator to the initial state $|0\rangle$, where Ω corresponds to the Rabi frequency (see Eq (1.5)). The Rabi frequency is obtained by fitting a cosine function to the normalized data. The duration of a π pulse is half an oscillation period, the duration of a $\pi/2$ pulse is one-quarter of an oscillation period, and so on.

1.3.2 Electron spin resonance (ESR)

The most basic scheme to measure the frequency of the transition $|0\rangle \rightarrow |1\rangle$ is the electron spin resonance (ESR). In NV setups, ESR can be detected optically (ODMR), by measuring the photoluminescence intensity while a frequency-tunable

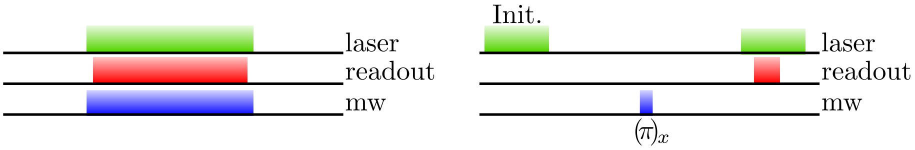

Figure 1.5: Pulse sequence scheme for the ESR experiment. **(a)** Continuous-wave ESR sequence scheme, and **(b)** pulsed ESR sequence scheme.

mw radiation addresses the NV center. The protocol consists in simultaneously applying a long laser pulse and an equally long mw pulse, as shown in Fig. 1.5(a), this technique is called "continuous-wave ESR" (CW-ESR). During this time, the PL intensity is constantly registered by the SPD. When the mw frequency matches the desired transition, the qubit performs Rabi oscillations, resulting in a reduction of the PL intensity to approximately half of the amplitude of the oscillations shown in Fig. 1.4.

In order to increase contrast, it is possible to use a pulsed ESR sequence. This sequence consists in a long laser to initialize the system into $|0\rangle$, followed by a π pulse, and finally applying a second laser and a PL readout. The contrast is increased with respect to the continuous-wave ESR, because, when the mw frequency matches the desired transition, instead of averaging in time the signal from the Rabi oscillations, the PL readout will take place when all the population has been transferred into $|1\rangle$. Note that, in order to maximize the contrast, it is necessary to apply a π pulse, hence we are required to know beforehand the correct mw pulse duration and amplitude. This is achieved by previously performing Rabi experiment.

The sequence of pulses to perform both, the continuous-wave and the pulsed ESR experiments are shown in Fig. 1.5. An example of a pulsed ESR experiment was already shown in Fig. 1.2.

1.3.3 Ramsey experiment

In order to improve the resolution when measuring the central frequency of the fine and hyperfine transitions, we use a Ramsey experiment. Ramsey interferometry was design to measure the phase acquired by a two-level quantum state, a quantity that is not directly measurable, in contrast with the probability of being in each state, as it is the case of the ESR experiment. The acquired phase carries enough information to estimate the frequency of one, or more induced transitions.

The sequence is the following: after initializing the system into the $m_S = 0$ state ($|0\rangle$), a $\pi/2$ pulse is applied, creating a perfect superposition of states $\frac{1}{\sqrt{2}}\left(|0\rangle + |1\rangle\right)$, where $|1\rangle$ can be any of the $m_S = \pm 1$ states. During a free evolution period t, the qubit interacts with the external bias field. Hence, during this time the state $|1\rangle$ acquires a phase ϕ_t with respect to the state $|0\rangle$, resulting in a state $\frac{1}{\sqrt{2}}\left(|0\rangle + e^{i\phi_t}|1\rangle\right)$. After this, a second $\pi/2$ pulse is applied. The final state is then written, ignoring a global phase, as $|\psi_{\mathrm{R}}\rangle = \cos\frac{\phi_t}{2}|1\rangle \pm i\sin\frac{\phi_t}{2}|0\rangle$. In this way, reading out the final state probability of being in $m_S = 0$, we measure the phase ϕ_t. The scheme of the pulse sequence is shown in Fig. 1.6(a).

By repeating the experiment for different t values, we observe a damped coherent oscillation, as the one shown in Fig. 1.6(b). The detrimental noise caused by the interaction with the environment imposes a random phase on the qubit, hence damping the oscillations. The main source of this detrimental noise comes from

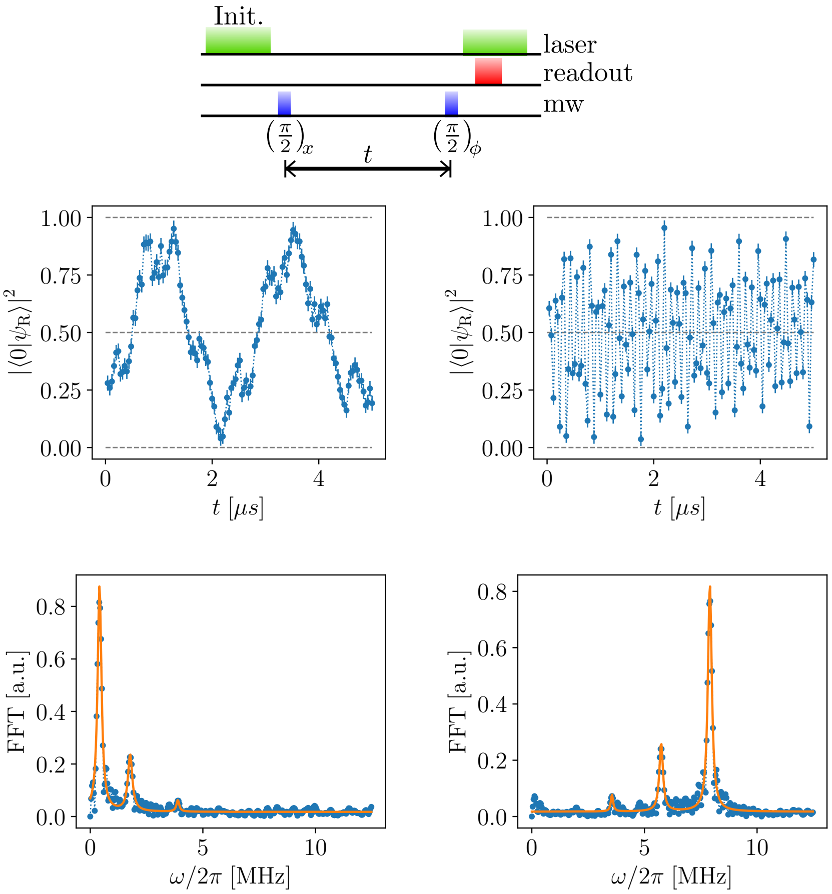

Figure 1.6: Ramsey interferometry experiment. **(a)** Sequence scheme. The phase of the second $\pi/2$ pulse can be fixed to match that of the first pulse, or it can change in time to add an offset to the frequency components of the acquired signal (see text). **(b)** Example of the results from a Ramsey interferometer. In this case the second $\pi/2$ pulse had zero phase with respect to the first pulse ($\phi = x$). **(c)** Example of the results from a Ramsey interferometer with a phase modulation $\phi(T) = \nu T$ in the second $\pi/2$ pulse. In particular we use $\nu = 7.5$ MHz. Both in (b) and (c), the acquired data was normalized with respect to the PL of the $m_S = 0$ state ($|\langle 0|\psi_\mathrm{R}\rangle|^2 = 1$) and the PL of the $m_S = -1$ state ($|\langle 0|\psi_\mathrm{R}\rangle|^2 = 0$). **(d,e)** FFT of the data shown in (b) and (c), respectively, with a Lorentzian fit for each peak. The partial polarization of the nuclear spin (different amplitudes of the FFT peaks) is expected for the external magnetic field of approximately 203 G (see Sec. 1.5). Notice that the splittings between the peaks in (e) are equal to 2.17(1) MHz $\simeq A_\parallel$. Compare with the data in Fig. 1.2 to observe the resolution improvement of the Ramsey interference technique with respect to the ESR experiment.

impurities in the diamond around the NV center, more details about this can be found in Chapter 2.

The frequency components associated with this oscillation are obtained with a Fourier analysis, as shown in Fig. 1.6(d). The three peaks correspond to the each of the three hyperfine states m_I. Notice that the frequency $\omega_{\mathrm{R}}^{(m_I)}/2\pi$ associated with each transition is of the order of MHz, instead of GHz as from the ESR experiments. Though, we need to remember that the phase of the $|0\rangle$ and $|1\rangle$ states is defined in the microwave rotating frame, in such a way that an on-resonant microwave pulse acts as quantum gate without adding a phase related to the duration of the pulse itself. Hence, the energy difference between the two states is $\hbar(\omega_{\mathrm{R}}^{(m_I)} + \omega_{\mathrm{mw}})$, where ω_{mw} is the microwave frequency of the $\pi/2$ gates.

In order to avoid mistakenly taking as positive the value of $\omega_{\mathrm{R}}^{(m_I)}$, when it actually represents a frequency component lower than ω_{mw}, we can add a phase modulation $\omega_{\mathrm{ph}} = 2\pi(7.5\text{ MHz})$ to the second half-π pulse, which effectively changes the rotating frame of the measurement, meaning that the energy difference for each transition becomes $\hbar(\omega_{\mathrm{R}}^{(m_I)} - \omega_{\mathrm{ph}} + \omega_{\mathrm{mw}})$. The results and analysis from the Ramsey experiment with phase modulation in the second mw pulse are shown in Fig. 1.6(c) and (e).

The main advantage of using this interferometric technique is that the result is not power broadened, as it is, in contrast, in the case of the ESR experiment. This means that the frequency resolution is increased, hence allowing to distinguish and measure with higher precision the central frequency and amplitude of the transitions for each of the hyperfine components. The amplitude of the transition is related to the population originally found in the specific hyperfine states $|0, m_I\rangle$. As we will see later on, knowing the hyperfine populations after the initialization is necessary to align the external bias field with the NV quantization axis.

1.4 Lindbladian master equation for NV photodynamics

The NV center photodynamics can be described with a seven-level model [61]. This section includes the theory behind this model, and an example on how to experimentally characterize the model free parameters. A numerical implementation (Python) of this model can be downloaded from Ref. [69].

1.4.1 Bases of the seven-level model

The model uses a spin Hamiltonian to describe the coupling between the NV center and a green laser pulse that connects the ground (${}^3A_2$) and excited (${}^3E$) levels. The two singlet states ${}^1E$ and ${}^1A_1$ are merged into one single metastable state (see Fig. 1.7). The hyperfine interaction is neglected. The generalization of this model to include such interaction can be done following the proposal in Ref. [70].

The spin dynamics is described by a set of optical Bloch equations for a seven energy level model. In the following, the order of the levels is $\{g_{+1}, g_0, g_{-1}, e_{+1}, e_0, e_{-1}, m\}$, where g stands for ground, e for excited, and m for metastable. The set of parameters that completely describes the system is $X = \{\Gamma_{eg}, \Gamma_{1m}, \Gamma_{0m}, \Gamma_{m0}, \theta\}$, together with the excitation rate Γ_{abs}. Γ_{eg} is the spontaneous spin-conserving emission rate and $\Gamma_{ge} = p_{abs}\Gamma_{eg}$ represents the rate for the electric dipole absorption and stimulated emission, with absorption probability p_{abs}. Note that $\Gamma_{abs} \sim \Gamma_{eg}$, the difference being given by corrections due to spin non-preserving radiative transition with rates

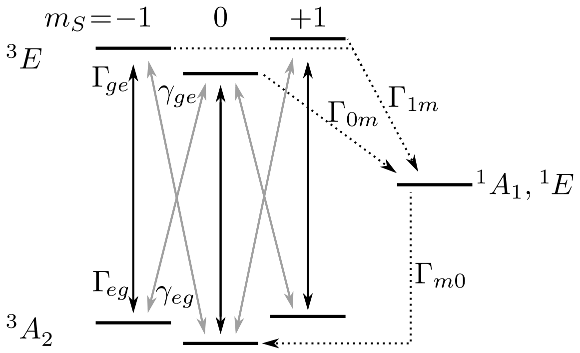

Figure 1.7: Energy levels involved in the excitation and relaxation process during the absorption of green laser light (not to scale). Solid lines represent radiative transitions, while dotted lines represent non-radiative decays. All the solid black arrows are associated to the same decay (*resp.,* excitation) rates Γ_{eg} (*resp.,* Γ_{ge}), while all the gray arrows are associated to the decay (*resp.,* excitation) rates γ_{eg} (*resp.,* γ_{ge}).

γ_{eg}. Thus, $\tan^2\theta = \frac{\gamma_{ge}}{\Gamma_{ge}} = \frac{\gamma_{eg}}{\Gamma_{eg}}$ is the relative probability for a spin non-conserving radiative transition to occur. Additional non-radiative transitions involve the spin singlet state, with decay rates Γ_{1m}, Γ_{0m} from $m_S = +1$ and 0, respectively, towards the metastable, and Γ_{m0} from the singlet towards the $m_S = 0$ in the ground state. All the possible transitions are schematically represented in Fig. 1.7.

The global Hamiltonian describing the radiation-matter coherent interaction for the system, in the laser frequency rotating frame, is represented through the matrix

$$\mathcal{H}_7 = \begin{pmatrix} 0 & 0 & 0 & \Gamma_{ge} & \gamma_{ge} & 0 & 0 \\ 0 & 0 & 0 & \gamma_{ge}/2 & \Gamma_{ge} & \gamma_{ge}/2 & 0 \\ 0 & 0 & 0 & 0 & \gamma_{ge} & \Gamma_{ge} & 0 \\ \Gamma_{ge} & \gamma_{ge}/2 & 0 & 0 & 0 & 0 & 0 \\ \gamma_{ge} & \Gamma_{ge} & \gamma_{ge} & 0 & 0 & 0 & 0 \\ 0 & \gamma_{ge}/2 & \Gamma_{ge} & 0 & 0 & 0 & 0 \\ 0 & 0 & 0 & 0 & 0 & 0 & 0 \end{pmatrix}. \tag{1.7}$$

The spontaneous decays are described by a Lindbladian super-operator, whereby the sum of all the decay routes written in matrix form is:

$$\sum_k \mathcal{L}_k = \begin{pmatrix} 0 & 0 & 0 & \sqrt{\Gamma_{eg}} & \sqrt{\gamma_{eg}/2} & 0 & \sqrt{\Gamma_{m1}} \\ 0 & 0 & 0 & \sqrt{\gamma_{eg}} & \sqrt{\Gamma_{eg}} & \sqrt{\gamma_{eg}} & \sqrt{\Gamma_{m0}} \\ 0 & 0 & 0 & 0 & \sqrt{\gamma_{eg}/2} & \sqrt{\Gamma_{eg}} & \sqrt{\Gamma_{m1}} \\ 0 & 0 & 0 & 0 & 0 & 0 & 0 \\ 0 & 0 & 0 & 0 & 0 & 0 & 0 \\ 0 & 0 & 0 & 0 & 0 & 0 & 0 \\ 0 & 0 & 0 & \sqrt{\Gamma_{1m}} & \sqrt{\Gamma_{0m}} & \sqrt{\Gamma_{1m}} & 0 \end{pmatrix}. \tag{1.8}$$

Accordingly, the density matrix evolution follows the quantum Liouville equation

$$\frac{d\varrho}{dt} = -i[\mathcal{H}_7, \varrho] + \sum_k \mathcal{L}_k \varrho \mathcal{L}_k^\dagger - \frac{1}{2}\mathcal{L}_k^\dagger \mathcal{L}_k \varrho - \frac{1}{2}\varrho \mathcal{L}_k^\dagger \mathcal{L}_k, \tag{1.9}$$

where the sum is done over all the Lindbladian jump operators, i.e., every non-zero element in matrix (1.8). This equation can be solved numerically to obtain the time dependence of the system density matrix.

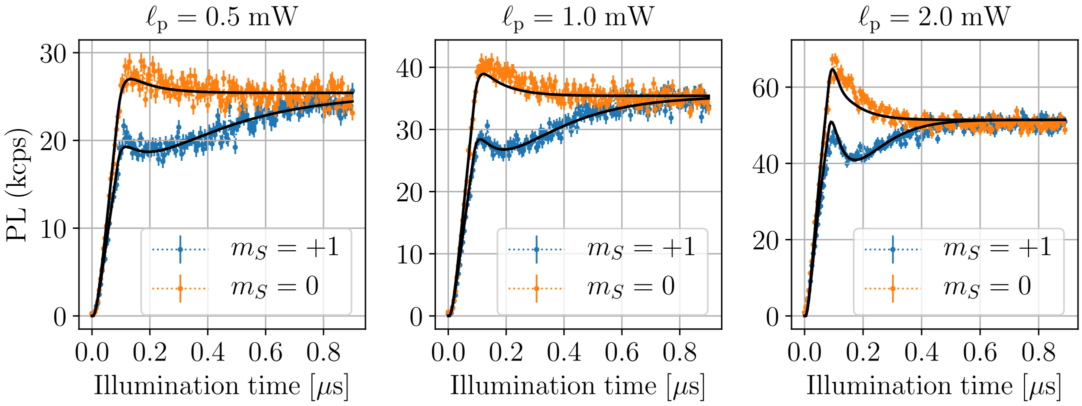

Figure 1.8: Measured photoluminescence (PL) intensity as a function of the green laser illumination time, for a given laser power ℓ_p. The experimental data for both the initial states $m_S = 0$ (orange dots) and $m_S = +1$ (blue dots), and for the three different ℓ_p values was simultaneously used to fit the parameters X and p_{abs} of the seven-level model. The numerical simulation with the fitted parameters is shown as solid black lines. The relatively slow rise time of the signal is due to the 80 ns integration time of the SPD (readout).

Finally, it is possible to include a coupling between the $m_S = 0$ and $m_S = +1$ (or $m_S = -1$) ground states mediated by a resonant mw excitation. This is only valid when the laser is off, since the rotating frame is different for these two couplings. With this aim, the Hamiltonian $\mathcal{H}_2$ (see Eq. 1.5) can be easily extended to this seven level model. This becomes useful for the simulation of qubit gates applied before or after the interaction with laser pulses, or even a continuous driving with short laser pulses interactions, as will be the case in upcoming chapters.

1.4.2 Experimental characterization of the model free parameters

As described in the previous section, the seven level model is completely characterized by five parameters $X = \{\Gamma_{eg}, \Gamma_{1m}, \Gamma_{0m}, \Gamma_{m0}, \theta\}$ – four decay rates and an angle that defines ratio between forbidden and non-forbidden radiative transitions. For the characterization of these parameters, one can measure the emitted red photoluminescence (PL) in terms of the illumination time with green laser light [71]. Results of such experiment are shown in Fig. 1.8, as well as the simulations after fitting the parameters in X, which values are reported in Tab. 1.1. The excitation rate depends on the intensity of the green laser, in particular for the three different experiments shown in Fig. 1.8, we found that $0.2\Gamma_{ge} \leq \Gamma_{abs} \leq 0.45\Gamma_{ge}$. The lifetime of the excited states is $1/(\Gamma_{eg}+\Gamma_{1m}) \sim 7$ ns for $m_S = \pm 1$, and $1/(\Gamma_{eg}+\Gamma_{0m}) \sim 12$ ns for $m_S = 0$.

1.5 Aligning the external bias field

All the NV center-based experiments are performed in the presence of an external bias field that, as already mentioned, modifies the energy levels of the NV electronic spin via Zeeman effect. A strong bias fields (around 510 G) also enables dynamic

Table 1.1: Parameters resulting from the fit of photo-luminescence with the seven-level model. The decay rates correspond to the transitions represented in Fig. 1.7. The value of θ results in a forbidden/non-forbidden transition ratio $\tan^2\theta \simeq 0.038$. Notice that the parameter Γ_{eg} was fixed to a previously reported value.

Parameter	Rate
Γ_{eg}	77 MHz [71]
Γ_{1m}	60.4 ± 0.3 MHz
Γ_{0m}	9.39 ± 0.05 MHz
Γ_{m0}	9.6 ± 0.05 MHz
θ	0.193 ± 0.011 rad

nuclear polarization of nitrogen [64, 72] at the excited-state level anticrossing (ES-LAC). However transverse bias field components have detrimental effect since they induce spin-mixing of the spin levels, and reduce the NV photoluminescence intensity and the contrast of optically-detected ESR [73]. A meticulous alignment of the bias field along the NV quantization axis is therefore an essential prerequisite of most of single-NV experiments. In our setup, the bias field is produced by a permanent magnet mounted on a translation and rotation stages. This Section describes a procedure used to finely align the magnet to minimize transverse field components.

1.5.1 Increase field while tracking down the ESR transition frequency

In this section we show the procedure to track down the $m_S = 0 \leftrightarrow m_S = \pm 1$ transition frequency while moving the magnet closer to the diamond. This is useful when a reference position of the magnet for high fields is not known, for example, when mounting a new diamond or the same diamond with a different orientation.

Starting from the farthest possible position of the magnet with respect to the diamond, the ESR signal should show a deep near to the ZFS $D_\text{g} \simeq 2.87$ GHz. From this reference point, one should slightly move the magnet closer to the diamond, in steps of a few millimeters. In this way it is possible to slightly change the frequency window explored with the ESR experiment, and follow the transition while moving the magnet, as shown in Fig. 1.9(a). Notice that for these measurements it is convenient to use high power mw in order to power broaden the hyperfine transitions up to the case where only a single broad deep is visible in the ESR signal. When the transition frequency ω_ESR has been measured, an approximate value[5] of the bias field at the NV center position can be calculated as $B = (D_\text{g} - \omega_\text{ESR})/\gamma_e$. The estimated magnetic field with respect to the magnet position is shown in Fig. 1.9(b). Notice that from this plot it is possible to conclude that the amplitude of the magnetic field approximately behaves as $1/d^2$, where d is the magnetic-diamond absolute distance However, we expect that this behavior, associated with a spherical symmetry or a point charge source, will not continue for $d \to 0$, due to the cubic shape of the permanent magnet.

Once identified the ESR resonance, a rough alignment of the magnet along the NV axis can be performed by exploiting the rotation mount stage, which we align

---

[5] The approximated value becomes closer to the exact value as the magnetic field becomes better aligned with the spin quantization axis.

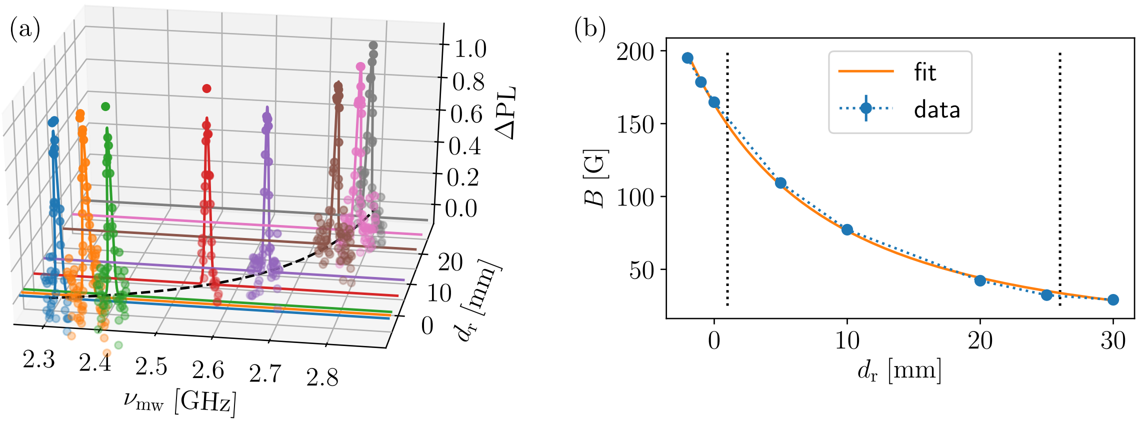

Figure 1.9: **(a)** ESR measurements to track down the $m_S = 0 \leftrightarrow m_S = \pm 1$ transition frequency while moving the magnet closer to the diamond. The (inverted) normalized PL amplitude ΔPL of the ESR transition line is plotted in terms of the mw frequency ν_{mw} for each of the magnet–diamond relative distance d_{r}, measured along the Z-direction of the translation stage. The dashed line represents the behavior of the transition frequency ω_{ESR} in terms of d_{r}. **(b)** Magnetic field, estimated from ω_{ESR} (see text), in terms of the magnet–diamond relative distance. The vertical dashed lines show the position at which the stick holding the magnet was moved from one screw hole to the next one in the XYZ translation stage. The relative distance equal to zero represents having the magnet in the first hole of the stage with the micrometer screw in the $z = 0$ mm position. The fitted function is $f(d) = a/d^2$, where $a = (7.7 \pm 2.4) \times 10^3$ G mm is an amplitude factor, and $d = d_{\mathrm{r}} - d_0$ is the magnetic-diamond absolute distance, with $d_0 = (-21.7 \pm 0.4)$ mm.

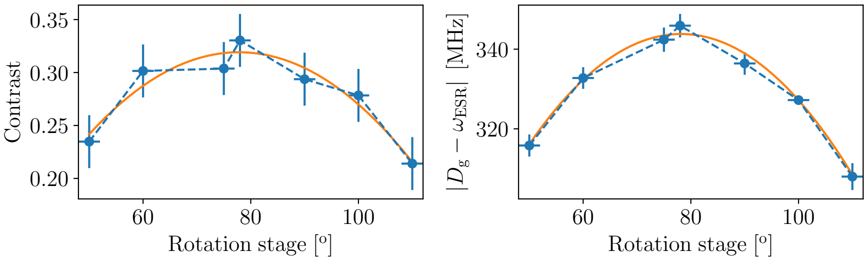

Figure 1.10: Results from ESR measurements to align the rotation stage holding the magnet. The optimal position of the rotation stage is achieved by maximizing either the contrast of the measured ESR signal **(a)** or the difference between the ZFS and the transition frequency ω_{ESR} **(b)**. In both cases a parabolic fit was used to find the center of the distribution, which corresponds to $(78 \pm 1)^{\mathrm{o}}$.

by maximizing the ESR contrast. We use high microwave power to observe a single power-broadened deep ESR peak independently of the polarization degree of the nuclear spin. Besides maximizing the contrast, an equivalent option is to maximize the difference between the measured transition frequency ω_{ESR} and the ZFS. In Fig. 1.10 we show both quantities in terms of the rotation stage angle. In this particular dataset, the external magnetic field amplitude was approximately 124 G, and the ESR experiments where performed for the $m_S = 0 \leftrightarrow m_S = +1$ transition.

Once the rotation stage has been aligned, it is not necessary to change its angle to align the magnetic field at any other position of the Z-stage.

A finer alignment of the magnetic field orientation can be obtained by moving the micrometric X-Y mount stages of the magnet, and monitoring polarization of the nuclear spin projection m_I, induced by optical pumping due to the presence of the excited state level anti-crossing (ESLAC) [64]. For magnetic fields near to the ESLAC (around 510 G) the degeneracy of the $m_S = 0$ and $m_S = -1$ spin projections in the excited state ${}^3E$, together with the the transverse hyperfine coupling, induce electron-nuclear spin flip-flops [72], which after several excitation-relaxation cycles results in the polarization of the nuclear spin. Also far away from the ESLAC [74] a non perfect polarization of the nuclear spin is still measurable. When the magnetic field has a transverse component, the effectiveness of this polarization mechanism is reduced. Hence, the alignment protocol is based on measuring the m_I population distribution while changing the position of the magnet with the X- and Y-stages. A Fourier analysis of a Ramsey experiment enables to accurately measure the polarization ratio, defined as $P_{m_I} \equiv a_{m_I}/(a_{+1} + a_0 + a_{-1})$, where a_{m_I} is the area below the measured transition line, as shown in Fig. 1.11(a) and (b). In Fig. 1.11(c) we show a two dimensional map of the polarization ratio P_{+1} in terms of the X and Y positions of the translation stage. The magnetic field is aligned at the position where P_{+1} is maximized.

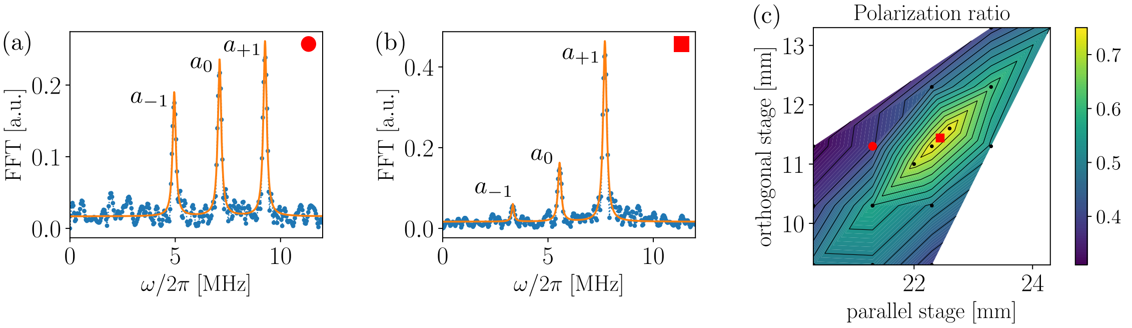

Figure 1.11: Results of the Ramsey experiment used to align the external magnetic field at approximately 203 G. **(a,b)** The FFT of the Ramsey signal shows the transition lines for each of the m_I projections. These experiments where performed for the $m_S = 0 \leftrightarrow m_S = -1$ transition. A Lorentzian function is fitted to extract the area a_{m_I} of each transition line. **(c)** Map of the polarization ratio P_{+1} for different positions of the translation XY-stage, in order to find the position that maximizes P_{+1}. A red circle and a red square represent the position of the translation stage for the measurements shown in (a) and (b), respectively.

Part I

Noise spectroscopy

Chapter 2

Noise spectroscopy of a quantum-classical environment with a diamond qubit

As quantum sensors, NV-based sensors exploit quantum resources to enhance the detection of physical signals. They have been successfully used for measuring magnetic and electric fields [5, 12, 13], temperature[14, 15], rotation [16], strain and pressure [17], and more. Remarkably, NV magnetometers have been demonstrated to be capable of measuring very localized ultra weak AC fields, achieving sensitivities of the order of $\mathrm{pT}/\sqrt{\mathrm{Hz}}$ with ensemble devices [14] in ambient conditions. However, the great sensitivity to external magnetic fields implies that the NV center is also coupled with environmental noise, which limits its sensing capabilities by reducing the coherence of its quantum states. The knowledge of the inherent noise of any quantum device is therefore an essential prerequisite to define its performances and optimize its functioning through tailored error correction strategies. When dealing with spin-qubit sensors in the solid state, noise-tailored protection protocols are crucial to prolong the spin coherence and improve the sensor performance. For a bulk diamond with natural abundance of carbon, as the one used in this work, dephasing in the NV center triplet ground state is mainly caused by the coupling with a ^{13}C nuclear spin bath with characteristic time (at room temperature) $T_2^* \sim \mu$s [75].

In this Part of the thesis, we experimentally demonstrate the capabilities of a protocol used to characterize this nuclear spin bath. This protocol is particularly interesting because it is not based on the assumption of weak coupling with the noise source. Crucially for quantum devices, we show that the acquired knowledge of the spin bath can reliably predict the NV spin dynamics, even under drivings that differ from the ones used for noise spectroscopy.

In Sec. 2.1, a brief introduction to this work is given, that includes the contextualization of the current work with respect to other recent research. In addition, the section introduces basic concepts of quantum control applied to spectroscopy. Section 2.2 contains the theory to formally describe the nuclear spin environment and its interaction with the NV center. The experimental protocol, results and analysis concerning the characterization of the environment is given in Sec. 2.3. Section 2.4 includes a discussion about the limits of a classical model used to describe the spin bath. The predictive power of the characterized environment is explored in detail in Sec. 2.5. Finally, section 2.6 contains the summarized results and conclusions of this work.

The content of this chapter has been partially published in different journals.

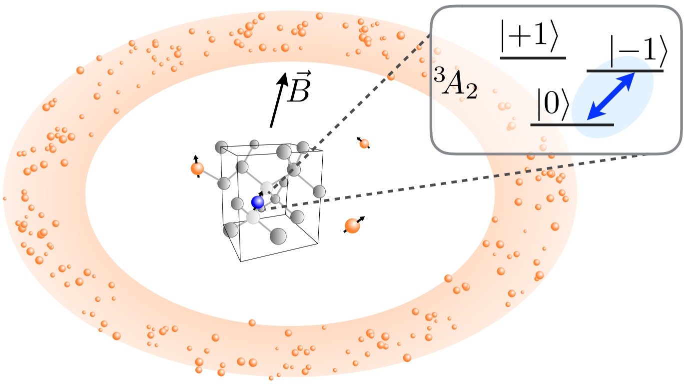

Figure 2.1: The NV electronic spin (blue sphere) is sensitive to ^{13}C impurities in the diamond (orange spheres), including isolated nearby spins and a larger ensemble spin bath (orange shadow). The spin sensor is formed by the electronic spin projections $\{0, -1\}$ of the orbital ground state $^3A_2$.

The recent advances in quantum control assisted quantum sensing and spectroscopy of magnetic fields with an NV center are discussed in Ref. [76]. The main project described in this Part of the thesis concerns the characterization of the NV center environment formed by randomly oriented ^{13}C nuclear spins, that collectively act as a spin bath inducing decoherence to the NV spin qubit. This was reported in Ref. [77]. Three proceedings articles were published for a brief description of the environment noise spectroscopy [78], and the application of the acquired information from the environment to optimize the sensing capabilities of the qubit as a magnetometer [79, 80].

2.1 Noise spectroscopy methods

The spectral characterization of a magnetic field can be conducted through the analysis of relaxation and dephasing processes occurring to the probe system itself due to the interaction with the target field. Relaxometry consists in the measurement of the relaxation rate of the sensor that is connected with the spectral density of a signal $S(\omega)$, linearly in the first order approximation. This method—introduced in nuclear magnetic resonance (NMR) [81]—has been exploited with NV sensors to investigate especially high-frequency noise, through on the measurements of the T_1 relaxation time [82–86]. The alternative approach, commonly used for the noise spectroscopy [87–91], relies on the systematic analysis of the sensor decoherence under sets of dynamical decoupling (DD) control sequences [92–95]. Periodic DD sequences realize narrow frequency filters that select only a specific noise contribution, while canceling all other interactions. This method has been used for noise identification with spin qubits in diamond [96–98], superconductive flux qubits [99], trapped ions [100], and nanoelectronic devices [101]. Most of these noise spectroscopy methods assume the environment to be a classical stochastic bath [90, 95, 102]. In addition these methods rely on the assumption that the noise is weak enough to allow relatively long qubit coherence time under the applied control.

Here, we experimentally demonstrate a protocol for characterizing the qubit environment that overcomes the challenges arising when those assumptions are not verified. We implement the protocol using the electron spin qubit associated with a single Nitrogen-vacancy (NV) center in diamond, which has emerged as a powerful

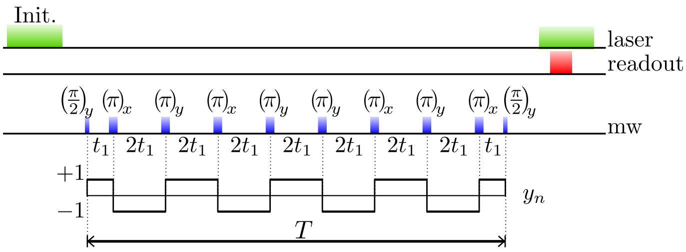

Figure 2.2: Base DD sequence used to characterize the nuclear spin environment. The π pulses are applied inside a Ramsey scheme in order to measure the NV spin coherence. The DD sequence corresponds to an XY-8 sequence [103], where the phase ϕ of each π pulse is alternated between π_x ($\phi = 0$) and π_y ($\phi = 90°$). This base sequence can be repeated to obtain DD sequences with n impulses, where n is a multiple of 8. The bottom line shows the modulation function $y_n(t)$, which acts as a control field.

platform for quantum technologies [2, 10]. In the presence of a static bias field B aligned along the NV axis, we can restrict the description to an NV spin subspace, $\{|0\rangle, |-1\rangle\}$. The NV qubit displays a complex environment, comprising ^{13}C nuclear spins randomly distributed in the diamond lattice. The thermal and quantum fluctuations of this environment, and the distribution of environment-qubit interaction strengths make this an extremely rich scenario where to test our protocol. The environment can be divided into a small set of resolved ^{13}C, and a large ensemble of unresolved ^{13}C that we treat as a collective bath [Fig. 2.1]. We can further tune the ratio between the environment internal energy and its coupling to the NV center by varying the strength of an applied external magnetic field, thus exploring different bath regimes [96].

2.1.1 Dynamical decoupling for noise spectroscopy

The coherent interaction with fully resolved nearby nuclear spins, and the dephasing induced by the nuclear spin bath are characterized by performing a systematic analysis of the qubit coherence under a set of DD control protocols. The origin of DD protocols can be trace back to the 1950's, when they were used in the field of nuclear magnetic resonance (NMR) [104–107]. The elementary DD protocol is Hanh's spin-echo [104], where a π pulse is applied halfway of the spin precession in order to time reverse the spin evolution, so that the phase accumulated in the two time segments cancels out. This concept can be extended to multiple refocusing π pulses that repeatedly flip the qubit spin. The time distribution n of π pulses defines a control field, that is described by a modulation function $y_n(t)$ with a sign switch at the position of each π pulse, indicating the direction of time evolution, forward or backward, as schematized in Fig. 2.2. This results in narrow frequency filters that select only a specific coupling and frequency to be probed, while decoupling the system from the rest of the environment, which is ideal for spectroscopy. The set of π pulses of the DD sequence is incorporated in a Ramsey interferometer (see Sec. 1.3.3) in order to map the phase acquired by the NV spin into the residual population of the state $|-1\rangle$

$$P_n(T) = \frac{1}{2}\left(1 + W_n(T)\right), \tag{2.1}$$

where n is the number of pulses of the DD sequence, T is the sensing time, and W_n is the residual coherence of the qubit. The qubit coherence can be factorized into two independent contributions $W_n = W_n^{\rm c} \cdot W_n^{\rm d}$, where $W_n^{\rm c}$ describes coherent interactions, and $W_n^{\rm d}$ englobes the presence of decoherence. In the present study, the first factor corresponds to the coherent coupling with a small set of single nuclear spins that can be individually resolved. The coupling between the NV spin and each of these nuclear spins was characterized using the methodology proposed in Refs. [23–25]. On the other hand, the dephasing caused by the interaction with the nuclear spin bath is ruled by a stochastic variable with power spectral density $S(\omega)$, also known as *noise spectral density* (NSD) [Sec. 2.2]. As a result of this interaction, the qubit coherence is destroyed $W_n^{\rm d}(T) = e^{-\chi_n(T)}$, where the decoherence function

$$\chi_n(T) = \int \frac{{\rm d}\omega}{\pi\omega^2} S(\omega) \left|Y_{n,T}(\omega)\right|^2 \tag{2.2}$$

is the convolution between the NSD and the square modulus of the filter function

$$Y_{n,T}(\omega) \equiv \int_0^T \frac{{\rm d}t}{T} e^{-i\omega t} y_n(t). \tag{2.3}$$

Hence, in order to measure the NSD $S(\omega)$ it is necessary to perform a deconvolution analysis. A perfect monochromatic filter function would greatly reduce the difficulty of this task. However, this would require virtually infinitely long measurement times, which is not only impractical, but also impossible because the decoherence itself limits the available measurement time. A realistic approach involves using a Carr-Purcell (CP) sequence [105], formed by a set of n equidistant π pulses, with interpulse delay time $2t_1$ [Fig. 2.2]. This pulse train acts as a narrow quasi-monochromatic and tunable filter, where t_1 selects the pass-band frequency, while n determines the filter width [108, 109]. In Sec. 2.3 we show how to simultaneously characterize the NSD and the coupling with nearby nuclear spins, using CP-based DD sequences. In Sec. 2.5 we demonstrate that this characterization of the nuclear spin environment has predictive capabilities. In particular we predict and measure the spin dynamics under a set of non-equidistant DD sequences, that has been recently proposed as candidates to improve the coherence of a quantum sensor in the presence of detrimental noise.

2.2 The nuclear spin environment

This section contains the theory used to describe the coupling between the NV center electronic spin and its environment, formed by an ensemble of Carbon-13 nuclear spins ($I = 1/2$), present in natural abundance (1%) inside the diamond lattice.

The interaction with nuclear spins is described in a similar fashion to the formalism used in Sec. 1.1 (see Eq. (1.2)). Notice that the hyperfine splitting is three orders of magnitude smaller than the ZFS, meaning that hyperfine coupling will not flip the electronic spin, i.e., the S_x, and S_y terms can be neglected [23]. This leads to a system-environment Hamiltonian

$$\mathcal{H} = \mathcal{H}^{(\rm NV)} + \frac{\omega_L}{2} \sum_k \sigma_z^{(k)} + \sum_k S_z \cdot \boldsymbol{\omega}_h^{(k)} \cdot \boldsymbol{\sigma}^{(k)}/2, \tag{2.4}$$

where $\mathcal{H}^{(\rm NV)} = D_{\rm g} S_z^2 + \gamma_{\rm e} B S_z$ depends only on the NV center electronic spin, $\omega_L = \gamma_n^{(C)} B$ is the Larmor frequency of the ^{13}C nuclei, with $\gamma_n^{(C)} = 1.0705$ kHz/G being the nuclear gyromagnetic ratio, and $\boldsymbol{\omega}_h^{(n)}$ is the hyperfine-interaction frequency tensor. The sum is done over all ^{13}C nuclear spins that interact with the NV center. The last term incorporates a small set of discrete couplings that can be fully resolved, as later shown in section 2.2.1, and a broad unresolved distribution of couplings that we describe as a collective bath. In the strong coupling regime, where the typical coupling strength overcomes the environment internal energy ($\|\omega_h\| \geq \omega_L$), the creation of entanglement between spin qubit and a large environment, with subsequent tracing over of the environment, induces loss of qubit coherence [77, 96]. In the weak coupling limit, $\|\omega_h\| \ll \omega_L$, the environment can be modeled as a classical stochastic field, as we will describe in the following section, also leading to a non-unitary qubit dynamics characterized by dephasing.

2.2.1 Interaction with single nuclear spins

Now we focus on the interaction between the NV electronic spin, and a single 13-carbon nuclear spin. Eq. (2.4) can be recast as $\mathcal{H} = \mathcal{H}^{(\mathrm{NV})} + \mathcal{H}^{(\mathrm{NV\text{-}C})}$, where $\mathcal{H}^{(\mathrm{NV\text{-}C})} \equiv \frac{1}{2}\left(\omega_L \sigma_z^{(\mathrm{C})} + \omega_h^{\|} S_z \sigma_z^{(\mathrm{C})} + \omega_h^{\perp} S_z \sigma_x^{(\mathrm{C})}\right)$. Notice that this Hamiltonian is diagonal for the electronic spin $\mathbf{S}$. In addition, we set $\mathcal{H}^{(\mathrm{NV})} = 0$ without loss of generality, due to the fact that $[\mathcal{H}^{(\mathrm{NV})}, \mathcal{H}^{(\mathrm{NV\text{-}C})}] = 0$. Therefore, the Hamiltonian can be written as

$$\mathcal{H} = \sum_{m_S} |m_S\rangle\langle m_S| \otimes \mathcal{H}_{m_S}, \tag{2.5}$$

where the nuclear spin Hamiltonian $\mathcal{H}_{m_S}$ is conditioned by the state of the electronic spin

$$\mathcal{H}_{m_S} = \frac{1}{2}\left((m_s\, \omega_h^{\|} + \omega_L)\sigma_z^{(\mathrm{C})} + m_s\, \omega_h^{\perp} \sigma_x^{(\mathrm{C})}\right). \tag{2.6}$$

As mentioned before, during this work we restrict the description to an NV spin subspace, $\{|0\rangle, |{-1}\rangle\}$. The initial electronic state, after the first Ramsey $\pi/2$ pulse, is $|\psi_S\rangle = (|0\rangle + |{-1}\rangle)/\sqrt{2}$. The nuclear spins are completely unpolarized, therefore the initial state of the bipartite system is

$$\rho_0 = |\psi_S\rangle\langle\psi_S| \otimes \mathbb{1}_I/2. \tag{2.7}$$

The evolution of the system for a sequence of n pulses is given by

$$\rho(T) = U(t_{n+1})\left(\overleftarrow{\Pi}_{j=1}^{n} X U(t_j)\right)\rho_0 \left(\Pi_{j=1}^{n} U^\dagger(t_j) X\right) U^\dagger(t_{n+1}) \tag{2.8}$$

where the system evolves under the unitary evolution operator U for the time intervals t_j between two consecutive microwave pulses ($\overleftarrow{\Pi}$ denotes time ordered product from right to left), and X represents the pauli-X gate that associated with an ideal π pulse:

$$U(t) \equiv e^{-it\mathcal{H}} = \sum_{m_S} |m_S\rangle\langle m_S| \otimes e^{-it\mathcal{H}_{m_S}} \tag{2.9}$$

$$X \equiv (|0\rangle\langle -1| + |{-1}\rangle\langle 0|) \otimes \mathbb{1}_I = \sigma_x^{(\mathrm{NV})} \otimes \mathbb{1}_I \tag{2.10}$$

The measurement of the electronic spin coherence under a DD sequence (embedded in a Ramsey scheme) is written as

$$\begin{aligned} M(T) &= \langle \sigma_x^{(\mathrm{NV})} \rangle \\ &= \mathrm{Tr}_S \left[\rho^{(\mathrm{NV})}(T) \sigma_x^{(\mathrm{NV})} \right] \\ &= 2\,\mathfrak{R}(\langle 0| \rho^{(\mathrm{NV})}(T) |{-1}\rangle) \\ &= 2\,\mathfrak{R}(\langle 0| \mathrm{Tr}_C \left[\rho(T)\right] |{-1}\rangle) \\ &= 2\,\mathfrak{R}\left(\langle 0| \sum_{m_I} \langle m_I| \rho(T) |m_I\rangle |{-1}\rangle \right) \\ &= 2\,\mathfrak{R}\left(\sum_{m_I} (\langle 0| \otimes \langle m_I|) \rho(T) (|{-1}\rangle \otimes |m_I\rangle) \right), \end{aligned} \tag{2.11}$$

where $\mathfrak{R}$ stands for real part, and we have used that $\rho^{(\mathrm{NV})}(T) = \mathrm{Tr}_C\left[\rho(T)\right]$, and $\mathrm{Tr}_C[\cdot] = \sum_{m_I} \langle m_I| \cdot |m_I\rangle$. The combination of equations (2.7) to (2.11) implies that

$$M(T) = \mathfrak{R}\left(\sum_{m_I} \langle m_I| U_0 \left(\langle m_S^{(n,0)}|\psi_S\rangle \langle \psi_S|m_S^{(n,-1)}\rangle \right) U_{-1}^{\dagger} |m_I\rangle \right) \tag{2.12}$$

where $|m_S^{(n)}\rangle$ represents the result of applying n flips to the electronic spin state $|m_S\rangle$ ($|m_S^{(n)}\rangle = |m_S\rangle$ for even-n), and

$$U_{-1}^{\dagger} \equiv \begin{cases} e^{it_1\mathcal{H}_{-1}} e^{it_2\mathcal{H}_0} \dots e^{it_n\mathcal{H}_0} e^{it_{n+1}\mathcal{H}_{-1}}, & \text{(even } n\text{)} \\ e^{it_1\mathcal{H}_0} e^{it_2\mathcal{H}_{-1}} \dots e^{it_n\mathcal{H}_0} e^{it_{n+1}\mathcal{H}_{-1}}, & \text{(odd } n\text{)} \end{cases} \tag{2.13}$$

$$U_0 \equiv \begin{cases} e^{-it_{n+1}\mathcal{H}_0} e^{-it_n\mathcal{H}_{-1}} \dots e^{-it_2\mathcal{H}_{-1}} e^{-it_1\mathcal{H}_0}, & \text{(even } n\text{)} \\ e^{-it_{n+1}\mathcal{H}_0} e^{-it_n\mathcal{H}_{-1}} \dots e^{-it_2\mathcal{H}_0} e^{-it_1\mathcal{H}_{-1}}, & \text{(odd } n\text{)} \end{cases} \tag{2.14}$$

Notice that $\langle m_S^{(n,0)}|\psi_S\rangle \langle \psi_S|m_S^{(n,-1)}\rangle = \frac{1}{2}$, for any n, because the initial electronic state $|\psi_S\rangle$ is a perfect superposition. Meaning that the electronic spin coherence under a DD sequence while interacting with a single nuclear spin is given by

$$M_n(T) = \frac{1}{2} \mathfrak{R}\, \mathrm{Tr} \left(U_0 U_1^{\dagger} \right). \tag{2.15}$$

Hence, we are only required to characterize the coupling strength components, $\omega_h^{\parallel}$, and $\omega_h^{\perp}$, in order to predict the NV spin dynamics under different kinds of DD sequences. Equation (2.15) will be used in Sec. 2.5 to compare the simulated dynamics with experimental data.

In order to characterize the coupling strength we use a CP sequence with an even number of π pulses, in this case $M_n(T)$ can be calculated analytically [23–25], leading to

$$M_n^{(\mathrm{CP})}(2nt_1) = 1 - 2\left(\frac{\omega_h^{\perp}}{\omega_1}\right)^2 \sin^2\left(\frac{\omega_1 t_1}{2}\right) \sin^2\left(\frac{\omega_L t_1}{2}\right) \frac{\sin^2\left(\frac{n\phi}{2}\right)}{\sin^2\left(\frac{\phi}{2}\right)}, \tag{2.16}$$

where $2t_1$ is the time between pulses, $\omega_1 = \sqrt{(m_s\,\omega_h^{\parallel} + \omega_L)^2 + (\omega_h^{\perp})^2}$ is the frequency seen by the spin in the $m_s = \pm 1$ state, and the phase ϕ is the modulation frequency of the transition probability as a function of n, given by

$$\cos\phi = \frac{m_s\,\omega_h^{\parallel} + \omega_L}{\omega_1} \sin(\omega_1 t_1) \sin(\omega_L t_1) - \cos(\omega_1 t_1) \cos\left(\omega_L t_1\right). \tag{2.17}$$

In Sec. 2.3, we use this formalism to experimentally characterize the coupling strength with three different nearby ^{13}C nuclear spins. From those measurements, we observed that ϕ is small for times t_1 corresponding to the minimum values of $M_n^{(\mathrm{CP})}$. Note that equations (2.16) and (2.17) are equivalent to the ones in Refs. [24, 25] with the simple transformation $\phi \to \phi' = \pi - \phi$. Both of these conventions are consistent with the model and suitable to evaluate the two components of the hyperfine strength, because they assume the same $M_n^{(\mathrm{CP})}$ values for even integer n; nonetheless, they result in a very different periodicity of P_n as a function of n, making the analysis of the data very different in terms of the convergence of the fit.

2.2.2 Classical model for a quantum bath

The collective effect of the spin bath is to induce decoherence into the NV spin. It has been proved that any decoherent process acting on a qubit (or qutrit) can be described by a random unitary map (RUM) [110, 111], even when it arises from an underlying quantum bath. In general, this classical description of the interaction is non-predictive, since the RUM may depend on the quantum control applied to the qubit. Remarkably, for the spin bath considered in our work, we have found that the classical model becomes predictive in the limit of weak coupling between the system and the environment.

A fully detailed prove on how to convert Eq. (2.4) into a RUM can be found in Ref. [77] (Supplemental material, Sec. S-II). Here we will present the general idea, without going into too much details. As for the previous section, the system+environment Hamiltonian can be rewritten as

$$\mathcal{H} = \sum_{m_S} \upsilon_{m_S}(t)\, |m_S\rangle\langle m_S| \otimes B_{m_S}. \tag{2.18}$$

Here $\upsilon_{m_S}(t)$ is a scalar representing the coupling to the m_S state of the NV spin, which can be time dependent if pulsed control is applied on the system, and

$$B_{m_S} = \frac{1}{2}\sum_k (m_s\, \omega_h^{k,\parallel} + \omega_L)\sigma_z^{(k)} + m_s\, \omega_h^{k,\perp}\sigma_x^{(k)}. \tag{2.19}$$

Again, in a similar fashion to what we did in the previous section, and assuming that the system is initially prepared in a superposition state $|\psi_S\rangle = (|0\rangle + |{-1}\rangle)/\sqrt{2}$, then the spin coherence in a Ramsey-like sequence is given by

$$W^{\mathrm{d}}(T) = \Re[\mathrm{Tr}_B(U_{0,B}\, \rho_B\, U_{1,B}^\dagger)] \tag{2.20}$$

where $U_{m_S,B}$ are the unitary evolution operators for the bath subspace, conditioned on the state of the system m_S. For a bath of non-interacting nuclear spins and for a DD sequence such as CPMG with n cycles, the NV coherence can be finally written as [77]:

$$W_n^{\mathrm{d}}(T) = \exp\left[-2\sum_k |\omega_h^{k,\perp}|^2 \frac{\sin^4\left(\frac{T\omega_L}{4}\right)\sin^2\left(nT\omega_L\right)}{\omega_L^2\cos^2\left(\frac{T\omega_L}{2}\right)}\right] \tag{2.21}$$

These results can be modeled by assuming the presence of a classical magnetic field, with a static component with rms $\Delta B^2 = \sum_k |\omega_h^{k,\parallel}|^2$ (which gets refocused by DD sequences) and a stochastic one, with spectrum $S(\omega) = \sum_k |\omega_h^{k,\perp}|^2 \delta(\omega - \omega_L)$. This model has predictive powers for any pulsed DD sequence, under the assumption that we neglect the higher orders of the interaction between the NV electronic spin and the spin bath. The condition for neglecting the higher orders is related to the ratio $\|\omega_h\|/\omega_L$ (or, in the case of DD sequences, $\omega_h^\perp/\omega_L$). Here, bath couplings without an index indicate the "typical" interaction strength (indeed, a discrete number of more strongly coupled bath spins could be treated separately, following their coherent evolution, as done in the previous section). For strong noise ($\|\omega_h\| \approx \omega_L$), where one needs to take into account higher order terms, it would still be possible to find a classical model but the model must be varied every time one selects a different control scheme, even when we limit the control to π-pulses (DD sequences).

The bases presented in the previous, and in this section are enough to spectroscopically characterize the nuclear spin environment around the NV center.

2.3 Spectral characterization of the environment

As mentioned in Sec. 2.1, the spectral characterization of the environment was achieved by performing a systematic spectral analysis of NV spin coherence under DD sequences with equidistant pulses. In particular, we use the XY-8 sequence [103] as base cycle, as it is designed to improve robustness against detuning and imperfections of the π-pulse shape. The time between consecutive pulses is defined as $2t_1$ (see Fig. 2.2), leading to a total sensing time $T = 2nt_1$. An example of the measurement of the residual population P_n (see Eq. (2.1)) as a function of the time between pulses is shown in Fig. 2.3(a). In these particular measurements, the number of pulses was fixed to $n = 8$, 16, and 24 pulses, meaning that one, two, or three consecutive XY-8 sequences where applied, respectively. There are two different kinds of loss (collapses) of the electronic spin coherence. The collapses due to the interaction with the spin bath are the broad ones and go down to $P_n = 0.5$, as the one marked with a black diamond in Fig. 2.3(a). The analysis of these collapses give access to the noise spectral density (NSD) modeling the large spin bath, as shown in the next section. Narrow collapses (marked with with a square) can reach $P_n < 0.5$ and originate from the interaction with individual strongly coupled nuclear spins. Characterizing the two contributions to the signal loss gives us a full picture of the spin environment. The overall coherence decay for t_1 values 'outside' the collapses (marked with with a star) is caused by a combination of decoherence (T_2) and spin relaxation (T_1), depending on the number of applied pulses.

The difference between the bath induced decoherence, and the coherent coupling with single nuclear spins is even more evident when the interpulse time t_1 is fixed and the behavior of the coherence in terms of the number of pulses is observed. While the collective spin bath induces an exponential decay of P_n [Fig. 2.3(c)], the coherent coupling to nearby nuclei generates coherent oscillations [Fig. 2.3(b)]. In the Sec. 2.3.1 we show how to reconstruct the NSD from the measurement of the exponential decay time of the signal. On the other hand, in Sec. 2.3.3 we show how the coherent oscillations give enough information to extract the coupling strength with a single nuclear spin.

2.3.1 Characterization of the NSD

For now, we will focus on the loss of coherence in order to characterize the NSD of the spin bath. The exponential decay of the qubit coherence allows the extraction

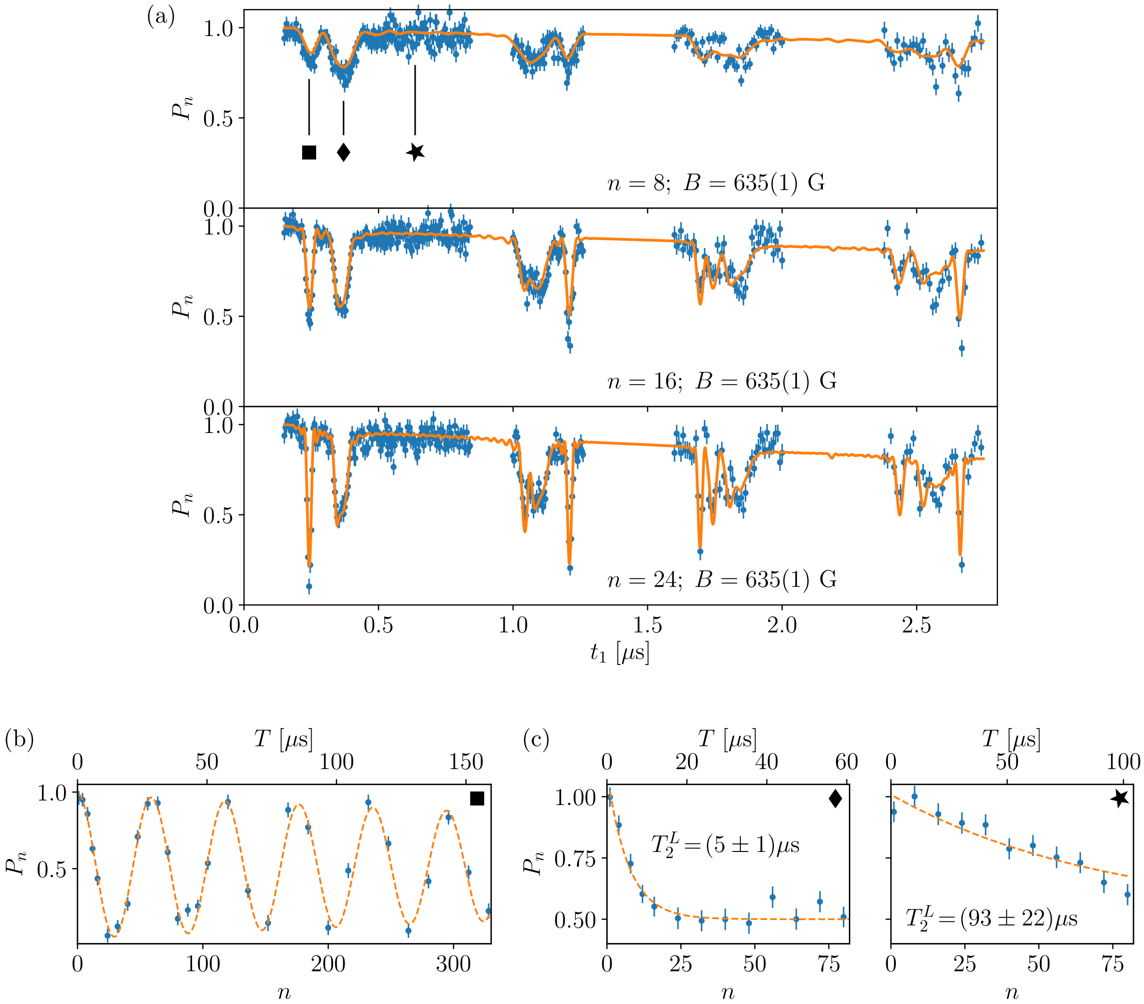

Figure 2.3: Spin coherence, mapped into population P_n [Eq. 2.1], as a function of t_1 with n fixed **(a)**, or as a function of n with t_1 fixed **(b-c)**. **(a)** The evolution of P_n for $n = 8$, 16, and 24. Notice that for different n values, the collapses occur at the same t_1 values, although the total measuring time $T = 2nt_1$ is different. The collapses become narrower when n increases, this is a signature on how the filter function becomes narrower for larger n. The orange line is a simulation of the spin qubit dynamics once the environment was completely characterized [Sec. 2.5]. **(b)** Fixed interpulse time $t_1 = 242$ ns (■ in **(a)**). The coherent oscillation is caused by the interaction with a nearby ^{13}C nuclear spin [Sec. 2.3.3]. The orange dashed line is a fitted damped cosine. **(c)** Fixed interpulse time $t_1 = 370$ ns (◆ in **(a)**) and $t_1 = 636$ ns (★ in **(a)**). The orange dashed line is the fit of an exponential decay $(1 + e^{-T/T_2^L})/2$. The generalized coherence time T_2^L [Sec. 2.3.1] is much shorter for t_1 values near the collapses caused by the NSD and the harmonics of the filter function.

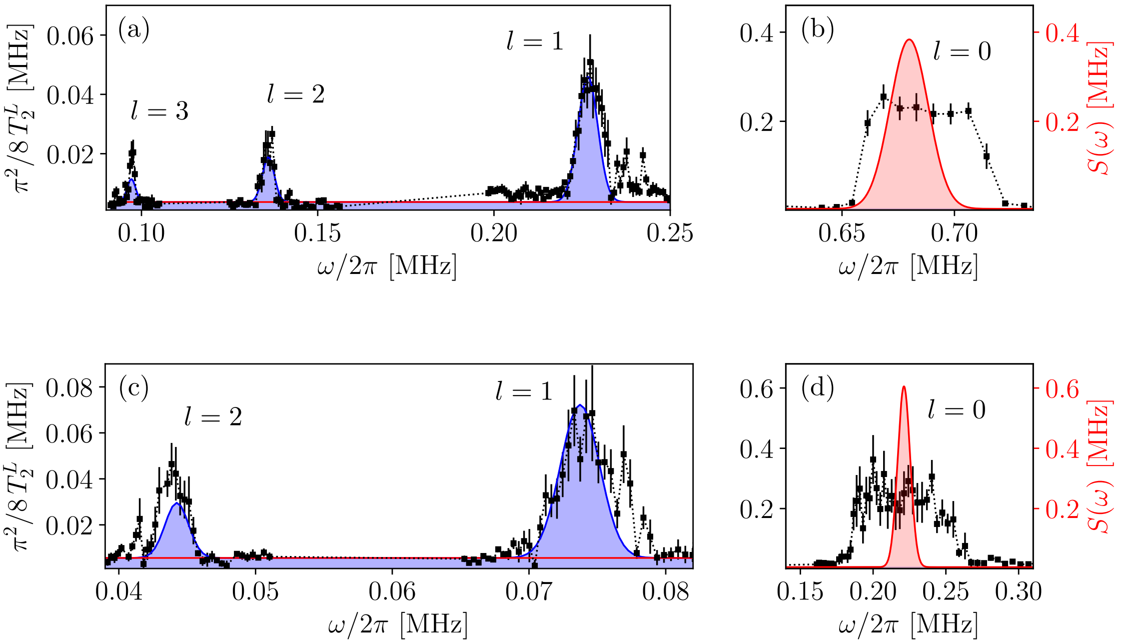

Figure 2.4: Measurement of $1/T_2^L$ as a function of $\omega = \pi/2t_1$, for $B = 635(1)$ G **(a-b)** and $B = 208(1)$ G **(c-d)**. Black dots are experimental $1/T_2^L$ values peaked at $\omega_L/(2l+1)$, with $l \in [0, 1, 2, 3]$. The blue line is a Gaussian distribution simultaneously fitted to the harmonics $l = 1, 2, 3$ or $l = 1, 2$, respectively for **(a)** or **(c)**, from which we extract $S(\omega)$ (red line) peaked at ω_L.

of a generalized coherence time T_2^L [88]

$$W(nt_1) = \exp\left(-\frac{2nt_1}{T_2^L}\right). \tag{2.22}$$

The decay is faster for t_1 corresponding to the spin bath characteristic frequencies (coherence collapses), as shown in Fig. 2.3(c). The analysis of the measured spin coherence for several different values of t_1 and n, enables the estimation of the generalized coherence time for each t_1 value. An example of the results of this analysis is shown in Fig. 2.4, where the fitted values of $1/T_2^L$ are displayed as a function of $\omega = \pi/2t_1$ (blue dots). On a first approximation, the filter function of equidistant DD sequences is a Dirac delta $Y_{n,T}(\omega) \propto \delta(\omega - \pi n/T)$, valid only for a large number of pulses. Under this assumption, and merging equations (2.2) and (2.22) we can write an approximated form of the NSD

$$S(\omega) \propto \frac{1}{T_2^L(\omega)}. \tag{2.23}$$

Then, a practical protocol would be to map out T_2^L varying t_1 around the first collapse, in order to reconstruct the NSD for frequencies near ω_L (see Fig. 2.4), where we expect the NSD distribution to be centered at. However, a strongly-coupled spin bath leads to very fast decay (already at $n < 8$) for t_1 around the first collapse, so that using large number of pulses is not possible. Unfortunately, for low number of pulses the filter function is too broad, which rules out the possibility to approximate $Y_{n,T}(\omega)$ as a delta function, and imposes the need of a more detailed analysis.

For a general DD sequence, the filter function [Eq. (2.3)] is written as [29, 112]

$$Y_n(\omega, T) = 1 + (-1)^{n+1} e^{i\omega T} + 2\sum_{j=1}^{n}(-1)^j e^{i\omega T\delta_j} \tag{2.24}$$

where n is the number of pulses, T is the total time, and δ_j represent the times when π-pulses are applied (by definition $\delta_0 \equiv 0$ and $\delta_{n+1} \equiv 1$). In the case of CP-based sequences, $\delta_j = j/(n+1)$, from which it is possible to derive [93]

$$Y_n(\omega, t_1) = 8\frac{\sin^4 \frac{\omega t_1}{2}\ \sin^2 n\omega t_1}{\cos^2 \omega t_1} \tag{2.25}$$

For a fixed interpulse time t_1, this filter function qualitatively works as a band-pass filter roughly centered at $\omega_0 \equiv \pi/2t_1$, with harmonics centered at $\omega_h \equiv (1+2h)\omega_0$ caused by the periodicity of the DD control sequence, where h is a non-negative integer defining the order of the harmonics. The FWHM of the these bands behaves as $1/n$, therefore for large n this filter function can be approximated to a Dirac comb with periodicity $\Delta\omega = \omega_0$. As a consequence, $T_2^L(\omega)$ is affected not only by $S(\omega)$, but also by higher harmonics [88, 89],[1]

$$\frac{1}{T_2^L(\omega)} = \frac{8}{\pi^2}\sum_{l=0}^{\infty}\frac{1}{(2l+1)^2}S(\omega_l), \tag{2.26}$$

giving the approximation in Eq. 2.23 for $l = 0$. Hence, given a specific NSD distribution centered at a given Larmor frequency ω_L, the distribution of $T_2^L(t_1)$ will show replicas of the NSD at $\omega_0 = \omega_L/(2h+1)$ with corresponding weights $1/(2h+1)^2$. An example of this is shown in Fig. 2.4, where the first two or three harmonics were measured. Another way to understand the effect of the harmonics of the filter function is via the collapses on the spin coherence. The first collapse occurs for t_1 values that are close to $\pi/2\omega$. This corresponds to the zero-order harmonic of the filter function. The consecutive collapses occur for $t_1 \simeq (1+2l)\pi/2\omega$, in correspondence with the higher harmonics of the filter function [Fig. 2.5].

Going back to the relation between T_2^L and the NSD. Equation (2.26) gives us a simple tool to overcome the limitation of the short coherence decay time in the collapses time windows: We center each of the higher order harmonics of the filter function around the expected NSD peak, and measure the generalized coherence time. This partially attenuates strong noise that would saturate the coherence decay and achieves a better approximation to a δ-function, as for fixed number of pulses the filter function gets narrower at higher orders [Fig. 2.5]. Finally we combine the information obtained from several harmonics in order to reconstruct the NSD. In other words, we fit an an expected shape of the NSD to the T_2^L data using a modified version of Eq. (2.26) where the infinite sum is truncated to $l_{\max}$, the highest harmonic that has been measured. Measuring higher harmonics implies increasing t_1, hence the number of achievable harmonics to be used during this characterization is limited by the relaxation time of the spin qubit. In the cases shown in Fig. 2.4, the first two or three harmonics were used to reconstruct the NSD. The measured NSD clearly shows a strong deviation from the T_2^L values for the zero order harmonic. In the following section we will demonstrate that $S(\omega)$ is correctly reconstructed from higher harmonics.

---

[1] Notice that the definition of $1/T_2^L(\omega)$ in Ref. [88] has an extra 1/2 factor. This is compensated with the same extra factor in the definition of the coherence function (compare Eq.(4) in Ref. [88] with Eq. (2.2)). Meaning that both conventions are self-consistent.

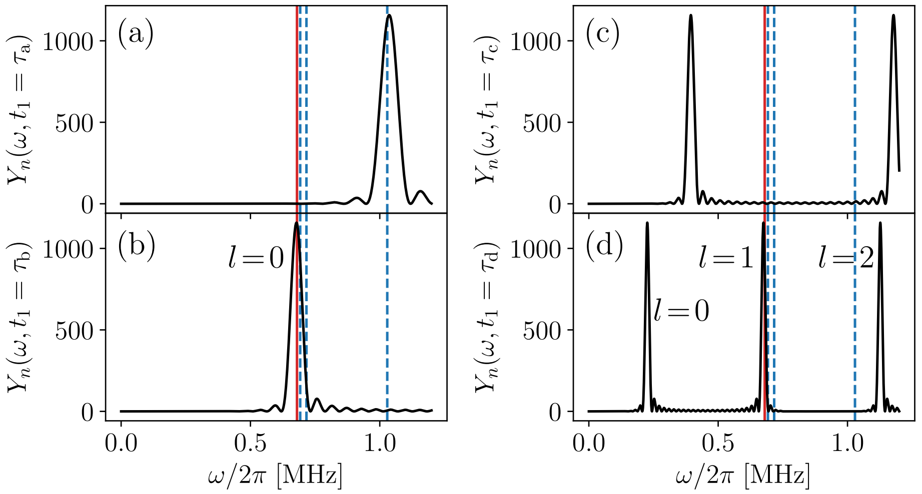

Figure 2.5: Study of the filter function for equidistant DD sequences [Eq. (2.25)] as a function of ω (with t_1 fixed and $n = 24$). The vertical red line marks ω_L for $B = 635$ G. The dashed blue lines is an anticipated result that correspond to $\omega_L + \omega_h^{||}/2$, for three different nuclear spins with parallel coupling strength component $\omega_h^{||}$ (see Sec. 2.3.3) The collapses in the spin coherence [Fig. 2.3(a)] occur when the filter function overlaps with either the red line (spin bath), or the blue lines (single nuclear spin). The interpulse time t_1 for each plot is **(a)** $\tau_\mathrm{a} = 242$ ns **(b)** $\tau_\mathrm{b} = 370$ ns **(c)** $\tau_\mathrm{c} = 636$ ns **(d)** $\tau_\mathrm{d} = 3\tau_\mathrm{b}$. The center of the filter function peaks moves towards lower frequencies when t_1 increases. The **(a)**, **(b)** and **(c)** cases correspond to the ■, ♦, and ★ markers in Fig. 2.3, respectively. The case **(d)** represents the collapse associated with the first order harmonic ($l = 1$).

The parameters that describe the NSD, for different magnetic fields, are listed on Table 2.1. They correspond to a Gaussian distribution

$$S(\nu) = y_0 + A\, e^{-(\nu-\nu_L)^2/(2\sigma^2)}, \tag{2.27}$$

where $\nu_L = \omega_L/(2\pi)$ is the Larmor frequency of the carbon nuclear spin bath.[2]

Table 2.1: Experimental results. Parameters obtained for the NSD peak using only the 0-th order collapse and using higher harmonics.

B-field [G]	Higher orders: 1^{st} & 2^{nd}			
	$y_0^\dagger$	$A^\dagger$	$\nu_L^\dagger$	$\sigma^\dagger$
635(1)*	0.0037(2)	0.38(5)	0.6799(8)	0.0085(7)
528(1)	0.0040(3)	0.48(7)	0.5647(7)	0.0062(6)
394(1)	0.0061(3)	0.42(6)	0.4220(6)	0.0048(5)
309(1)	0.0070(6)	0.53(7)	0.3306(6)	0.0059(5)
208(1)	0.0056(4)	0.60(8)	0.2212(4)	0.0043(4)

* For 635 G we also used the 3rd order harmonic.

† Values have units of MHz.

B-field [G]	0^{th}-order			
	$y_0^\dagger$	$A^\dagger$	$\nu_L^\dagger$	$\sigma^\dagger$
635(1)	0.0191(7)	0.35(8)	0.683(3)	0.018(2)
528(1)	0.0174(8)	0.16(3)	0.571(2)	0.019(2)
394(1)	0.0144(7)	0.25(4)	0.425(2)	0.017(1)
309(1)	0.0260(8)	0.21(3)	0.331(2)	0.018(1)
208(1)	0.016(1)	0.29(2)	0.223(1)	0.0187(8)

† Values have units of MHz.

Self-consistency of the method

To validate our protocol, we simulate the spin coherence $W_n^{\mathrm{d}}(T) = e^{-\chi_n(T)}$ (see Eq. (2.2)) under a simple noise model (a Gaussian centered at ω_L), and verify that $1/T_2^L$ obtained from the 0^{th}-order filter harmonics ($l = 0$) exhibits significant disagreement with the original spectrum, whereas the $l = 1, 2$ harmonics are sufficient to fully reconstruct the NSD peak.

We considered a Gaussian noise with NSD as in Eq. (2.27), with some preset parameters $[\nu_L, A, \sigma, y_0]$. We then calculated the temporal dependence of the spin coherence under control sequences with different numbers of equidistant pulses, as shown in Fig. 2.6(a). Finally we used this coherence to extract T_2^L values and reconstruct the simulated NSD with the same procedure used to treat the experimental data. This should prove the self-consistency of the method. As shown in Fig. 2.6(b-e), the 0^{th} order peak of the reconstructed spectrum from the simulated data exhibits significant disagreement from the original spectrum. Using instead the

---

[2] In appendix 2.H we show the parameters in the case of a Lorentz distribution. We chose the Gaussian distribution because the residuals were smaller.

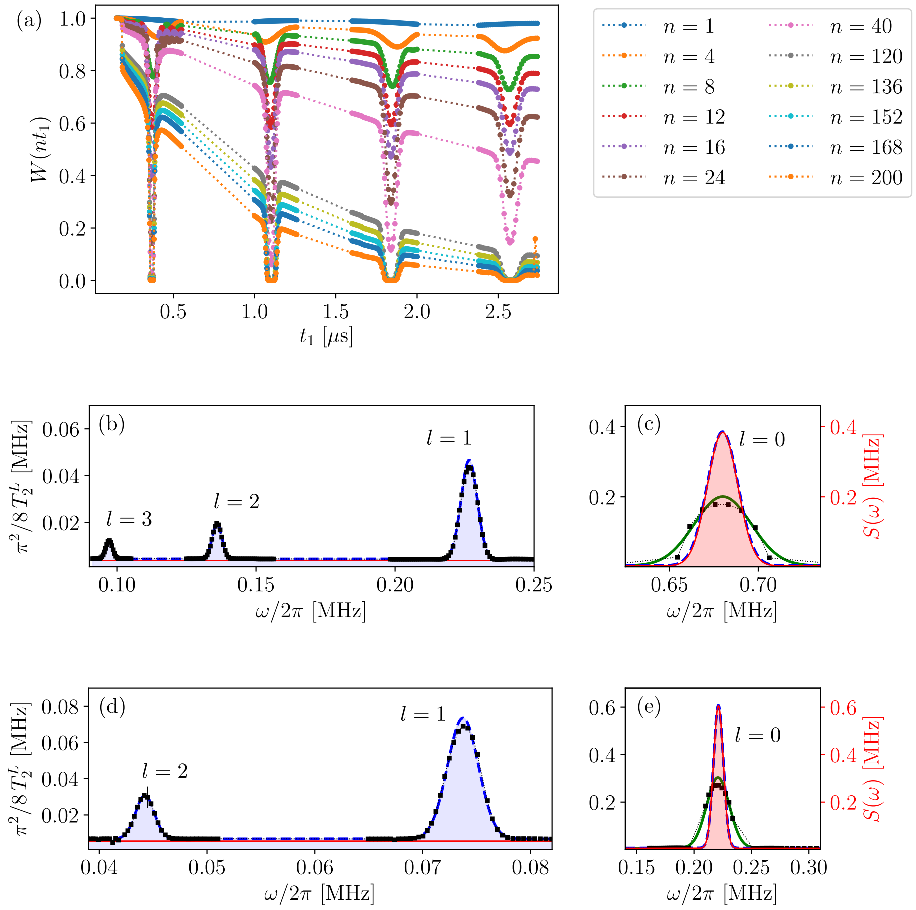

Figure 2.6: **(a)** Simulated coherence of the spin qubit under a DD sequence with n equidistant pulses. The simulation was done using Eq. (2.2) with a NSD given by Eq. (2.27) with the parameters in table 2.2 for $B = 635$ G. This simulation was treated as data to reconstruct the original NSD. **(b-e)** Reconstruction of a model NSD for $B = 635$ G **(b-c)** and $B = 208$ G **(d-e)**, used to proof self-consistency of the method. The black squares are $1/T_2^L$ values resulting from the fit of the simulated coherence. The dashed blue and solid green lines are the Gaussian fits to the harmonics of orders $l = 1, 2(, 3)$ and $l = 0$, respectively. The red line is the original model NSD. Clearly the dashed blue and solid red lines have a very good agreement, while the green line shows a strong deviation from the original model.

1^{st} and 2^{nd} harmonics we reliably reconstruct the NSD peak (see Table 2.2). From these results we can observe how the original NSD is not correctly reconstructed from the 0^{th}-order harmonic, meanwhile the first two harmonics are enough to obtain the NSD with good precision. We also performed the same analysis taking the first ten harmonics, with similar results. For the reconstruction, we simulated the coherence only for $n \geq 8$, including the points with $n < 8$ increases the percentage error on the estimated amplitude and width by a factor of 100 and 40, respectively. The estimation of the center was the same, within the error bars, in all cases.

Table 2.2: Comparison between three different simulated NSD and their correspondent reconstruction from the simulated data. The NSD is defined by its center $\nu_L = \omega_L/2\pi$, amplitude A, width σ and offset y_0. See Fig. 2.6 (c), and (e) for the $B = 635$ G, and $B = 208$ G cases, respectively.

		Original NSD	Reconstructed NSD	
			0^{th}-order	1^{st}&2^{nd}-orders
$B = 208$ G	ν_L †	221.2	220.8(1)	221.202(3)
	A †	600	297(5)	600.9(5)
	σ †	4.3	9.9(2)	4.304(3)
	y_0 †	5.6	6.23(4)	6.791(4)

† Values have units of kHz.

		Original NSD	Reconstructed NSD	
			0^{th}-order	1^{st}&2^{nd}-orders
$B = 635$ G	ν_L †	679.9	680(2)	679.91(4)
	A †	380	197(32)	381(2)
	σ †	8.5	16(3)	8.70(4)
	y_0 †	3.7	3.66(4)	4.337(2)

† Values have units of kHz.

		Original NSD	Reconstructed NSD		
			0^{th}-order	1^{st}&2^{nd}-orders	1^{st}–10^{th}-orders
$B = 700$ G	ν_L †	750	748(2)	750.0(2)	750.02(2)
	A †	600	266(34)	601(13)	603(1)
	σ †	9	21(4)	9.0(1)	9.01(2)
	y_0 †	5	5.00(5)	5.860(4)	5.983(2)

† Values have units of kHz.

In experiments, we extract the NSD lineshape from a Gaussian fit of $1/T_2^L$ around first and second order collapses. Figure 2.4(b,d) shows the obtained NSD lineshape (red line), compared with data from the 0^{th}-order collapse. We attribute the extra broadening of 0^{th}-order experimental data, compared with simulation, to the presence of the least-strongly-coupled among the observed nearby nuclei, as discussed in the Sec. 2.3.3. This carbon is clearly visible in higher-order harmonics, while is not resolved in the 0^{th}-order collapse, where it induces an overestimation of the NSD width.

2.3.2 NSD in the strong coupling regime

The critical magnetic field, where the transition towards the strong coupling regime occurs, is defined by $\omega_L = \gamma_n^{(C)} B \leq |\omega_h^{\perp}|$, being $\omega_h^{\perp}$ the orthogonal component of the coupling strength between the NV center and the closest ^{13}C nucleus. For a diamond with natural abundance of ^{13}C ($\sim 1\%$) the critical magnetic field is expected to be $B \approx 100$ G [96]. For the NV center used during this work, the value of this critical field should be $B \simeq 148\,\mathrm{kHz}/\gamma_n^{(C)} \simeq 140$ G [Tab. 2.4]. The measurements shown in the previous section [Sec. 2.3.1] were performed for fields above this value. In this section we will measure the NSD for lower magnetic fields, using the same protocol used before in order to compare the results.

Measuring the generalized coherence time T_2^L at low fields rapidly shows to be a challenge, since in a spin-echo signal we see a strong loss of coherence, as can be observed from the measurement of $P_{n=1}$ shown in Fig. 2.7(a). The collapses for equidistant DD sequences occur at interpulse times $t_1^{(l)} = \frac{1}{2\nu_L}(l + 1/2)$, where l is the order of the filter function harmonics. Already at $t_1^{(0)}$ the coherence has been reduced to almost one half. Moreover, the coherence has been completely lost for times between the collapses of even and odd harmonics. The presence of revivals still permits the measurement of the exponential decay of coherence for some specific t_1 windows, between odd and even collapses. Based on the results of Sec. 2.3.1, we are only interested in measuring the generalized coherence time T_2^L for harmonics $l > 0$. It is important to notice that for $n = 12$ pulses, the coherence was completely lost, so we were forced to use CP sequences with $n < 8$ in order to measure T_2^L. The results are shown in Fig. 2.7(b-c). From the data distribution, we expect to be able to extract a good estimation of the offset, center and width of the NSD. In contrast, we can expect a less precise estimation of the NSD amplitude with respect to higher magnetic fields. The estimated parameters for the NSD are shown in table 2.3, which are complementary to the cases for the weak coupling regime shown in table 2.1. In Sec. 2.4 we will compare the results obtained in both regimes.

Table 2.3: Parameters obtained for the NSD peak in the strong coupling regime, extracted from partial measurements of T_2^L [Fig. 2.7].

B-field [G]	$y_0^\dagger$	$A^\dagger$	$\nu_L^\dagger$	$\sigma^\dagger$
78(1)	0.0072(5)	1.3(6)	0.0826(4)	0.0038(5)
132(1)	0.0080(8)	0.9(2)	0.1435(8)	0.006(1)

† Values have units of MHz.

2.3.3 Characterization of resolved nuclear spins

The reconstruction of the NSD from a classical model fails in some narrow time windows, where the coherence presents sharp dips reaching even negative values ($P_n < 0.5$). This allows us to identify the coherent coupling of the NV spin to a local

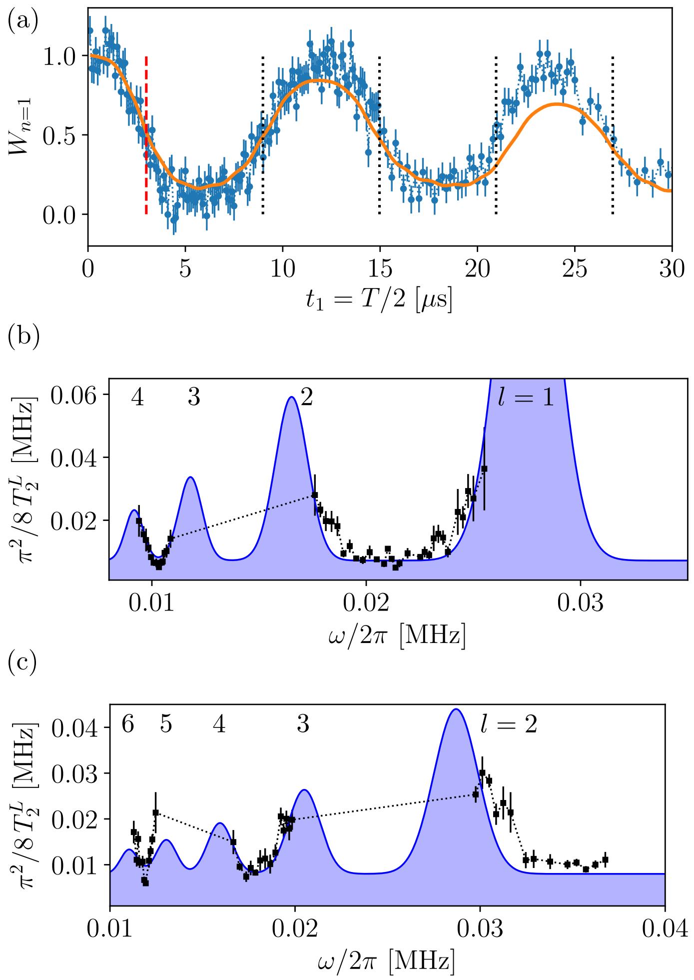

Figure 2.7: **(a)** Measured coherence of the spin qubit under a spin-echo (SE) sequence for an external magnetic field $B = (78 \pm 1)$ G. At this field, the zero-th order collapse occurs at $t_1^{(0)} = (2.99 \pm 0.04)$ μs (red dashed line). The next four orders (black dashed lines) were used to measure the generalized coherence time T_2^L. The orange line is a simulation of the spin qubit dynamics once the environment was completely characterized [Sec. 2.5]. **(b)-(c)** T_2^L measured values for $B = (78 \pm 1)$ G and $B = (132 \pm 1)$ G, respectively. The blue line is a fit for Eq. (2.26) used to estimate the NSD parameters. The order l of the harmonics used for the fit are indicated in each plot.

small quantum environment, which becomes visible as the equispaced DD sequences partially filter out the larger spin bath. The hyperfine interaction to single proximal nuclear spins (Eq. 2.4) induces different phases for the two states $|\pm\rangle = (|0\rangle \pm |-1\rangle)/\sqrt{2}$ during the spin evolution time [23–25]. The residual NV spin coherence then presents coherent modulations as a function of the pulse number [Fig. 2.3(b)], which give information on the hyperfine coupling tensor between the NV spin and nearby nuclear spins. In particular, the interpulse time $t_1^{(\mathrm{hf};\,l)}$ at which these coherent evolutions are present (see ■ in Fig. 2.3) allows us to obtain an estimate of the energy-conserving component of the coupling strength, $\omega_h^{||} = \frac{(2l+1)\pi}{t_1^{(\mathrm{hf};\,l)}} - 2\omega_L$ [24], where $l = 0, 1, 2, \dots$ is the order of the harmonics. By fitting the modulations with a periodic function $M_n^{(\mathrm{CP})}(T)$ [Eq. (2.16)], we extract a refined estimate of the parallel and orthogonal components of the coupling strength for three different ^{13}C nuclei (see Table 2.4). Note that we treat each coherently coupled ^{13}C spin separately, since nuclear-nuclear spins couplings are negligible. A more detailed analysis (see e.g. refs. [21, 33]) could be used to identify as well couplings between nuclear spins if they are strong enough to affect the dynamics.

Table 2.4: Coupling components of the NV spin to three ^{13}C nuclei.

$\omega_h^{\|\|}/2\pi$ [kHz]	$\omega_h^{\perp}/2\pi$ [kHz]
-698 ± 8	148 ± 13
-73 ± 4	59 ± 3
-25 ± 2	42 ± 1

The modulation amplitude shows sharp peaks as a function of frequency [Fig. 2.8]. Notice that for the third carbon, the least strongly coupled to the NV, the amplitude of the modulation is centered very close to the Larmor frequency. As mentioned in the previous section, this may induce extra broadening in the estimation of the NSD when using 0^{th}-order of the filter function. In addition, only the more strongly coupled nucleus is visible with a Ramsey experiment, which gives a consistent but less precise estimate of the coupling strength.

Characterizing the spin environment of a qubit is critical to achieve improved error correction protocols. One could, e.g., exploit the coherently coupled nuclear spins in the environment to create quantum error correction codes [113–116], that could be further tailored to the measured noise spectrum [31]. An alternative strategy is to optimize dynamical decoupling sequences [29, 117–120], for example to allow both noise suppression and quantum sensing [28]. It is then essential to test whether the reconstructed environment model has predictive power, as we will do in Sec. 2.5.

2.4 Limits of the classical noise model

Having devised a practical protocol to reconstruct the NV environment, we implement it at different magnetic field intensities, where either classical or quantum properties of the bath are expected to be visible [96]. While we expect the spin bath effects on a central spin qubit to be always described by a classic noise source model [111], noise spectroscopy allows us to mark the boundary between quantum and classical regime. The bias magnetic field applied along the NV spin not only

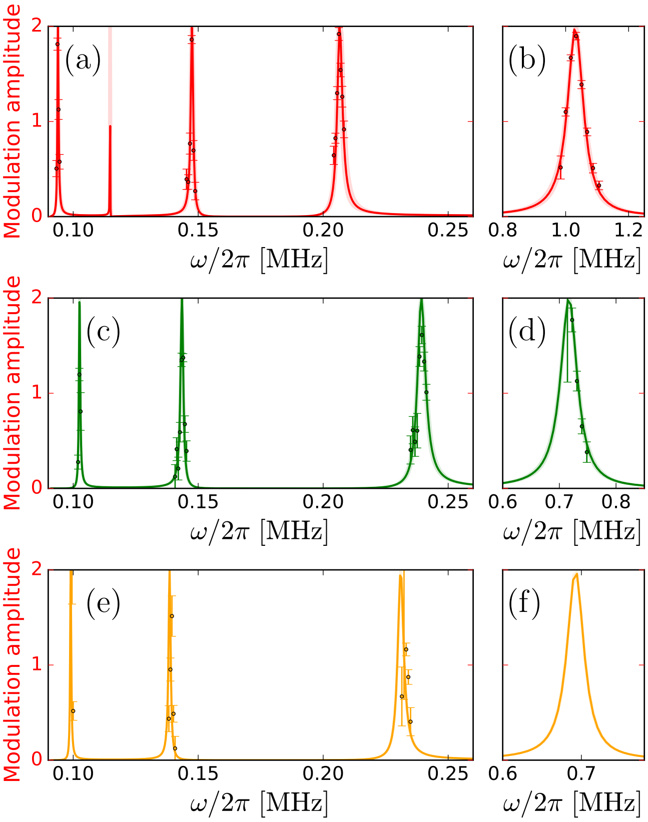

Figure 2.8: Amplitude of the observed coherent modulations, at $B = (635 \pm 1)$ G. The points represent the experimental data and the lines represent the simulation after the characterization of $\omega_h^{\parallel}$ and $\omega_h^{\perp}$, using Eq. (2.16). The colors red, green and orange represent the different nearby carbons, following the same order than the Table 2.4. Panels **(b)**, **(d)** and **(f)** show the modulation for the 0^{th}-order harmonic of the filter function; **(a)**, **(c)** and **(e)** show the modulation amplitudes for higher harmonics of the filter function. Note that the third carbon is so weakly coupled to the NV spin, that the 0^{th}-order is not distinguishable from the bath (see Fig. 2.5), which is why there are no data points in **(f)**. The presence of this carbon also influences the strong extra-broadening of the data in Fig. 2.4(b). Adapted from [77].

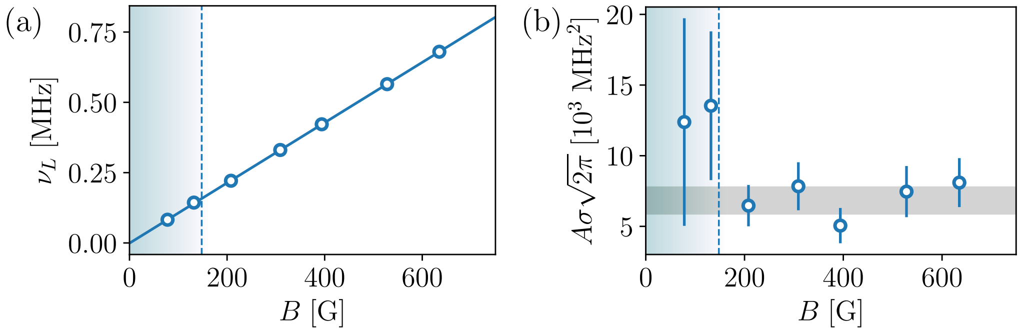

Figure 2.9: **(a-b)** Properties of the measured NSD peak across the quantum-to-classical spin bath transition. Peak position **(a)**, and area **(b)**, obtained from a Gaussian fit of the measured NSD, and reported as a function of the magnetic field strength. The blue line in **(a)** is a linear fit, consistent with the expected coupling frequency for a ^{13}C spin bath. The vertical dashed line represents a guide for the eye indicating a sudden change of the bath behavior–where the condition $R \gg 1$ is no longer fulfilled. The gray horizontal region in **(b)** denotes the mean value $\bar{a}$ and standard deviation σ_a of the NSD area for $B > 150$ G. Values at field $B < 150$ G deviate from $\bar{a}$ by $> 6\sigma_a$. Adapted from [77].

changes the NSD central frequency (^{13}C Larmor frequency ω_L), but also its properties. In Fig. 2.9 we plot peak center, and area of the measured $S(\omega)$. The center scales linearly with the magnetic field, with a slope of 1.069(2) kHz/G, the gyromagnetic ratio of ^{13}C [Fig. 2.9(a)]. Remarkably instead, the NSD area [Fig. 2.9(b)] show a discontinuity at $B \sim 150$ G, where $R \equiv \omega_h^{\perp}/\omega_L \sim 1$, indicating a sudden change in the bath properties that we can associate with the boundary between the quantum and classical regimes.

In the weak coupling regime, when $R \ll 1$ for most nuclei, the unpolarized nuclear bath can be described as formed by classical randomly-oriented magnetic dipoles, as shown in Sec. 2.2.2. The orthogonal component of each nuclear dipole $\sigma_n^{\perp}$ undergoes Larmor precession around the external magnetic field. The coupling to the spin qubit thus assumes the form of an effective dephasing Hamiltonian $\mathcal{H} = \gamma\beta(t)\sigma_z^{\mathrm{NV}}$ with $\beta(t)$ a time-varying mean field with stochastic amplitude and phase, which can be characterized by its NSD. In the following section, we will demonstrate this by using the parameters of the NSD to simulate the NV spin dynamics and comparing the result with experimental data.

In the strong-coupling regime, at $B \leq 150$ G, we expect the bath dynamics to be modified by the controlled NV dynamics due to the back action of the NV onto the bath itself. The characterization of the environment using a full quantum description would be a very difficult task. A system formed by a large number of nuclear spins that interact with an NV center, and with each other is by itself a very complex system to describe. Instead, as will be shown in Sec. 2.5.3, two different classical models are enough to predict the NV spin dynamics, under a set of different control fields, in the strong coupling regime.

2.5 Predicted spin dynamics

Having gained in principle a full picture of the NV spin environment – noise spectrum of the bath and coherent interaction with nearby impurities, we want to confirm this to be a predictive model of the spin evolution under different kinds of time-dependent control, beyond monochromatic filters. We thus use the measured spectrum and hyperfine couplings to simulate the spin coherence under different kinds of DD sequences, and we compare this prediction to measurements.

We calculate the residual coherence after a given n-pulse sequence, P_n, as due to both the spin bath and the $m = 3$ observed strongly-coupled single spins,

$$P_n(T) = \frac{1}{2}\left(1 + e^{-\chi_n(T)} \prod_{i=1}^{m} M_n^{(i)}(T)\right). \tag{2.28}$$

Here, $\chi_n(T)$ is obtained from the measured NSD for the correspondent magnetic field, whereas $M_n(T)$ is extracted by evolving the spin under conditional evolution operators, using Eq. (2.15) and the coupling strengths reported in table 2.4.

In Sec. 2.5.1 we show the case of equidistant pulses. In Sec. 2.5.2, we will show the case of a couple of important non equidistant DD sequences [76].

2.5.1 Equidistant DD sequences predictions

As a preliminary test for the prediction capabilities of the characterized environment, we compared the simulated dynamics under equidistant DD sequences with the experimental data, obtaining a very good agreement [Fig. 2.10(a-b)]. In addition, we exploited the spin triplet nature of the NV center to further validate the fact that the reconstructed environment model is predictive independently of the qubit properties, that is, the environment model extracted from the dynamics of the the two spin states $|0\rangle$ and $|-1\rangle$ can predict also the dynamics of the $m_s = \{0, +1\}$ [Fig. 2.10(c)]. It is worth mentioning that all these datasets (and a second set shown in Fig. 2.14) were obtained for DD sequences as the ones used to characterize the environment, however non of these were directly used to fit the NSD parameters or the hyperfine coupling strengths.

2.5.2 Non equidistant DD sequences predictions

DD sequences of equidistant pulses may exhibit suboptimal performances in several cases, for example when probing multitone target fields due to attenuation of some frequency components. Thus, DD has been further developed by introducing non-equispaced and concatenated sequences. In this section we demonstrate the predictive capabilities of the characterized environment for two different non-equidistant DD sequences.

The Uhrig DD (UDD) protocol [29], composed by a set of n π-pulses with interpulse delay time $\delta_j = \sin^2[\pi j/(2n+2)]$ and $j \in \{1, \ldots, n\}$, has been successfully employed to detect ^{13}C dimers [21] inside diamond, as it highly suppresses the effect of coupling to single nearby nuclei. The dynamics of the NV spin under a UDD sequence with $n = 32$ pulses is shown in Fig. 2.11, together with the time distribution of pulses and an example of the associated filter function.

A recent proposal is the adaptive XY-N (AXY-N) [121], composed by N blocks —Knill pulses—each containing five π pulses with rotated phases [121, 122]. As

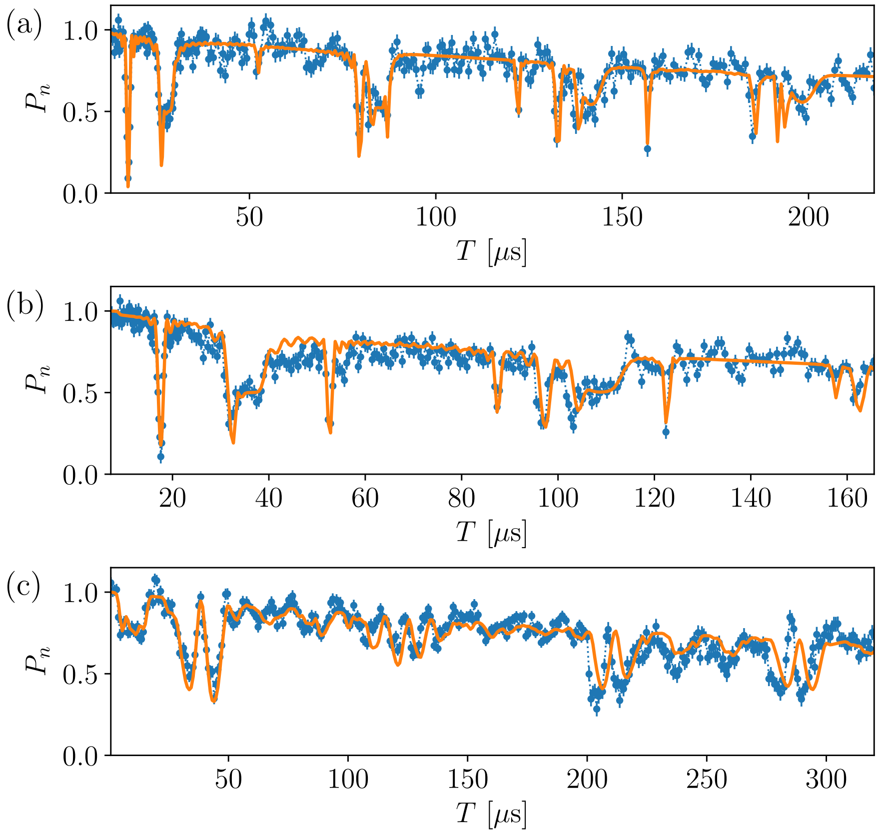

Figure 2.10: Time evolution of spin coherence under equidistant DD sequences. Dots are experimental data with statistical error. Orange lines are the predicted coherence simulated using the measured environment, with no free parameters. **(a)** Four repetitions of XY-8 ($n = 32$) for $B = (528 \pm 1)$ G. **(b)** Three repetitions of XY-8 ($n = 24$) for $B = (309 \pm 1)$ G. **(c)** XY-4 ($n = 4$) for $B = (394 \pm 1)$ G with the two level system formed by $\{|0\rangle, |+1\rangle\}$. This is the only set of data in this chapter that uses the positive NV spin projection to form a qubit. Notice that the simulation was done using the NSD parameters, and hyperfine coupling strengths characterized with the $\{|0\rangle, |-1\rangle\}$ qubit.

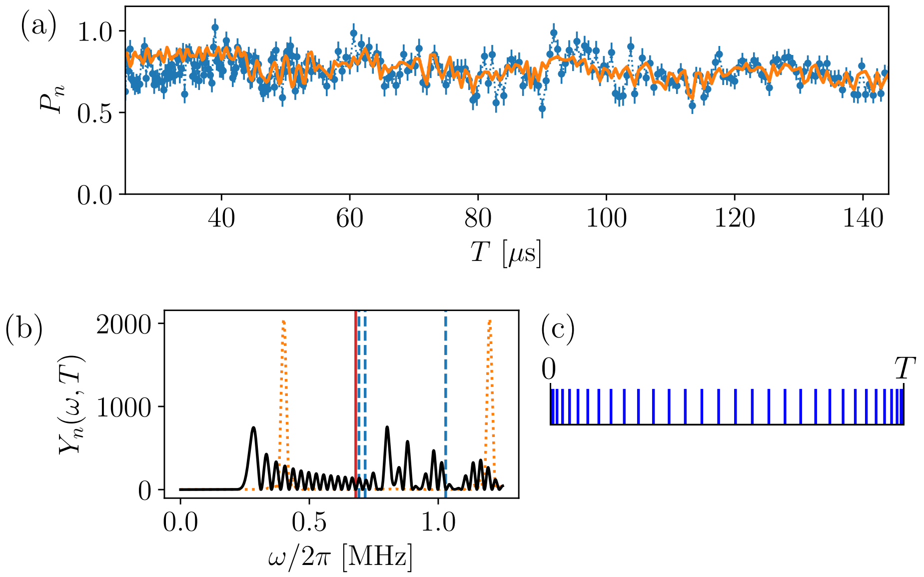

Figure 2.11: **(a)** Spin coherence dynamics under a UDD sequence with $n = 32$ pulses for $B = 635$ G. Dots are experimental data with statistical error. Orange lines are the predicted coherence simulated using the measured environment, with no free parameters. **(b)** Filter function for a UDD sequence with $n = 32$ and $T = 40$ μs. The vertical red line marks ω_L for $B = 635$ G. The dashed blue lines correspond to $\omega_L + \omega_h^{||}/2$, for the three nearby nuclear spins. The orange dashed line is the filter function for a CP sequence for the same $n = 32$ and $T = 40$ μs, as reference. **(c)** Time distribution of π pulses for the same $n = 32$ UDD sequence.

mentioned before, carefully selecting the relative phase between pulses improves the robustness against pulse errors. The phase distribution of the pulses in each block is:

$$\Pi_\phi = \pi_{\phi+\pi/6} \; - \; \pi_\phi \; - \; \pi_{\phi+\pi/2} \; - \; \pi_\phi \; - \; \pi_{\phi+\pi/6} \tag{2.29}$$

to form the AXY-8 sequence, the eight blocks must be:

$$\Pi_X \; - \; \Pi_Y \; - \; \Pi_X \; - \; \Pi_Y \; - \; \Pi_Y \; - \; \Pi_X \; - \; \Pi_Y \; - \; \Pi_X \tag{2.30}$$

Since the blocks are equidistant, and we decided to use a Knill pulse with five equidistant π pulses, then the time distribution of the $N \times M$ pulses corresponds to the sequence reported in Ref. [123], which was conceived specifically to facilitate the discrimination of single nuclear spins. The position in time for each π-pulse is given by $t_{i,j}(r_m) = (1/\mathcal{N}) \left(\frac{2i-1}{2} + r_m \frac{2j-\mathcal{M}-1}{2\mathcal{M}}\right)$ where $\mathcal{M} = 5$ is the number of pulses inside each block and $\mathcal{N}$ is the number of blocks, $i \in \{1, \ldots, \mathcal{N}\}$, $j \in \{1, \ldots, \mathcal{M}\}$, and r_m defines how close within each other are the pulses inside each block. With $r_m = 1$ the $N \times M$ pulses are equidistant, whereas the limit of $r_m = 0$ corresponds to N π pulses (each one formed by the superposition of five pulses). In Figure 2.12 we show the case of AXY-8 for $r_m = 1.0$, 0.75, 0.5, and 0.25, and AXY-4 for $r_m = 0.75$. We have verified that, as expected, AXY-8 and XY-8 are more robust compared to CPMG and XY-4 against detuning and pulse shape imperfections, which our simulations do not take into account.

At high field, the excellent agreement between data and simulations (see also inset of Fig. 2.15, circles) demonstrates that the spin bath can be described independently of the NV dynamics, since the coupling of the NV center to the spin bath can be neglected compared to the bath internal energy.

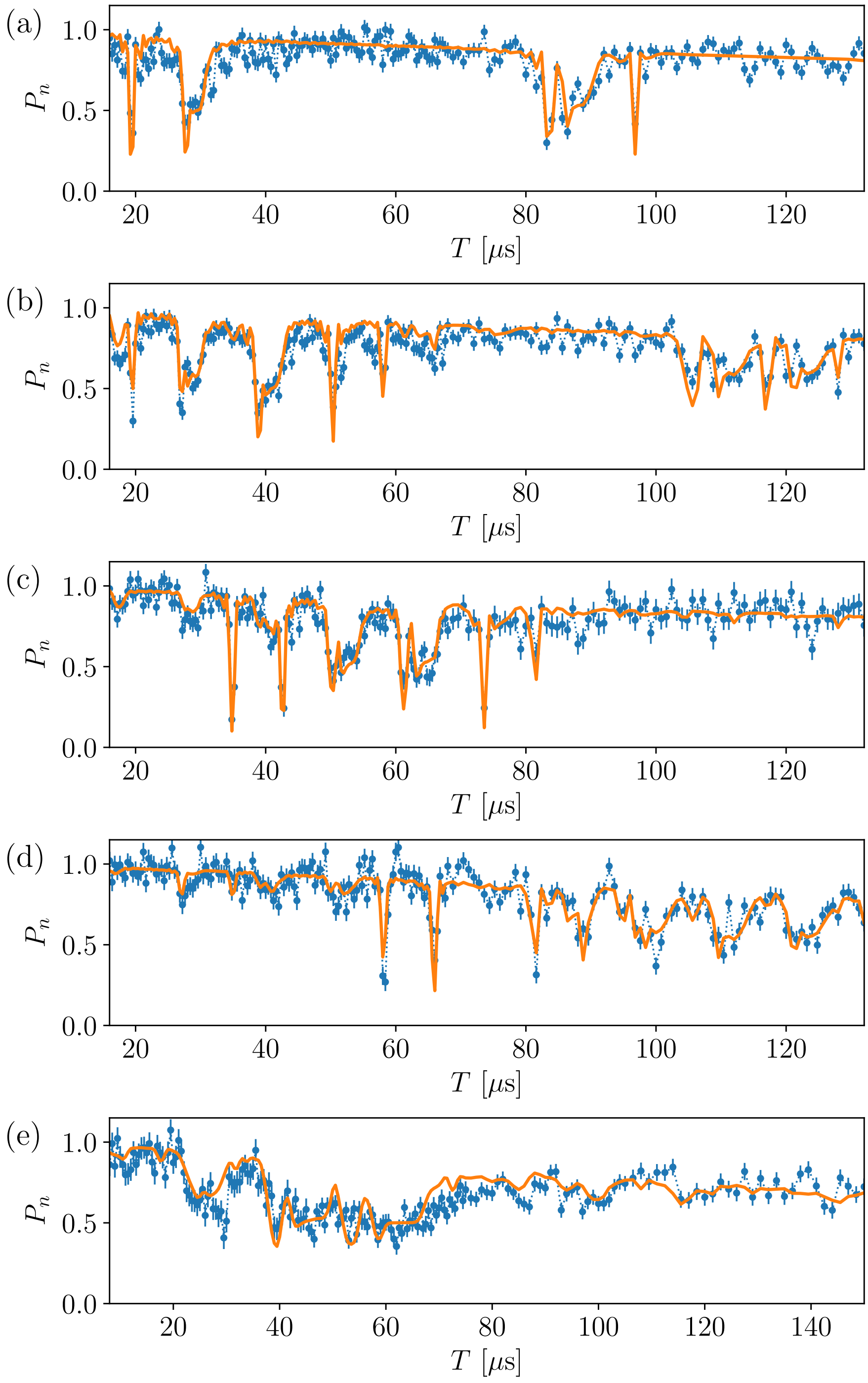

Figure 2.12: Time evolution of spin coherence for different cases of AXY-N sequences at field **(a-d)** $B = (635 \pm 1)$ G or **(e)** $B = (208 \pm 1)$ G. The dots are the experimental data, and the orange line is the predicted dynamics using the measured environment, with no free parameters. The interpulse time is defined by the parameter r_m (see text). **(a)** AXY-8 (40 pulses) with $r_m = 1.0$. **(b)** AXY-8 (40 pulses) with $r_m = 0.75$. **(c)** AXY-8 (40 pulses) with $r_m = 0.5$. **(d)** AXY-8 (40 pulses) with $r_m = 0.25$. **(b)** AXY-4 (20 pulses) with $r_m = 0.75$.

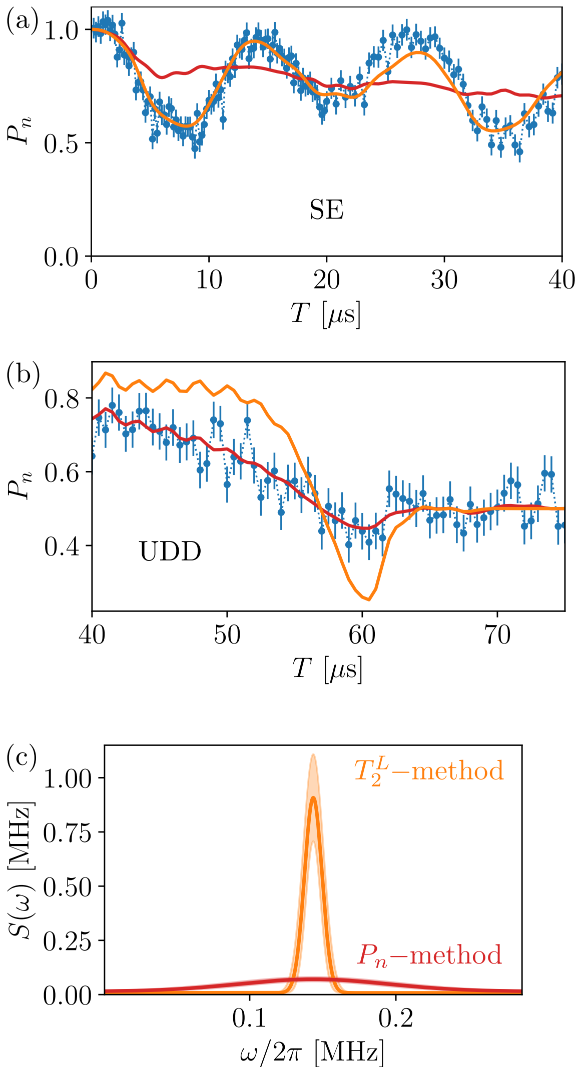

Figure 2.13: Time evolution of spin coherence under **(a)** spin-echo and **(b)** Uhrig $n = 32$, in the strong coupling regime ($B = 132(1)$ G). Dots are experimental data with statistical error. Solid lines are the predicted coherence simulated using the two different NSDs: **(c)** NSD obtained from the measurement of T_2^L (orange) and NSD obtained from the direct fit of P_n (red). The shaded area represent the errorbars on the parameters that describe the Gaussian peak.

2.5.3 Strong coupling regime

As mentioned in 2.4, at fields $B \leq 150$ G, we expect that the loss of NV coherence is due to the creation of entanglement between NV spin and the large environment: In this strong-coupling regime, the environment description in terms of classic noise is no longer valid [96], and the dynamics of the nuclear spin environment itself is affected by the control applied to the NV center electronic spin, due to the NV back action [77]. Indeed, we observe that the NSD measured with equispaced sequences does not predict correctly the measured coherence independently of the applied control [Fig. 2.13(orange)]. The NSD extracted with the T_2^L method correctly describes the coherence for DD sequences with small n numbers (e.g. Hahn echo), but it fails to predict the dynamics for other DD sequences (e.g. UDD). In other words, one single classical model is no longer suitable to describe the bath when the NV dynamics is driven by different kinds of DD sequences. However, since the NV spin is a simple

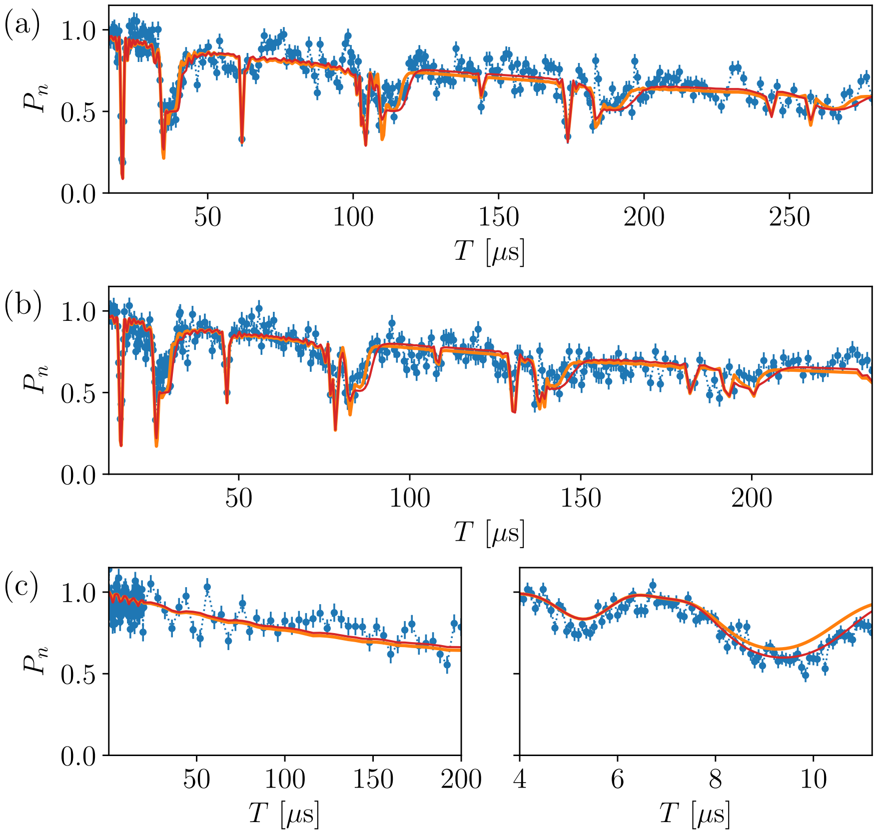

Figure 2.14: Comparison between two NSD models in the weak coupling regime: $B = (394 \pm 1)$ G. Dots are experimental data with statistical error. Solid lines are the predicted coherence simulated using the NSD obtained from the measurement of T_2^L (orange) and using the NSD obtained from the direct fit of P_n (red). **(a)** Four repetitions of XY-8 ($n = 32$). **(b)** Three repetitions of XY-8 ($n = 24$). **(c)** Left panel: SE ($n = 1$). Right panel: XY-8 ($n = 8$).

two-level system, once fixed the control sequence acting on the NV spin we should be able to find a classical model of the spin bath [111] (we note that we are still able to correctly model the contribution from the coherently coupled nuclear spins using the same parameters and Hamiltonian as in the high-field regime). We have found that two classical noise spectra are enough to achieve predictive results. The first one being the NSD extracted via the measurement of T_2^L. This model effectively predicts the NV spin dynamics under sequences with small n that have broad filter functions, less sensitive to the shape of the NSD. The second NSD is obtained by direct fit of P_n under different multi-pulse controls. The fitted parameters are offset, amplitude and width, while we fix the NSD center given by the Larmor frequency $\nu_L = B\gamma_{C_{13}}$. The alternative NSD line shape correctly predicts the dynamics for sequences with $n \geq 20$, but it fails for sequences with low number of pulses, like Hahn-echo or CPMG with $n = 2$ [Fig. 2.13(red)]. In the strong-coupling regime, both methods result in NSD peak functions that are significantly different from each other, as shown in Fig. 2.13(c). Conversely, this is not the case for the weak-coupling regime, where the two noise models effectively predict the spin dynamics for low and high n values, as shown in Fig. 2.14.

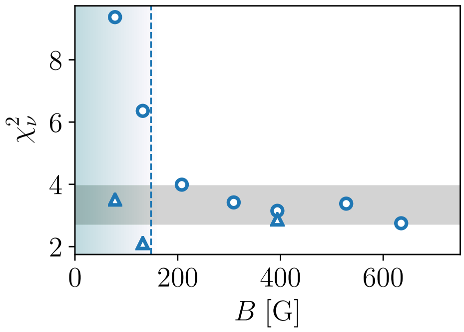

Figure 2.15: Mean-squared-residuals of the experimentally observed coherence with the simulation obtained from the measured NSD (circles) and with the two-model simulation (triangles). Each point results from several datasets collected under different controls [Tab. 2.5]. Adapted from [77].

2.5.4 Quantitative analysis of the prediction capability

The predictive power of the model can be estimated quantitatively by calculating the mean-squared-residuals (defined as the reduced chi squared) between simulation and experimental data:

$$\chi^2_{\{N-1\}} = \frac{1}{N-1} \sum_{i=1}^{N} \frac{(s_i - y_i)^2}{\delta_i^2} \tag{2.31}$$

where N is the number of data points, y_i are the experimental values of P_n with statistical error δ_i, calculated over 10^5 measurements, and s_i are the points simulated under the same conditions as the experimental data, using Eq. (2.28). For each different magnetic field, we take into account different kinds of DD sequences in order to calculate the residuals of all of them at once. For example, at 635(1) G we obtain the mean-squared-residuals from four datasets of AXY-8 together with one dataset of an Uhrig (UDD) sequence, as shown in Fig. 2.12 and Fig. 2.11, respectively. A second example is shown in Fig. 2.10, where the experimental data together with the simulation are shown for $B = 394(1)$ G.

Performing this kind of analysis for all the investigated magnetic field intensities, we obtain χ^2_ν with respect to the NSD obtained by measuring T_2^L, shown as circles in Fig. 2.15. It is important to notice that the values of the mean-squared-residuals increase strongly for low magnetic fields – yet another signature of the quantum-to-classical transition. The triangles in Fig. 2.15 are calculated by evaluating the residuals using the T_2^L-based NSD for sequences with low number of pulses, and the alternative NSD for sequences with high n values. This demonstrate that in the strong coupling regime, two classical models suffice to describe the dynamics of the spin qubit under the DD sequences used in this work. We note that for $B = 394(1)$ G – in the weak coupling regime, using this two-model picture results in values of χ^2_ν comparable to the ones obtained from the T_2^L-based NSD measurement.

A summary of the DD sequences used to calculate the values of χ^2_ν is shown in appendix 2.G.

2.6 Conclusions

We have experimentally demonstrated a method to spectrally characterize the nuclear spin environment of NV centers, even when the resulting NV coherence time is short. The environment comprised both nearby nuclei, that induce coherent modulations, as well as a larger ensemble of nuclear spins, which we aim to model with a classical bath. Our method enables the identification of the characteristic parameters of both components of the environment (Hamiltonian of nearby nuclei and NSD of the bath). The reconstruction of the full environment model can be then used to predict the NV coherence even when the spin dynamics is driven by different kinds of control.

In a weak coupling regime, at high magnetic fields, the environment model fully predicts the measured spin coherence under various control sequences. At low magnetic fields, where the quantum dynamics of the nuclear spin bath is expected to have larger influence, we can still identify a classical noise model describing the NV central spin decoherence, even if decoherence is fundamentally induced by the nuclear spin bath via entanglement with the NV center. However, due to the control-driven qubit back action on the bath, the classical noise model is not generally predictive, and we find that different environment models are needed to describe the evolution under different types of applied controls.

By studying the validity and limits of a robust environment characterization protocol, able to address a complex quantum environment and provide a simplified (classical) model, our results pave the way to more robust quantum devices, protected by noise-tailored error correction techniques.

2.G Appendix: Summary of sequences used to calculate mean-squared-residuals

Table 2.5: Summary of the data sets used to extract the mean-squared-residuals, in terms of the external magnetic field. The χ^2_ν values resulting from comparison between simulation and experiment are shown as squares in Fig. 2.15. Note that these datasets doesn't include the experiments used to characterize the NSD using the T_2^L method.

B-field [G]	Base DD sequence	number of pulses
635(1)	UDD	32
	AXY-8 ($r_m = 1$)	40
	AXY-8 ($r_m = 0.75$)	40
	AXY-8 ($r_m = 0.5$)	40
	AXY-8 ($r_m = 0.25$)	40
528(1)	XY-8	8
	XY-8	24
	XY-8	32
	UDD	32
	XY-8	48
394(1)	SE	1
	XY-8	8
	YX-8	24
	YX-8	32
309(1)	YX-8	24
208(1)	AXY-4 ($r_m = 0.75$)	20
	YX-8	24
132(1)	SE†	1
	AXY4† ($r_m = 1$)	20
	AXY4† ($r_m = 0.75$)	20
	UDD†	32
	UDD	32
	AXY8† ($r_m = 1$)	40
	AXY8† ($r_m = 0.75$)	40
78(1)	SE	1
	CPMG	2
	AXY4 ($r_m = 1$)	20
	AXY4 ($r_m = 0.75$)	20
	UDD	32
	AXY8 ($r_m = 1$)	40
	AXY8 ($r_m = 0.75$)	40

† Using the $\{|0\rangle, |+1\rangle\}$ qubit.

2.H Appendix: Lorentzian NSD

Here we report in Table 2.6 the parameters that describe the NSD, for different magnetic fields, assuming that the NSD follows a Lorentzian distribution. Notice that throughout this chapter we have used the Gaussian distribution parameters described in tables 2.1 and 2.3.

Table 2.6: Experimental results. Fitted parameters for a NSD peak with a Lorentzian function $S^{(\mathrm{L})}(\nu) = y_0 + a(2/\pi)w/(4(\nu - \nu_L)^2 + w^2)$, where w is the FWHM, and a is the amplitude. The parameters shown in this table are the result of a fit to the same datasets used for tables 2.1 and 2.3.

B-field [G]	$y_0^\dagger$	$a^\dagger$	$\nu_L^\dagger$	$w^\dagger$
635(1)	0.0028(2)	0.46(6)	0.6806(8)	0.016(2)
528(1)	0.0033(4)	0.6(1)	0.5654(7)	0.010(2)
394(1)	0.0056(4)	0.6(2)	0.4228(6)	0.006(1)
309(1)	0.0057(7)	0.6(1)	0.3314(7)	0.009(2)
208(1)	0.0038(6)	0.6(1)	0.2214(5)	0.008(1)
132(1)	0.006(1)	1.1(6)	0.1436(8)	0.011(5)
78(1)	0.0068(8)	1.2(6)	0.086(1)	0.004(2)

† Values have units of MHz.

Part II

Quantum thermodynamics

Chapter 3

Introduction to quantum fluctuation relations

The development of state-of-the-art technology at the nanoscale can shine new light on fundamental problems concerning the connection of quantum information and thermodynamics in open quantum systems, and bring to the realization of novel devices such as quantum thermal machines [18, 48] and quantum batteries [124–126]. In nanoscale quantum systems, classical and quantum fluctuations play a paramount role in the dynamics and affect many physical and thermodynamic quantities of interest. Work, heat, and entropy are stochastic variables, in nanoscale quantum systems, as opposed to large systems, where they are deterministic variables.

While systems at equilibrium or near equilibrium are well known to satisfy the universal fluctuation-dissipation theorem [127, 128], far from equilibrium systems have been subject of study for several decades. This extensive work has brought to the formalization of different Fluctuation Relations (FR) [129, 130] and later to their extension to the Quantum Fluctuation Relations (QFR) [131–133], which describe far-from-equilibrium processes by connecting the out-of-equilibrium thermodynamic quantities with the properties of the equilibrium initial and final states. A remarkable example of these relations is the celebrated Jarzynski equality, which recasts the second law of thermodynamics for closed systems, by connecting work and free energy variation in out-of-equilibrium thermodynamic processes through an equality that takes into account all the possible microscopic trajectories. However, the experimental study of quantum FRs and quantum thermodynamic properties at the nanoscale represents a difficult task. An evidence of this is the very limited set of different experimental platforms that have been used to this goal.

The second part of this thesis is dedicated to a study of energy exchange fluctuation relations in open quantum systems, based on the NV center in diamond as experimental platform. The research presented here, together with the published material in Refs. [19, 58, 134], represent the very first study of this type with NV centers.

This chapter presents the basic concepts of this field of research, relevant to chapters 4, and 5. Section 3.1 contains a brief discussion about the connection between information theory and thermodynamics, both classic and quantum. Section 3.2 provides an introduction to the original formulation of FRs for classical settings, and the connection with their quantum counterparts. Section 3.3 contains the main concepts and tools used to understand QFRs, and their operative definition. Finally, in section 3.4, I briefly review the experimental studies of QFRs that, to date and to the best of my knowledge, have been performed on different quantum platforms.

3.1 Information and thermodynamics

A strong connection between information theory and thermodynamics has been already established in classical physics, and has further thrived in the framework of quantum physics [39, 40, 135, 136]. As a glaring example, the resources consumption in tasks such as storing and sharing information, is generally described by means of an entropy variation [137]. Specifically, for equilibrium thermal states the thermodynamic entropy coincides with the information theory entropy, or Shannon entropy [138]. In a classical context, entropy defines the uncertainty of predicting the result after an operation, and so, loosing information implies an increase of entropy [139]. This is known as Landauer's erasure principle. The most famous example of an application of this principle is the solution to the Maxwell's demon paradox [49, 139, 140]. In its original proposal, this demon is an intelligent agent that has information about velocity and position of gas particles in a box, and therefore is able to selectively transfer hotter particles from a cold to a hot partition of the box, in apparent violation of the second law of thermodynamics. Significantly, the solution of this paradox requires to incorporate information explicitly in the thermodynamic description of the process.

The development of new technologies at the nano-scale has made accessible the investigation of the connection between quantum information theory and thermodynamics. Fundamental issues concern the thermodynamic cost [141] and thermodynamic nature [142] of quantum projective measurements. Projective measurements add stochasticity to a process in a purely quantum way, and make the dynamics irreversible, although micro-reversibility is still valid. This is similar to what happens in the irreversible case of heat exchange with a thermal bath, where micro-reversibility is not violated [143]. Moreover, quantum projective measurements can be used as an input to implement feedback processes in the system dynamics [144, 145]. The implementation of feedback mechanisms is a way to realize non unital maps where not only reversibility but also micro-reversibility are broken – the reverse process of a non-unital map is not well defined [45].

The irreversibility of a physical process can be measured via the relative entropy or fluctuation relations [146, 147]. The experimental characterization of irreversibility has been achieved for closed and open classic systems [148–153], and for closed quantum systems [154]. So far, the characterization of irreversibility in open quantum systems was not achieved, and will be addressed in this thesis by the exploration of quantum fluctuaction relations with an NV center spin in diamond.

3.2 Classical fluctuation relations

Fluctuation theorems or fluctuation relations (FR) refer to the set of equations that involve the statistical analysis over a canonical ensemble of trajectories, in order to relate equilibrium and out-of-equilibrium variables. Accounting for the statistical fluctuations is the key to reformulate the second law of thermodynamics, usually expressed as inequalities, in terms of equalities. As a major example, in 1997 [129] Christopher Jarzynski proposed a relation between the averaged negative exponentiated work (W) done on a system, averaged over a statistically relevant ensemble of realizations of the system dynamics, and the change in the free energy between two equilibrium thermal states

$$\langle e^{-\beta W} \rangle = e^{-\beta \Delta F} \tag{3.1}$$

In literature, this relation is referred to as work fluctuation relation (WFR) [129] or Jarzynski equality. Notably, equation (3.1) directly implies the second law of thermodynamics, by using the Jensen's inequality: $\langle W\rangle \leq \Delta F$. A couple of years later, another way to postulate the WFR was proposed [130], the so called Crook's relation

$$e^{-\beta(W-\Delta F)} = \frac{\widetilde{P}(-W)}{P(W)} \tag{3.2}$$

where $P(W)$ is the probability of applying work W on the system during the (*forward*) protocol, and $\widetilde{P}(-W)$ is the probability of applying work $-W$ on the system for a *backwards* protocol. Note that Eq. (3.2) directly implies Eq. (3.1) (multiply by $P(W)$ and integrate over W), it is for this reason that some authors refer to Eq. (3.2) as the WFR. This framework has been also extended to describe the flow of heat Q and matter transport (number of particles N) between different systems with different (inverse) temperatures β_i and chemical potentials μ_i, known as exchange fluctuation relation (XFR) [155, 156]

$$\langle e^{-\sum_i \beta_i Q_i + \mu_i N_i}\rangle = 1. \tag{3.3}$$

A special case of the XFR, and one of particular interest for this thesis, corresponds to a (small) system (S) in contact with a thermal reservoir (R). In such case the super-system formed by the sum of S and R is a closed system, which implies that $Q_\mathrm{S} = -Q_\mathrm{R}$. Therefore, the XFR for a system that thermalizes with a reservoir is expressed as

$$\langle e^{-(\beta_S - \beta_R)Q_S}\rangle = 1. \tag{3.4}$$

A general FR can be written as

$$\langle e^{-\beta_S \Delta E}\rangle = \gamma, \tag{3.5}$$

as demonstrated by Sagawa-Ueda for a system under a feedback process [157], where γ represents de efficacy of the feedback protocol. Hence Eq. (3.5) is known as Jarzynski-Sagawa-Ueda (JSU) relation. Remarkably, all these relations hold for processes that drive the system arbitrarily far from equilibrium, provided that the initial state is in thermodynamic equilibrium.

These fluctuation relations can be recast in quantum mechanical settings. For example, the Jarzynski equality for a quantum system, the quantum Jarzynski equality [131–133] and the Crook's relation for a quantum system, the Tasaki-Crooks relation [131] were both proposed in the year 2000. The quantum version of the XFR was published in the same paper as its classical counterpart [155]. A more recent example is the FR for heat engines, proposed for a classical system in 2011 [158] and for a quantum setting in 2014 [159]. Recasting FRs into their quantum mechanical from is by no means a simple task, mainly because the definition of thermodynamic variables for quantum systems is far from trivial.

This chapter contains some of the basic concepts of quantum thermodynamics that are necessary to understand how to understand and how to measure fluctuation relations using an open quantum system. For a complete and formal discussion on the subject, please refer to Ref. [38].

3.3 Quantum fluctuation relations: basic concepts

In this section I will briefly introduce some of the concepts and tools necessary to understand the next chapters of this thesis. For a broad-audience introduction on this topic, I also refer to Ref [136].

In quantum settings, the description of thermodynamics processes is challenged under different fundamental aspects. Remarkably, temperature is not always a well defined physical quantity in quantum settings. The state of a quantum system in thermal equilibrium with a heat bath corresponds to a Gibbs state, or thermal state

$$\begin{aligned} \rho_{\text{th}} &\equiv e^{-\beta\mathcal{H}}/Z_\beta \qquad (3.6) \\ &= \sum_i |E_i\rangle\langle E_i|\, e^{-\beta E_i}/Z_\beta \qquad (3.7) \end{aligned}$$

where the second line is the spectral decomposition of the Gibbs state in terms of the eigenvalues E_i and eigenstates $|E_i\rangle$ of a finite quantum system Hamiltonian $\mathcal{H}$, β is the inverse temperature of the heat bath, and

$$Z_\beta \equiv \text{Tr}[e^{-\beta\mathcal{H}}] = \sum_i e^{-\beta E_i} \qquad (3.8)$$

is the partition function. These kind of thermal states represent a small subset of all the possible mixed states allowed in a quantum system. The particular case of a two-level system is interesting because every incoherent mixed state (where all the coherences, i.e., the off-diagonal terms of the density matrix, $|E_i\rangle\langle E_j|$ for $i \neq j$, are null) can be recast as a pseudo-thermal state, where the pseudo- prefix refers to the fact that these mixed states are not necessarily in thermal equilibrium. These kind of states are most often employed in the experimental study of quantum FRs, as will be mentioned in Sec. 3.4, and throughout Chapter 4. The analogy of pseudo-thermal states breaks for systems with dimension larger than two, as will be the case of the study presented in Chapter 5.

The free energy of a quantum system F_β is defined in an analogous way to its classical counterpart

$$F_\beta \equiv -\beta^{-1} \ln Z_\beta. \qquad (3.9)$$

As a second fundamental aspect, the definition of quantum non-equilibrium quantites, i.e., quantum work, quantum heat, and quantum entropy is not so straightforward in quantum settings. The amount of work (or heat flux, or entropy) depends on the trajectory followed by the system, which implies that, in general, it cannot be associated with a quantum observable [160]. To date different proposals have been formulated to define these concepts for a general quantum system [136]. In the context of FRs, heat flux an work can be estimated through the so-called two-point measurement (TPM) scheme [161], that I will illustrate in depth in Sec. 3.3.1, that measures the energy variation of the system between the initial and final states, for each trajectory (single realizations of a protocol). Attributing this energy variation to work or heat flux depends on the nature of the process occurred. For example, the energy variation of an isolated system (which can be composed of interacting subsystems) caused by an external driving, i.e., a time-varying Hamiltonian, is associated with work [38, 131–133]. If the driven system is weakly coupled to a thermal reservoir, then the energy variation of the reservoir is equal to the flow of heat [42, 59].[1]

---

[1] Notice that this implies that evaluating work and heat flux requires information on both the system and on the reservoir, that is often not practically available.

However, not all the quantum processes fit within these categories. This is the case of a quantum system in contact with a non-thermal reservoir, as is common in experimental studies of FRs, which will be mentioned in Sec. 3.4. Another notable example is the case of quantum projective measruements (QPMs) applied to the quantum system during its evolution. Remarkably, FRs are expected to hold for a quantum system in the presence of QPMs [38, 162–165]. However, due to the lack of a classical analogy, the evergy variation caused by QPMs has been attributed either to "non-equilibrium work" [166] or to "quantum heat" flux [142].

The research presented in the following chapters refers to the study of energy variation of a quantum system in the presence of stochastically distributed interactions, that are modeled as QPMs followed by conditioned dissipation caused by the contact with a non-thermal reservoir. During the time intervals between two subsequent interactions, the quantum system is coherently driven by a time-independent Hamiltonian, therefore no external work is applied on the system. For the sake of clarity, we refer to the FRs associated with this process as energy exchange fluctuation relations.

3.3.1 Measuring energy exchange fluctuation relations

The verification of FRs for quantum systems is possible through a two point measurement (TPM) scheme [160, 161] consisting in the measurement of the expectation value of the Hamiltonian for the initial and for the final state of the system. Since the practically accessible quantity is the system energy variation, then the energy exchange fluctuation relation is conveniently expressed in terms of the characteristic function of the energy variation statistics

$$G(\varepsilon) \equiv \langle e^{-\varepsilon \Delta E} \rangle, \tag{3.10}$$

where ε is an energy scale factor that depends on the specific type of protocol. For example, for an isolated system, the quantum Jarzynski equality is written as $G(\beta) = e^{-\beta \Delta F}$, where β is the inverse temperature of the initial thermal state [51–56]. In the case of a system (S) in contact with a (pseudo-)thermal reservoir (R), then the quantum exchange fluctuation relation (XFR) is written as $G(\Delta\beta) = 1$ (compare with Eq. (3.4)), where $\Delta\beta \equiv \beta_{\mathrm{S}} - \beta_{\mathrm{R}}$ is the difference between the initial inverse (pseudo-)temperatures [19, 57, 167].

In practice, $G(\varepsilon)$ is obtained by measuring the energy variation with a TPM scheme. The energy measurements performed at the beginning and at the end of the protocol give access to the full statistics of ΔE, i.e.,

$$P_{\Delta E} \equiv \mathrm{Prob}(\Delta E) = \sum_{i,j} \delta(\Delta E - \Delta E_{j,i}) P_{j,i} \tag{3.11}$$

where $\Delta E_{j,i} \equiv E_j - E_i$ and $P_{j,i}$ is the joint probability to measure E_i in the first energy measurement and E_j in the final energy measurement.

Once obtained the energy variation distribution $P_{\Delta E}$, the average value of any function $f(\Delta E)$ of ΔE is expressed in terms of the probability distribution of ΔE:

$$\begin{aligned} \langle f(\Delta E) \rangle &= \int_{-\infty}^{\infty} \mathrm{d}(\Delta E) f(\Delta E) P_{\Delta E} \\ &= \sum_{i,j} f(\Delta E_{j,i}) P_{j,i} \,. \end{aligned} \tag{3.12}$$

In particular, one can reconstruct the characteristic function of the energy variation

$$G(\varepsilon) = \sum_{i,j} e^{-\varepsilon \Delta E_{j,i}} P_{j,i} \,. \tag{3.13}$$

3.4 Experimental tests of quantum fluctuation relations

This section contains a short overview of the different platforms used to test QFRs. As already mentioned, the very first use of NV center for the study of quantum FRs was done by our group, which is the content of this Part of the thesis and which has been published in Refs. [19, 58]. Note that there exist only one more article, Ref. [18], where NV centers are used as experimental platform in the field of quantum thermodynamics. In the latter, an ensemble of NV centers at room temperature are used to emulate the operation of a quantum heat engine, and, remarkably, measure a pure quantum signature in the operation of the engine itself.

In addition to NV centers [19, 58], the other experimental platforms that have been used for the study of quantum fluctuation relations are single ions [51–53], superconducting qubits [54], ensemble of cold atoms/atom chip [55], and NMR setup (molecules suspended in liquid) [56, 57].

The first experimental verification of the quantum work fluctuation relation, or Jarzynski equality, in a closed system was performed in 2014 [56]. Using a set of non-interacting chloroform molecules, and particularly using the ^{13}C nuclear spin ($S = 1/2$) as a qubit, and the ^{1}H nuclear spin as an ancillary system, the authors of Ref. [56] measured the work characteristic function $G_W(\beta)$, where β is the inverse pseudo-temperature of the initial state (no thermal reservoir was involved in the preparation of the initial state). The energy variation in this closed system was realized by driving it with a time-varying Hamiltonian. Very recently, in a similar experiment using a different molecule and the nuclear spins of three ^{19}F isotopes (two of them as qubit systems, and the third one as an ancillary qubit), a different research group studied the (pseudo-)heat exchange between two spins [57], and they found out that only under specific conditions, this interaction was actually compatible with the Jarzynski-Wójcik [155] heat exchange fluctuation relation. It is worth noting that the interaction between these two qubits is described by a unitary evolution operator, hence there are no irreversible process in the dynamics (as it is for the case presented in this thesis). Note that liquid-state nuclear magnetic resonance platforms do not support measurements of single quantum trajectories, and the result of the performed measurements constitutes the spatial average over several (10^{15} [57]) non-interacting molecules.

A second experimental verification of the quantum Jarzynski equality was performed in 2015 [51], using a single trapped ion. In this experiment the system is a harmonic oscillator formed by the ion-trap apparatus. In contrast with the spin based experiments, this infinite dimensional system is initially prepared in a thermal state, which temperature is measured from average phonon number. The energy of the closed system was measured before and after a unitary evolution associated with a time-varying Hamiltonian. The same experimental setup was used to measure the work fluctuation relation in the presence of decoherence [52]. This means that the system is open, but only weakly coupled to a decoherent environment. Reference [52] represents the first experimental study of an *open quantum system* in the context of FRs without effective heat flux. In contrast with the previous experiment [51], in

Ref. [52] the system was a qubit formed by two hyperfine levels in the ion ground-state manifold of $^2S_{1/2}$. The initial effective thermal state (pseudo-thermal state) was prepared by combining optical pumping and on-resonant microwave driving, which is equivalent to the techniques used in the spin-based platforms (NV centers and liquid-state NMR setups) to create pseudo-thermal states.

Later, a quantum work meter was realized by using a Bose-Einstein condensate trapped by an atom chip [55]. The spin-based system is formed by two hyperfine sublevels of ^{87}Rb atoms. In this experiment, the spin (internal) degree of freedom is entangled with the motional (external) degree of freedom of the atoms, therefore, performing imaging measurements of the cloud of atoms corresponds effectively to a measurement on the internal degree of freedom of the atoms themselves.

In Ref. [54] a superconducting qubit was used to measure the work fluctuations during the so called shortcut-to-adiabaticity protocols. More recently a different kind of superconducting qubit was used to measure the work and the heat flux for single trajectories of the system [168]. Although the measurement of FRs is not explicitly mentioned in these last two references, they set the bases to permit this kind of studies in the future, specially for FRs involving work and heat at the same time.

To conclude this chapter, I want to mention that the same kind of platforms have been employed also to realize practical implementations of quantum thermal machines, that exploit the same kind of processes (entailing work application and heat flux) that are described by QFRs. These implementations include molecules suspended in liquid in NMR experiments [169, 170], single ions [48, 171], ensemble of NV centers [18], and single photons [172].

Chapter 4

Experimental test of exchange fluctuation relations in an open two-level quantum system

Opening an energy exchange channel from a quantum system to a reservoir poses challenges for describing the non-equilibrium thermodynamic processes that take place [38]. While a dephasing dynamics can be effectively traced back to the case of an isolated system [52], the energy transport between a system and its environment is expected to be described by an exchange fluctuation relation [37, 38, 42]. Such relation was originally introduced to describe the heat exchange between two bodies in thermal contact [155], each initially in thermal equilibrium. In the case of a system in contact with a reservoir, the system evolves under thermalizing dynamics, reaching a final thermal state. Also in the absence of a thermal bath, provided that the system undergoes a thermalizing dynamics, the exchange fluctuation relation can be written in terms of the initial and asymptotic thermal states of the system [167]. What happens if the system follows instead a quantum dissipative non-thermalizing dynamics?

In this chapter, I present an experimental test of the energy exchange fluctuation relation in a two level quantum system subject to repeated quantum projective measurements (QPMs) and energy dissipation, where the resulting dissipative dynamics drives the system towards an out-of-equilibrium energy steady state, hence emulating the contact with a pseudo-thermal reservoir. The open two level system is formed by a single NV center qubit in diamond at room temperature, in the presence of trains of short laser pulses. Each absorbed laser pulse results in a QPM [71], and in an energy redistribution that can be modeled as a controlled energy exchange with a Markovian reservoir [18]. The time intervals between QPMs follow a stochastic distribution due to the finite absorption probability. Tuning the laser duration and power enables the control of the coupling strength between the quantum system and the reservoir.

The combined effect of QPMs and dissipation can create or destroy quantum coherence during the system dynamics, an effect that goes beyond the classical description. This work, reported in Ref. [19], represents the first verification of the exchange fluctuation relation for an open two-level quantum system in the presence of QPMs and dissipation (irreversible dynamics). This result is achieved by measuring the statistics of the exponentiated energy fluctuations through a two-point measurement (TPM) protocol. Since the dissipative map is correctly described by pseudo-thermalizing dynamics [167], we find that the exchange fluctuation relation is written in terms of the initial and asymptotic pseudo-temperatures.

In Sec. 4.1 I introduce the protocol used to measure the statistics of the energy variation. Sec. 4.2 presents the experimental data and the discussion on how to construct the full statistics of the energy variation, which is necessary to reconstruct the characteristic function of the energy variation and to verify the energy exchange fluctuation relation. Section 4.3 contains the complete formalism to describe the dissipative dynamics, both with a numerical and an analytic model. The conclusions of this project are given in Sec. 4.4.

4.1 Protocol implementation

This section introduces the protocol that we devised to measure energy fluctuations in a two level system formed by the two electronic spin projections within the ground state of an NV center in diamond.

A continuous nearly-resonant microwave field sets the Hamiltonian $\mathcal{H}$ of the two-level system in the frame rotating at the microwave frequency [Eq. (1.5)]

$$\mathcal{H} = \frac{\hbar\omega}{2}(\cos\alpha\ \sigma_z - \sin\alpha\ \sigma_x), \tag{4.1}$$

with eigenstates $\{|\uparrow\rangle, |\downarrow\rangle\} = \{\cos\frac{\alpha}{2}|0\rangle - \sin\frac{\alpha}{2}|+1\rangle, \sin\frac{\alpha}{2}|0\rangle + \cos\frac{\alpha}{2}|+1\rangle\}$, and eigenvalues $E_\uparrow = \hbar\omega/2$ and $E_\downarrow = -\hbar\omega/2$. Here, σ_i are Pauli matrices, $\tan\alpha = -\Omega/\delta$ and $\omega = \sqrt{\delta^2+\Omega^2}$, $\Omega = 1.3$ MHz being the bare Rabi frequency, and $\delta \in [0, \Omega]$ the microwave detuning. This Hamiltonian (4.1) remains constant during the protocol. Repeated short laser pulses induce a non-unitary dynamics, as explained below.

In contrast to the work described in Chapter 2, here we consider an NV center with no detectable coupling to nearby impurities (^{13}C). In addition, we used an external magnetic field of 394(1) G, which is close enough to the ESLAC to ensure that the ^{14}N nuclear spin is polarized after a long laser pulse [Sec. 1.5]. The long coherence time of the nuclear spin implies that it remains polarized during a whole protocol. Moreover, on the experiment timescales ($\sim \mu$s) spin-lattice relaxation is negligible (T_1 ∼ms), while the Rabi driving together with the short laser pulses prevent spin dephasing to occur.

4.1.1 Adapted TPM scheme

As described in Sec. 3.3.1, the energy exchange fluctuation relation is conveniently expressed in terms of the characteristic function $G(\varepsilon)$ [Eq. (3.13)], that can be reconstructed by measuring the full statistics of the energy variation [Eq. (3.11)],

$$P_{\Delta E} \equiv \text{Prob}(\Delta E) = \sum_{i,j} \delta(\Delta E - \Delta E_{j,i}) P_{j,i} \tag{4.2}$$

where $\Delta E_{j,i} \equiv E_j - E_i$ and $P_{j,i}$ is the joint probability to measure E_i in the first energy measurement and E_j in the final energy measurement. Notice that $P_{j,i}$ can be factorized as $P_{j,i} = P_{j|i}P_i$ where $P_{j|i}$ is the conditional probability for energy variation and P_i is the probability associated with the first energy measurement. In contrast with the usual TPM scheme, where an energy projective measurement is performed on the initial thermal state, we propose an alternative scheme in which we measure the energy variation conditional probabilities, and we combine the results

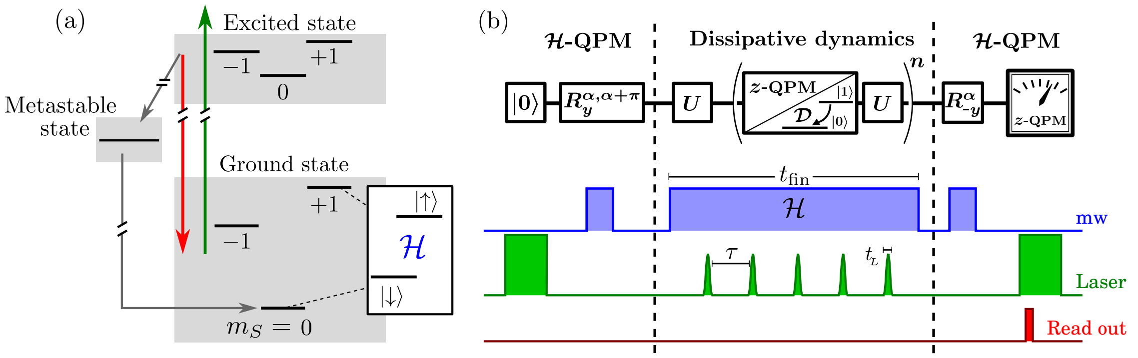

Figure 4.1: **(a)** Schematic representation of the photodynamics of a nitrogen-vacancy center. Photon absorption (green upwards arrow) and spin preserving spontaneous emission (red downwards arrow) between the electronic ground and excited levels realize quantum projective measurements of the spin state along the z axis (z–QPM). A non-radiative decay channel (left gray arrows) enables controlled optical spin pumping to the $|0\rangle$ state. Inset: Effective two-level system considered in the protocol, formed by two dressed spin states set by quasi-resonant continuous driving (see Eq. (4.1)). **(b)** Block-diagram of the two-point measurement protocol implementation, and experimental pulse sequence. After initialization in the $|0\rangle$ state, for each protocol repetition a Hamiltonian eigenstate $|\uparrow\rangle$ ($|\downarrow\rangle$) is prepared by applying a microwave (mw) gate R_y^{α} ($R_y^{\alpha+\pi}$). During the time t_{fin}, the mw-driven spin unitary evolution set by the Hamiltonian $\mathcal{H}$, defined in Eq. (4.1), is perturbed by equidistant short laser pulses acting as z–QPMs plus dissipation ($\mathcal{D}$). The inter-pulse time ($270 \leq \tau \leq 750$ ns) is much longer than each pulse duration ($t_{\mathrm{L}} = 41$ ns). At the end, a quantum projective measurement of the final state energy ($\mathcal{H}$–QPM) is realized with a mw gate R_{-y}^{α} and a spin selective fluorescence intensity measurement – read out. Adapted from [19].

multiplying them by the probabilities P_i, to be seen as weight factors. Under the assumption of performing a large number of experimental realizations (as it is the case for the experiments presented here), the two protocols give equivalent results on average. Notice that the method proposed here has the advantage of overcoming the difficulties to prepare an initial thermal state. Moreover, it removes the possible experimental errors associated with the first energy measurement, and allows to use one single set of measurements to study different initial states.

4.1.2 Energy jump probabilities

Measuring the conditional probability of the energy variation $P_{j|i}$, is achieved by initializing the system into each of the energy eigenstates, and measuring the energy of the system at the end of the protocol.

Each of the two energy eigenstates is prepared by optically initializing the system into $|0\rangle$, and then applying a rotation gate along σ_y with an angle α. In other words, the Hamiltonian eigenstates are prepared as $|\uparrow\rangle = R_y^{\alpha}|0\rangle$ and $|\uparrow\rangle = R_y^{\alpha+\pi}|0\rangle$, where the rotation $R_y^{a} \equiv U^{-ia\sigma_y}$ is induced by a microwave (mw) gate, as depicted in Fig. 4.1(b). To implement the final energy measurement ($\mathcal{H}$–QPM), we apply another mw gate that maps $\mathcal{H}$ into σ_z, i.e., R_{-y}^{α} (as detailed in Fig. 4.1(b) and (c).IV), and then measure the σ_z operator (usual photoluminescence (PL) intensity measurement described in Chapter 1). Low collection efficiency and photon shot noise impose the need of repeating the procedure several times ($\sim 1.6 \times 10^6$) and averaging over the detected PL intensity to reduce the readout uncertainty.

Therefore, we measure the conditional probabilities $P_{\uparrow|\uparrow}$ and $P_{\uparrow|\downarrow}$ for the spin to have energy $E_{\text{fin}} = E_\uparrow$, when starting respectively from the states $\varrho_\uparrow$ or $\varrho_\downarrow$. Notice that by definition $P_{\uparrow|i} + P_{\downarrow|i} = 1$, for $i =\uparrow$ and $\downarrow$. Hence, measuring the two probabilities $P_{\uparrow|\uparrow}$ and $P_{\uparrow|\downarrow}$, are enough to reconstruct the complete energy variation distribution.

Pseudo-thermal states

As mentioned in Sec. 3.3, for any two-level mixed state (without coherent terms) written as $\varrho^{\text{mix}} = P_\uparrow \varrho_\uparrow + (1 - P_\uparrow)\varrho_\downarrow$, an effective inverse temperature (pseudo-temperature) is defined as

$$\beta^{(\text{eff})}(P_\uparrow) = \frac{2}{\hbar\omega} \operatorname{arctanh}(1 - 2P_\uparrow) \tag{4.3}$$

$$= \frac{1}{\hbar\omega} \ln \frac{1 - P_\uparrow}{P_\uparrow}. \tag{4.4}$$

In the experiment, the initial inverse pseudo-temperature $\beta_{\text{in}}^{(\text{eff})}$ is defined by the choice of the initial probabilities P_i.

4.1.3 Dissipative map: effective 2-level system

The two level system is continuously driven by the Hamiltonian (4.1). In addition, the NV center is subject to trains of short laser pulses with duration t_{L} at intervals τ, as depicted in Fig. 4.1(b). Due to the finite photon-absorption probability, a train of equidistant laser pulses entails a stochastic time distribution of laser absorption, for each single realization of the experiment. The photodynamics of the NV center is well described with a seven-level model (as explained in Sec. 1.4). However, the experiments in this chapter can be well-reproduced by an effective two-level model. As described in Sec. 1.1, the absorption of 532 nm laser pulses excites the NV-center electronic spin from the ground to the excited triplet states. The decay involves (i) radiative transitions to the ground state, and (ii) non-radiative transitions through the singlet metastable state. In a reduced two-level system, the interaction with short laser pulses has a probability $(1 - p_{\text{diss}})$ to result in an ideal quantum projective measurement of σ_z (z–QPM) [71], but also a finite probability ($p_{\text{diss}} < 1$) to destroy all previous information and force the resulting state to be $|0\rangle$. This irreversible optical pumping is equivalent to a controlled dissipation channel towards $|0\rangle$ in the reduced two-level system. Note that the effective optical pumping rate depends on the number of excitation-decay cycles performed by the system, which can be controlled by changing the laser pulse duration and power. For a single cycle, $p_{\text{diss}} = \Gamma_{1m}/(\Gamma_{1m} + \Gamma_{eg}) \simeq 0.44$ (see Tab.1.1). Therefore, even when we cannot completely isolate the dissipation from the z–QPMs, the strength of the dissipation can be tuned in the interval $p_{\text{diss}} \in [0.44, 1]$.

A detailed description of the effective two level model, and its comparison with the complete seven level model are presented in Sec. 4.3.

4.2 Experimental results

The main results of this work is the measurement of the characteristic function $G(\varepsilon)$ of the energy variation [Eq. (3.10)] of the spin qubit under the stochastic dissipative dynamics induced by the application of trains of short laser pulses, as described above. This allows us to verify the energy exchange fluctuation relation. The measurement of $G(\varepsilon)$ requires to reconstruct the full statistics of energy, which we obtained by measuring the conditional probabilities of the spin to jump in a state with fixed energy, once known its initial energy.

The measurements of the energy jump probabilities are presented in Sec. 4.2.1, with a discussion on the estimation of the asymptotic pseudo-temperature for a dissipative map. Section 4.2.2 contains the analysis of these results, used to obtain the full statistics of the energy variation. The experimental verification of the energy exchange fluctuation relation, via the reconstruction of the characteristic function of the energy variation, is shown in Sec. 4.2.3.

4.2.1 Conditional probabilities of energy jumps

The combined effect of continuous driving and a train of short laser pulses leads the system into an asymptotic out-of-equilibrium steady-state in the energy basis (SSE). Figure 4.2 shows the conditional probabilities $P_{\uparrow|\downarrow}$ and $P_{\uparrow|\uparrow}$ as a function of the evolution time t_{fin}, obtained in the experiment. In the absence of laser pulses, the spin qubit is a closed system and the energy eigenstates do not evolve in time (usually referred to as *spin lock*). As a consequence of the laser pulses, the system jumps between states with different coherences in the energy basis and the final energy measurement returns, on average, a mixed state. Eventually, the system reaches a SSE defined by the balance between the energy variation due to z–QPMs applied to the system and the dissipation channel. The SSE is independent of the initial state. The photon absorption probability dictates how fast the system approaches the asymptotic steady state.

To quantitatively support that the considered two-level model provides an accurate description of the system dynamics, we performed a numerical Monte Carlo simulation of the dynamics [Sec. 4.3.1] and we found excellent agreement with data (see Figure 4.2). Note that the only fit parameter is the absorption probability, which depends on the laser power and characterizes the stochasticity of the protocol.

In a TPM protocol the fixed point of the map is the pseudo-thermal state $\varrho^{\text{th}} = P_{\uparrow}^{\text{th}}\varrho_{\uparrow} + (1 - P_{\uparrow}^{\text{th}})\varrho_{\downarrow}$ such that the mean energy is kept constant at any given time t_{fin}, i.e., $\langle \Delta E \rangle = 0$. From Eq. (3.12), this condition can be rewritten in terms of energy jump probabilities as

$$\frac{1 - P_{\uparrow|\downarrow}}{P_{\uparrow|\uparrow}} = \frac{1 - P_{\uparrow}^{\text{th}}}{P_{\uparrow}^{\text{th}}} \equiv e^{\beta_{\text{fp}}^{(\text{eff})}\hbar\omega} \tag{4.5}$$

where $\beta_{\text{fp}}^{(\text{eff})}$ is the inverse pseudo temperature [Eq. (4.4)] of the fixed point. Therefore, from the data (and/or simulation) shown in Fig. 4.2 we can estimate $\beta_{\text{fp}}^{(\text{eff})}$. Notice that Eq. (4.5) must be fulfilled at any time t_{fin}. In particular, it is valid for the asymptotic SSE, where the probability to find the spin in the $|\uparrow\rangle$ state is independent of the initial state: $P_{\uparrow}^{\infty} = P_{\uparrow|\uparrow}^{\infty} = P_{\uparrow|\downarrow}^{\infty}$. This implies that the inverse temperature of the SSE is $\beta_{\infty}^{(\text{eff})} = \beta_{\text{fp}}^{(\text{eff})}$, i.e., the asymptotic state is equal to the fixed point of the map.

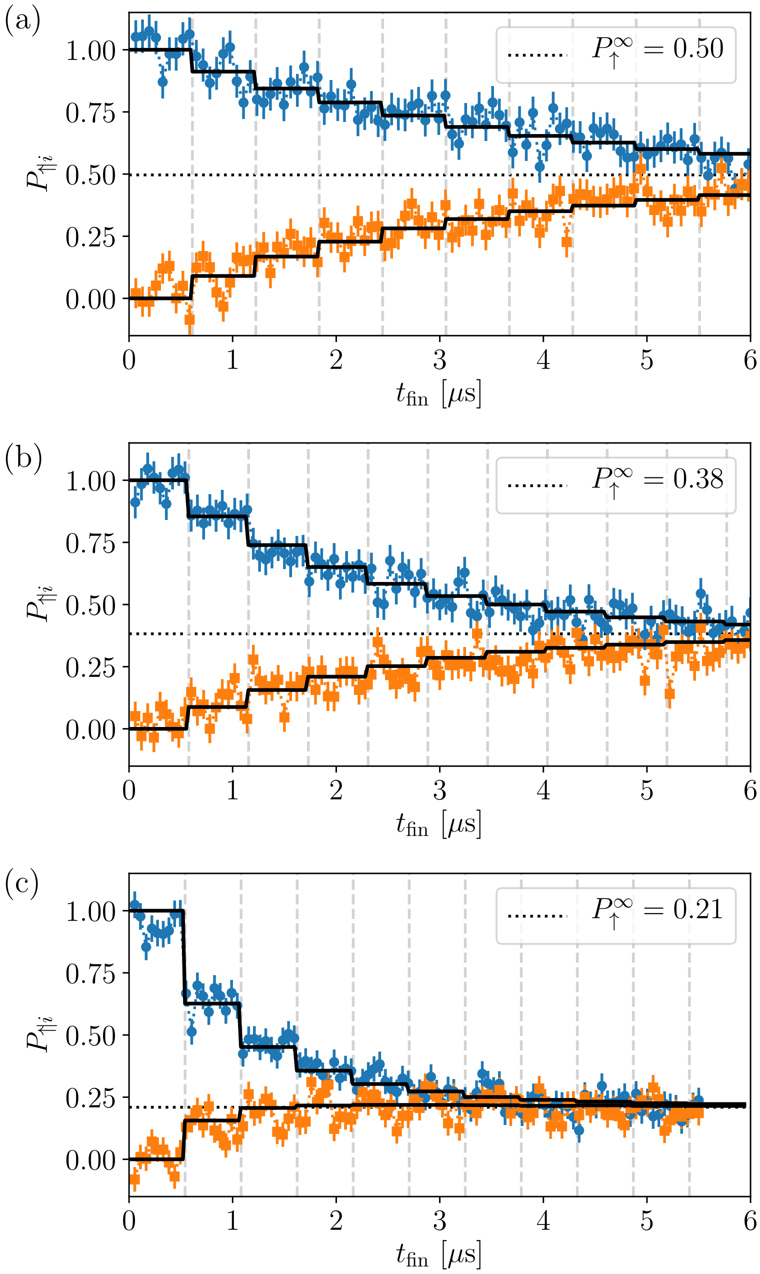

Figure 4.2: Conditional probabilities $P_{\uparrow|\uparrow}$ and $P_{\uparrow|\downarrow}$ to measure $E_f = E_\uparrow$ as a function of the evolution time t_{fin} starting from the Hamiltonian eigenstates $|\uparrow\rangle$ (blue circles) or $|\downarrow\rangle$ (orange squares). Error bars denote the experimental uncertainty given by the photon shot noise. The solid black lines are obtained with the numerical simulation of the two level system dynamics (Sec. 4.3.1), with an effective absorption probability p_{abs}. The horizontal dotted lines represent the conditional probabilities for the asymptotic (out-of-equilibrium) steady states (see text). **(a)** $\alpha = \pi/2$, $\tau = 5\pi/3\omega$ and $p_{\mathrm{abs}} = 0.18(1)$. **(b)** $\alpha = \pi/3$, $\tau = 5\pi/3\omega$ and $p_{\mathrm{abs}} = 0.27(1)$. **(c)** $\alpha = \pi/4$, $\tau = 2\pi/\omega$ and $p_{\mathrm{abs}} = 0.68(1)$.

In the case of $\alpha = \pi/2$ (see Fig. 4.2(a)), z–QPMs and dissipation act in a direction orthogonal to the Hamiltonian [Eq. (4.1)], and they bring the system into an SSE with $P_{\uparrow}^{\infty} = 1/2$ ($\beta_{\infty}^{(\mathrm{eff})} = 0$). Indeed for $\alpha = \pi/2$ the asymptotic state before the final energy measurement is a fully coherent state in the Hamiltonian basis such that $\langle \mathcal{H} \rangle = 0$, thus the density matrix after the final energy measurement corresponds, in average, to a completely mixed state (that is, a thermal state with infinite pseudo-temperature). The same asymptotic probability $P_{\uparrow}^{\infty} = 1/2$ would be observed in an experiment without dissipation, i.e., with a series of QPMs [142, 173]. Therefore, in this configuration ($\alpha = \pi/2$) during a TPM protocol, the dissipative map is indistinguishable from unitary dynamics plus repeated measurements [174].

For $\alpha = \pi/3$, and $\alpha = \pi/4$ (see Fig. 4.2(b-c)), the asymptotic state probability to measure $E_{\uparrow}$ was estimated to be $P_{\uparrow}^{\infty} \simeq 0.382$ and $P_{\uparrow}^{\infty} =\simeq 0.209$, respectively. Taking into account the value of $\omega = \Omega/\sin\alpha$, and the definition of inverse pseudo temperature [Eq. (4.4)], the estimated pseudo temperature of these two asymptotic states results in $T_{\infty}^{(\mathrm{eff})} = 515(2)\ \mu\mathrm{K}$ ($\alpha = \pi/3$, $\tau = 5\pi/3\omega$), and $T_{\infty}^{(\mathrm{eff})} = 66.7(4)\ \mu\mathrm{K}$ ($\alpha = \pi/4$, $\tau = 2\pi/\omega$).

4.2.2 Statistics of the energy variation

The energy variation occurred to the qubit after the TPM protocol can assume one of the three values $\Delta E \in \{-\hbar\omega, 0, +\hbar\omega\}$. Figure 4.3 shows the distribution of energy variation ($P_{\Delta E=0} = P_{\uparrow,\uparrow} + P_{\downarrow,\downarrow}$, $P_{\Delta E=+\hbar\omega} = P_{\uparrow,\downarrow}$, and $P_{\Delta E=-\hbar\omega} = P_{\downarrow,\uparrow}$) for a fixed initial pseudo-thermal state when varying the value of α and the power of the laser pulses. Notice that, as explained in Sec. 4.1.1, each of these energy variation joint probabilities corresponds to $P_{j,i} = P_{j|i}P_i$, where $P_{j|i}$ is the measured conditional probability, and $P_i = \exp(-\beta_{\mathrm{in}}^{(\mathrm{eff})}E_i)/Z$ is a weight factor that represents a (virtual) initial pseudo-thermal state ($Z = \sum_i \exp(-\beta_{\mathrm{in}}^{(\mathrm{eff})}E_i)$).

In contrast to Fig. 4.2, in Fig. 4.3 we have averaged all the measured data between N_{L} and $N_{\mathrm{L}} + 1$. This is valid because the system is considered to be closed during the time interval between consecutive laser pulses, meaning that its energy is not changed. Each dataset in Fig. 4.3 shows that the competing effects of z–QPMs and dissipation lead to a non-trivial dynamics, that modifies the energy distribution of the quantum system in different ways depending on the Hamiltonian angle α [Eq. (4.1)] and the absorption probability p_{abs}. The energy distribution also changes in terms of the time between laser pulses τ, the details on this subject are presented in Sec. 4.3.4 using an analytic two-level model of the dynamics.

4.2.3 Characteristic function of energy variation

Having measured the energy distribution probability, we can use Eq. (3.13) to gain access to the characteristic function $G(\varepsilon) \equiv \langle e^{-\varepsilon\Delta E} \rangle$ which is used to measure the XFR.

For two macroscopic systems S_1 and S_2 placed in thermal contact for a finite lapse of time, the statistics of exchanged heat Q is well known to be described by the heat exchange fluctuation relation $\langle e^{-(\beta_{\mathrm{in},S_1} - \beta_{\mathrm{in},S_2})Q} \rangle = 1$, where β_{in,S_1} and β_{in,S_2} are the initial inverse temperatures of S_1 and S_2 and $Q = \Delta E_{S_1} = -\Delta E_{S_2}$ [155]. Even in the absence of a physical reservoir, provided that the system undergoes a thermalizing dynamics, the non trivial value of ε for which $G(\varepsilon) = 1$, is $\varepsilon = \Delta\beta \equiv \beta_{\mathrm{in}} - \beta_{\infty}$, where β_{in} and β_{∞} are the initial and asymptotic inverse temperatures of the system [167]. These two results are equivalent in the case of a quantum

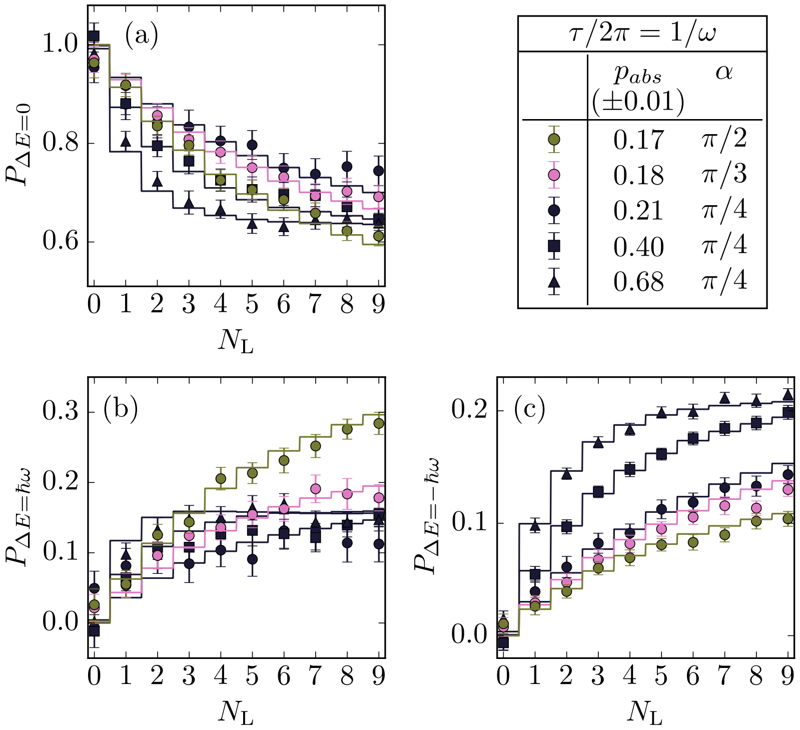

Figure 4.3: Statistics of the energy variation under different protocols: Probability to obtain $\Delta E = 0$, $+\hbar\omega$, $-\hbar\omega$, respectively, as a function of the number of laser pulses N_L experienced by the qubit, with initial probability $P_\uparrow = 1/(1+e)$. For each considered N_L value, the experimental points represent the average over ~ 10 different values of final evolution times t_{fin}. The error bars are due to the uncertainty on the measured photoluminescence intensity. The solid lines are the joint probabilities obtained from the numerical simulation of the system dynamics.

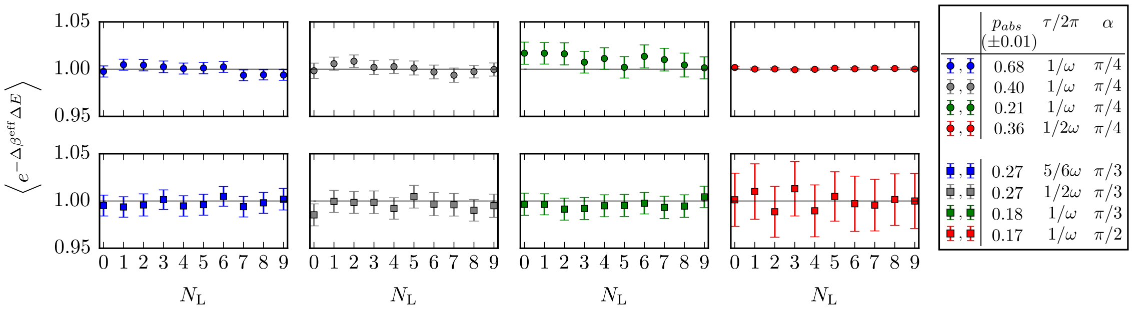

Figure 4.4: Experimental values of $\langle e^{-\Delta\beta^{(\mathrm{eff})}\Delta E} \rangle$ as a function of the number of laser pulses N_L. Each dataset represents a different combination between the parameters, the angle α (see Eq. (4.1)), the time τ between laser pulses, and the photon-absorption probability p_{abs}. The top-to-bottom order in the legend symbols corresponds to the left-to-right one in the plots. These data constitute the experimental verification of the exchange fluctuation relation for an open quantum system Eq. (4.6). The initial probability is set to $P_\uparrow = 1/(1+e)$, while the asymptotic probability $P_\uparrow^\infty$ is acquired from experimental data, as described in Sec. 4.2.1. Both quantities define the value of $\Delta\beta^{(\mathrm{eff})}$.

system interacting with a thermal reservoir at inverse temperature β_∞. The case of a dissipative non-thermalizing dynamics have not been explored before.

Here, the spin qubit interacts with a non-thermal reservoir and reaches an asymptotic non-equilibrium steady state defined by $\beta_\infty^{(\mathrm{eff})}$. Our findings are summarized in Fig. 4.4, which shows that the experimental data and simulation always verify the relation

$$\langle \exp\left(-\Delta\beta^{(\mathrm{eff})}\Delta E\right)\rangle = 1\,, \tag{4.6}$$

with

$$\Delta\beta^{(\mathrm{eff})} = \beta_{\mathrm{in}}^{(\mathrm{eff})} - \beta_\infty^{(\mathrm{eff})}, \tag{4.7}$$

irrespective of the initial state and the applied protocol, i.e., relative orientation between the z–QPM operator and the system Hamiltonian, inter-pulse time intervals and photo-absorption probability. Remarkably, we have found that equation (4.6) is valid for any value of N_{L}, not only when the system is in the SSE. This suggests that the induced dissipation truly emulates a thermalization process. Indeed, equation (4.6) corresponds to the XFR in the case of a two level system under (pseudo-)thermalizing dynamics (compare with Eq. (3.4)).

The previous sections of this chapter, up to this one, enclose all the experimental results for this chapter. In the next section 4.3 we will go into details on how to describe the system dynamics with a numerical or with an analytic model. The conclusions of the work are given instead in section 4.4.

4.3 Simulation for the effective two-level model

The interaction with a non-thermal reservoir calls for a deeper understanding of the role played by the energy scale factor ε. With this aim, we implemented numerical and analytic simulations to model the dissipative map introduced in section 4.1.3. Notice that the coherent driving, defined by the Hamiltonian in Eq. (4.1), affects only the $m_S = 0, +1$ states. Therefore a two level system exactly describes the dynamics during these parts of the protocol. It is the presence of short laser pulses that *opens* the two level system, hence imposing the need of a more complete description, either by including all the states involved in the process, or by using an effective two-level model description that incorporates z–QPMs and dissipation.

Before moving towards the effective two-level model description, we remind that the NV center electronic spin photodynamics is completely described by a seven level model [Sec. 1.4]. The parameters that determine this model, i.e., the decay rates, were extracted from measurements of the PL intensity as a function of the laser pulse duration (see Sec. 1.4.2). The seven level model can predict the dynamics of the NV in the presence of a continuous mw driving, or in the presence of laser pulses. By alternating these two descriptions we can effectively predict the NV dynamics for the complete pulse sequence shown in Fig. 4.1, including the preparation, dissipative dynamics and readout parts. As expected, the simulated dynamics present a very good agreement with experimental data, as shown in Fig. 4.6, where the only fitted parameter was the laser absorption probability $p_{\mathrm{abs}}^{(7)} = 0.45$ (called p_{abs} in Sec. 1.4, the superscript $^{(7)}$ is introduced here to distinguish between different models).

4.3.1 Numerical simulation of the qubit dynamics

In this section, we show that results consistent with the ones obtained for the seven level model can be obtained using a reduced two-level picture, composed only by

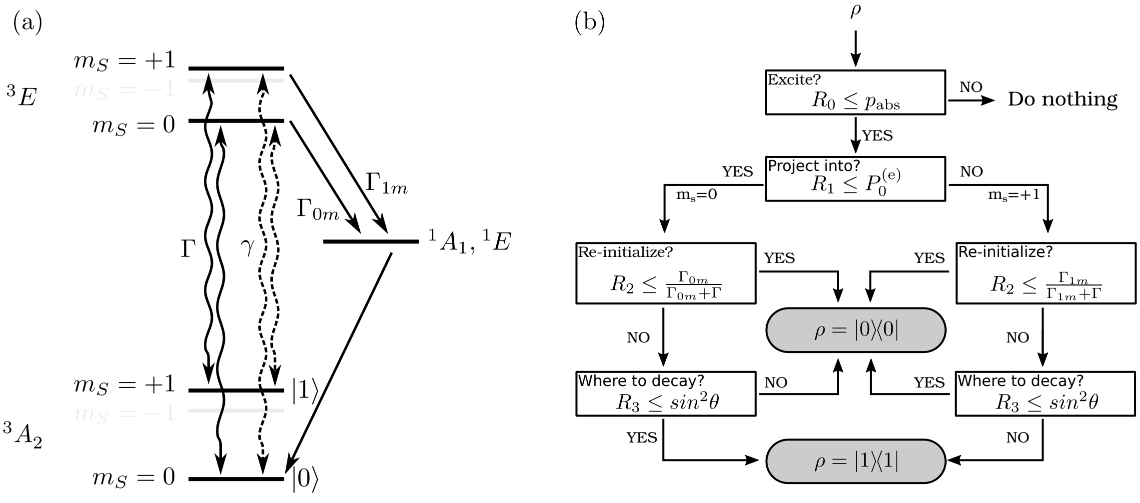

Figure 4.5: **(a)** Energy scheme of the NV center that gives origin to the reduced two-level system. The wavy lines represent radiative transitions, with dashed lines indicating the forbidden spin non-preserving transitions. The forbidden/non-forbidden ratio is given by $\tan^2\theta = \Gamma/\gamma$. **(b)** Flowchart of the reduced two-level system that incorporates all the dynamics of the complete seven level model. The four results (R_0,R_1,R_2, R_3) of an RNG are used to simulate the interaction of the qubit, in an initial state ρ, with a single short laser pulse. R_0 defines if the laser pulse is absorbed. R_1 defines the state after the z–QPM, where $P_0^{(\mathrm{e})}$ is the probability of the system to be in $m_S = 0$ after the laser excitation. R_2 defines if the system is initialized in $|0\rangle$ (dissipation). R_3 defines if an additional read-out error occurs (spin non-preserving radiative transitions).

the $m_S = 0, +1$ energy levels of the ground states.

The interaction between the two level system and a short laser pulse is modeled using a Monte Carlo simulation, where a random number generator (RNG) is used to select the possible outcomes of the absorption and emission processes, described in Sec. 1.4. The flowchart of the code is shown in Fig. 4.5. We assume the two-level system to be in an initial state ρ. The absorption rate is taken into account in the two-level model by considering a finite probability of applying a z–QPM. The probability of the system to be in $m_S = 0$ after the laser excitation is equal to the probability of the system to initially be in $|0\rangle$ and be excited via a spin preserving transition plus a small correction to the z–QPM given by the probability of the system to initially be in $|1\rangle$ and be excited via a forbidden spin non-preserving transition, i.e., $P_0^{(\mathrm{e})} = \frac{\Gamma_\mathrm{e}}{\gamma_\mathrm{e}+\Gamma_\mathrm{e}} \mathrm{Tr}[\rho\,|0\rangle\langle 0|] + \frac{\gamma_\mathrm{e}}{\gamma_\mathrm{e}+\Gamma_\mathrm{e}}(1 - \mathrm{Tr}[\rho\,|0\rangle\langle 0|]) = \mathrm{Tr}[\rho\,|0\rangle\langle 0|](1 - 2\sin^2\theta) + \sin^2\theta$, where $\sin^2\theta = \frac{\gamma_\mathrm{e}}{\gamma_\mathrm{e}+\Gamma_\mathrm{e}} \simeq 0.037$ is the relative probability of having a spin non-preserving transition [Tab. 1.1]. Once in the excited state, if the system spin projection is $m_S = +1$, it has a probability $\Gamma_{1m}/(\Gamma_{1m}+\Gamma_{eg}) \simeq 0.44$ to be reinitialized into $|0\rangle$. This reinitialization phenomenon originates the dissipative nature of the map. If not reinitialized, the system radiatively decays back into the ground state with a small probability to do it via a forbidden spin non-preserving transition. Both z–QPMs and dissipation processes are considered to be instantaneous.

A single trajectory of the two level system throughout the entire protocol is obtained by cyclically applying unitary evolution operators to the qubit and applying RNG-based instantaneous laser interactions. The unitary part of the evolution is calculated by solving the equation of motion for $\mathcal{H}$ [Eq. (4.1)]. The two-level model is able to predict the dynamics of the system by averaging a large enough amount of simulated single trajectories. In Fig. 4.6 we compare the results obtained for the TPM scheme experimentally and numerically. The effective absorption probability $p_\mathrm{abs} = 0.69$ was the only free parameter fitted to the experimental data. The fact that $p_\mathrm{abs} > p_\mathrm{abs}^{(7)}$ is a consequence of the neglected photodynamics occurring through the hidden physical states (excited triplet and metastable level). The simulations for all the experiments presented in this chapter [Figs. 4.2 and 4.3] were realized by using an effective photon absorption probability p_abs in the range 18 - 69 %

In the limit of absorption probability equal to one, the time distribution of effective consecutive absorptions is no longer stochastic. Hence, it is possible to model the dynamics with an analytic solution that includes z–QPMs and dissipation, as will be described in the following section.

4.3.2 Non-stochastic limit and analytic solution

In this section we describe a super-operators formalism [175], that we use to model the stochastic dissipative dynamics of the spin qubit. The evolution of system state is described by

$$\mathrm{col}(\varrho(t)) = \boldsymbol{\mathcal{G}}\,\mathrm{col}(\varrho(t=0)) \tag{4.8}$$

where ϱ is the density matrix, $\mathrm{col}(\varrho)$ denotes the result of stacking its columns in order to obtain a vector of dimension $N^2 = 4$ ($N = 2$ is the dimension of the Hilbert

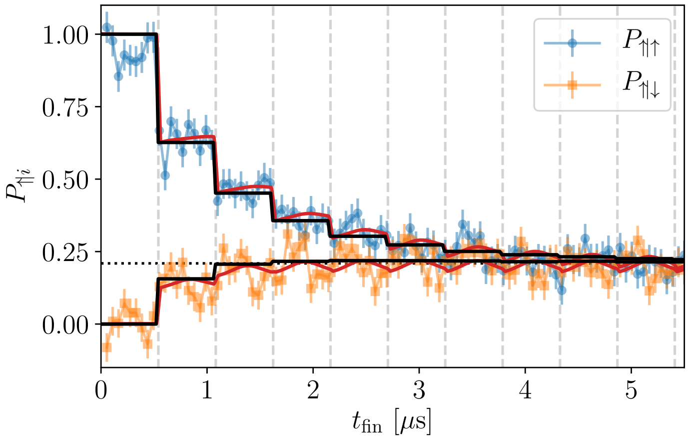

Figure 4.6: Simulations (solid lines) and experimental data (dots), for $\delta = -\Omega$ and inter-pulse time $\tau = 2\pi/\omega$ in the TPM protocol. Vertical dashed lines correspond to the temporal position of the short laser pulses. The red lines are obtained with the 7-level model, and absorption probability $p_{\text{abs}}^{(7)} = 0.45$. The black lines represent the numerical simulation obtained for the effective two-level model, and an effective absorption probability $p_{\text{abs}} = 0.69$. Adapted from Ref. [19].

space of the quantum system), and $\boldsymbol{\mathcal{G}}$ is the propagator defined as a $N^2 \times N^2$ matrix

$$\begin{aligned} \boldsymbol{\mathcal{G}} = \exp\Bigg[-t\Bigg(& i\,(\mathcal{H} \otimes \mathbb{1} - \mathbb{1} \otimes \mathcal{H}^*) \\ & + \sum_{m=1}^{M} L_m^\top \otimes L_m - \frac{1}{2}\mathbb{1} \otimes L_m^\dagger L_m - \frac{1}{2} L_m^\dagger L_m \otimes \mathbb{1} \Bigg) \Bigg] \end{aligned} \tag{4.9}$$

where $\mathcal{H}$ and L_m are the Liouville matrices for the Hamiltonian operator and for a set of Lindbladian jump operators, respectively. Here $\otimes$ stands for Kronecker product. Notice that the for the present chapter the Liouville matrix representation of the operators is done using as basis the eigenstates of σ_z

$$|0\rangle\langle 0| \rightarrow \begin{pmatrix} 1 & 0 \\ 0 & 0 \end{pmatrix} \quad ; \quad |1\rangle\langle 1| \rightarrow \begin{pmatrix} 0 & 0 \\ 0 & 1 \end{pmatrix}. \tag{4.10}$$

Model for the composition of z–QPMs and unitary evolutions

In this section we study the simplest case, without dissipation, in order to introduce the super-operator formalism and to investigate the effect of ideal projective measurements.

The protocol studied here consists on applying z–QPMs alternated with evolutions under the Hamiltonian $\mathcal{H}$ [Eq. (4.1)]. The quantum system evolves under the composition of unitary dynamics and measurement processes, which on average can be modelled by Lindbladian jump operators. As we measure σ_z, the two measurement projectors are $|0\rangle\langle 0|$ and $|1\rangle\langle 1|$ and thus the jump operators are just equal to $\sqrt{\Gamma_m}\,|0\rangle\langle 0|$ and $\sqrt{\Gamma_m}\,|1\rangle\langle 1|$ acting for the time t_{L}. The propagator associated with this two operators is calculated with Eq. (4.9). Since the optical transitions are very fast with respect to the coherent driving, we can neglect the Hamiltonian part. In addition, ideal projective measurements are obtained in the limit $\Gamma_m t_{\text{L}} \rightarrow \infty$, giving as a result the super-operator propagator

$$\boldsymbol{M} \equiv \frac{1}{2}(\mathbb{1}_{4\times 4} + \sigma_z \otimes \sigma_z). \tag{4.11}$$

Notice that $\boldsymbol{M}$ is a measurement projector, indeed, $\boldsymbol{M}^2 = \boldsymbol{M}$. On the other hand, the unitary evolution of the system is described by Eq. (4.9) without Lindbladian terms

$$\boldsymbol{U} \equiv \exp\left[-i\tau\left(\mathcal{H} \otimes \mathbb{1}_{2\times 2} - \mathbb{1}_{2\times 2} \otimes \mathcal{H}^*\right)\right]. \tag{4.12}$$

As a result, after having prepared the system in a thermal state at temperature β_{in}, the super-operator governing its evolution is given by applying n times the composition $\boldsymbol{MU}$, with n number of measurements, allowing us to introduce the super-operator $\boldsymbol{S}^n \equiv (\boldsymbol{MU})^n = \boldsymbol{M}(\boldsymbol{MUM})^{n-1}$, where the first unitary evolution super-operator was neglected because the system is initialized in one of the Hamiltonian eigenstates. Introducing for calculation purposes the quantities $\boldsymbol{N} \equiv \frac{1}{2}(\sigma_x \otimes \sigma_x - \sigma_y \otimes \sigma_y)$ and

$$\mu \equiv 1 - 2\sin^2(\alpha)\sin^2(\frac{\omega\tau}{2}), \tag{4.13}$$

we can derive an analytic expression for $\boldsymbol{S}^n$, i.e.

$$\boldsymbol{S}^n = \boldsymbol{M}(\boldsymbol{MUM})^{n-1} = \frac{1}{2}\left[(1+\mu^{n-1})\boldsymbol{M} + (1-\mu^{n-1})\boldsymbol{N}\right]. \tag{4.14}$$

The proof of this equality is given in Appendix 4.E.

In a two-level system we can compute the full statistics of energy variation ΔE, as well as the QJE $\langle e^{-\beta_{\text{in}}\Delta E}\rangle$, from $P_{\uparrow|\uparrow}$ and $P_{\uparrow|\downarrow}$. These conditional probabilities are measured after the qubit evolution

$$P^{(n)}_{\uparrow|i} = \text{Tr}\left[\varrho_\uparrow \ \text{col}^{-1}(\boldsymbol{S}^n \, \text{col}(\varrho_i))\right], \tag{4.15}$$

where col^{-1} is the opposite operation of col, i.e., col^{-1} converts a vectorized state of dimension N^2 into a square density matrix of dimension $N \times N$. The two Hamiltonian eigenstates are

$$\text{col}(\varrho_\uparrow) = \frac{1}{2}[1+\cos\alpha, -\sin\alpha, -\sin\alpha, 1-\cos\alpha] \tag{4.16}$$

and

$$\text{col}(\varrho_\downarrow) = \frac{1}{2}[1-\cos\alpha, +\sin\alpha, +\sin\alpha, 1+\cos\alpha]. \tag{4.17}$$

Therefore, the energy jump conditional probabilities are

$$P^{(n)}_{\uparrow|\substack{\uparrow\\\downarrow}} = \frac{1}{2}(1 \pm \mu^{n-1}\cos^2\alpha), \tag{4.18}$$

where the notation $\substack{\uparrow\\\downarrow}$ indicates the two possible initial states, each of which must be respectively associated with the $\pm$ sign in the r.h.s. of the equation. Notice that in the asymptotic limit

$$\lim_{n\to\infty}\mu^n = \begin{cases} 1, & \text{if } \ \alpha\!=\!0 \ \text{ or } \ \frac{\omega\tau}{2\pi}\!\in\!\mathbb{Z} \\ 0, & \text{otherwise} \end{cases} \tag{4.19}$$

Let us remember that by definition $\alpha \in [-\frac{\pi}{2}, \frac{\pi}{2}]$. This means that in the absence of dissipation $P^\infty_{\uparrow|\uparrow} = P^\infty_{\uparrow|\downarrow} = \frac{1}{2}$, i.e., z–QPMs bring the system into an equilibrium thermal state with infinite temperature [142, 173]. The cases where $\mu = 1$ are exceptions, for which $\boldsymbol{S}^n = \boldsymbol{M}$ (see *corollary II* in Appendix 4.E). If $\alpha = 0$, then the energy eigenstates, resulting from the first energy measurement, are not affected by $\boldsymbol{S}^n$. For τ equal to full periods of the coherent driving, $\boldsymbol{U}$ is the identity, therefore only the first z–QPM affects the spin energy.

Model for the composition of z–QPMs and unitary evolutions with dissipation

We now introduce the additional dissipative channel associated to each absorbed laser pulse. This model would reproduce the experimental conditions only for the case of $p_{\rm abs} = 1$, i.e., a completely deterministic (non-stochastic) time distribution of absorbed laser pulses.

The decay towards the $|0\rangle$ state can be modeled on average by the Lindbladian jump operator $\sqrt{\Gamma_{\mathcal{D}}}\,|0\rangle\langle 1|$ acting during the laser time $t_{\rm L}$. This jump operator gives rise to a new super-operator $\boldsymbol{\mathcal{D}}$ defined using Eq. (4.9) neglecting the Hamiltonian terms, as we did for the z–QPM superoperator M. The presence of each absorbed laser pulse is therefore described by the super-operator $\boldsymbol{\mathcal{D}M} = \boldsymbol{M\mathcal{D}}$. Therefore, the expression of the super-operator for the global dynamical evolution of the NV-center is equal to

$$\boldsymbol{S}^n_{\boldsymbol{\mathcal{D}}} = (\boldsymbol{\mathcal{D}MU})^n = \boldsymbol{M\mathcal{D}}^{1/2}(\boldsymbol{M\mathcal{D}}^{1/2}\boldsymbol{U\mathcal{D}}^{1/2}\boldsymbol{M})^{n-1}\boldsymbol{\mathcal{D}}^{1/2}\boldsymbol{M}, \tag{4.20}$$

where in the r.h.s. of Eq. (4.20) we have not considered the last unitary evolution, since the map is applied to the energy eigenstates. In a similar fashion to the case studied in the previous section, it is possible to prove (see appendix 4.F) that the energy jump conditional probability corresponds to

$$P^{(n)}_{\uparrow|{}^{\uparrow}_{\downarrow}} = \frac{1}{2}[1 + \cos\alpha(R_n \pm \mu^{n-1}e^{-n\Gamma_{\mathcal{D}}t_{\rm L}}\cos\alpha)], \tag{4.21}$$

where

$$R_n \equiv \frac{1 - e^{-\Gamma_{\mathcal{D}}t_{\rm L}}}{1 - \mu e^{-\Gamma_{\mathcal{D}}t_{\rm L}}}(1 - \mu^n e^{-n\Gamma_{\mathcal{D}}t_{\rm L}}) \tag{4.22}$$

and the notation ${}^{\uparrow}_{\downarrow}$ indicates the two possible initial states, each of which must be respectively associated with the ± sign in the r.h.s. of the equation (4.21). Notice that $\Gamma_{\mathcal{D}}$ is an effective dissipation rate such that $1 - e^{-\Gamma_{\mathcal{D}}t_{\rm L}} = 0.44$ ($\simeq p_{\rm diss}$ for a single absorption-emission cycle).

As mentioned before, in the asymptotic limit [Eq. (4.19)] $\lim_{n\to\infty}\mu^n \to 0$, except for trivial cases where the action of $\boldsymbol{U}$ becomes irrelevant and the map brings the spin state to the state $|0\rangle$. Therefore, for any non trivial case ($\mu \neq 1$) the asymptotic probability to find the spin in the $|\uparrow\rangle$ state $P^{\infty}_{\uparrow} = P^{\infty}_{\uparrow|\uparrow} = P^{\infty}_{\uparrow|\downarrow}$ can be analytically computed, yielding

$$P^{\infty}_{\uparrow} = \frac{1}{2}\left(1 - \frac{\left(1 - e^{-t_{\rm L}\Gamma_{\mathcal{D}}}\right)\cos\alpha}{1 - e^{-t_{\rm L}\Gamma_{\mathcal{D}}}\mu}\right). \tag{4.23}$$

The analytic prediction of $P^{\infty}_{\uparrow}$ matches the numerical simulations for ideal equally-spaced z–QPMs [Fig. 4.7].

In the experiment, the stochastic temporal distribution of z–QPMs — induced by an absorption probability lower than one — removes the strong dependence on τ, as will be discussed in the next section. The analytic model is therefore a good approximation of the system dynamics, provided one replaces τ with an effective inter-pulse spacing.

4.3.3 Stochastic limit

The absorption probability can be accounted for in the analytical solution by considering an effective parameter $\mu_{\rm eff}$ that takes into account the probability distribution

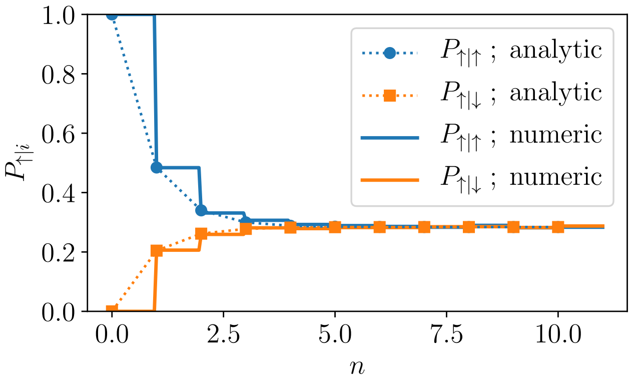

Figure 4.7: Comparison between numerical and analytical calculation for the case of $p_{\text{abs}} = 1$ (non-stochastic). The conditional probability to measure $E_\uparrow$ at the end of the TPM protocol, starting from the energy eigenstates $\varrho_\uparrow$ (blue) or $\varrho_\downarrow$ (orange), is shown as a function of the number of laser pulses n. In this particular case $\sin^2 \alpha = 0.5$ and $\sin^2(\omega\tau/2) = 0.5$, meaning that $\mu = 0.5$. The sum of square residuals between the two simulations is lower than 2×10^{-4}.

of free evolution time-intervals between consecutive absorbed laser pulses. In this section we explain how μ_{eff} is obtained by analyzing all the possible combinations of absorbed laser pulses and their probability.

Notice that the time before the first absorption is irrelevant because the system is initialized into each one of the Hamiltonian eigenstates, and the time after the last absorption is also irrelevant because the energy of the system is measured at the end of the protocol. It is for this reason that in the case with one laser pulse $n = 1$, the dependency on τ for Eq. (4.21) is removed.

For n laser pulses, the number of absorbed lasers k can take any integer value between 0 and n. The time between laser pulses τ is fixed, however, the time between two absorbed laser pulses τ_a can change in each realization of the experiment. Notice that the value of τ is irrelevant for $k = 0$ and $k = 1$, hence, to define the time between two consecutive absorbed laser pulses τ_a, we only consider the cases for $k \geq 2$. For n laser pulses, τ_a can take any value between τ (absorbing two laser pulses next to each other) and $(n-1)\tau$ (absorbing only the very first pulse and the very last one). Therefore, we can write that $\tau_a = m\tau$ for $m \in [1, 2, \ldots, n-1]$. For each value of k, there are $\frac{n!}{k!(n-k)!}$ possible combinations for the position of the absorbed laser pulses. Each of these combinations is associated with a specific set of m values. Hence, for a fixed k, we define $N(m|k)$ as the number of appearances of each value of m for all these sets. Then we obtain the probability $f_m(n, p_{\text{abs}})$ of having $\tau_a = m\tau$, by summing the appearances of each m value over all possible k values

$$f_m(n, p_{\text{abs}}) = \frac{\sum_k N(m,k) b(k, n, p_{\text{abs}})}{\sum_m \sum_k N(m,k) b(k, n, p_{\text{abs}})}, \tag{4.24}$$

where the binomial distribution $b(k, n, p_{\text{abs}})$ describes the probability of having k absorbed pulses, each with an absorption probability p_{abs}, in a set of n laser pulses. An illustrative example on how to do this procedure is shown in Section [4.3.4].

From the probability distribution $f_\ell(n, p_{\text{abs}})$ defined in Eq. (4.24) we extract an

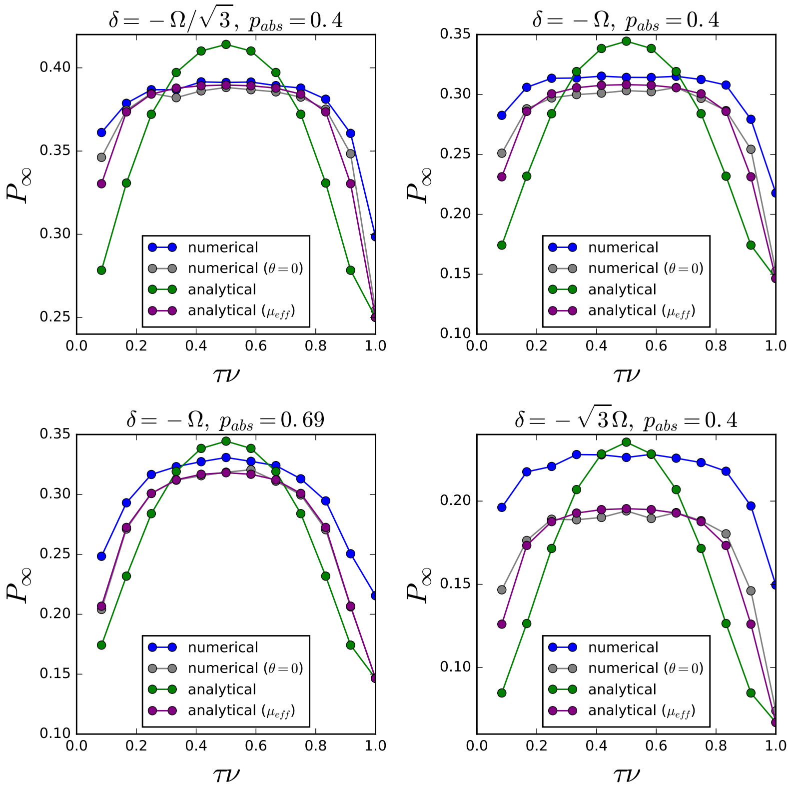

Figure 4.8: Comparison between numerical and analytical calculation of the asymptotic probability for the spin to be in the $|\uparrow\rangle$ state, as a function of the time between laser pulses τ. Respectively in blue and gray: Numerical simulation with the complete model, and without non-preserving spin transitions, i.e. $\theta = 0$ (see Tab. 1.1). In green and purple: Analytical solution for perfect absorption, and finite absorption ($\mu_{\text{eff}}(p_{\text{abs}})$, see text), respectively. Time τ is scaled in terms of energy $\nu = \omega/2\pi$ ($\hbar = 1$).

effective value of μ_{eff} as:

$$\mu_{\text{eff}}(p_{\text{abs}}) = \sum_{\ell=1}^{n} \mu_\ell \, f_\ell(n, p_{\text{abs}}) \tag{4.25}$$

where $\mu_\ell = 1 - 2\sin^2(\alpha)\sin^2(\frac{\ell\tau\omega}{2})$. In Fig. 4.8 we present the comparison between the numerical simulation and the analytical solution using both $\mu_{\text{eff}}(p_{\text{abs}})$ (finite absorption probability) and μ (perfect absorption). This μ_{eff} correctly takes into account the finite absorption probability, however the analytical solution is still missing a description of the non-preserving spin radiative transition process, which is more important as we reduce the value of α, as shown in Fig. 4.8.

4.3.4 Stochastic limit – Illustrative example for $n = 4$

In order to clarify the procedure explained in the previous section, lets consider as an example the case of $n = 4$ laser pulses, each with a 40% probability of absorption ($p_{\text{abs}} = 0.4$). Lets also assume that the time between laser pulses τ is such that $\omega\tau = \pi/2$.

The number of time intervals between consecutive absorbed laser pulses can be $\tau_a = m\tau \in \{\tau, 2\tau, 3\tau\}$. Assuming that two laser pulses are absorbed ($k = 2$), then the positions of the laser pulses that have been absorbed can be any of the ones shown in table 4.1. From this table we can also see that $m = 1$ occurs in three cases, $m = 2$ occurs in two cases, and $m = 3$ occurs in only one case. Therefore, $N(m, k)$ corresponds to

$$N(1, 2) = 3 \quad ; \quad N(2, 2) = 2 \quad ; \quad N(3, 2) = 1$$

The cases for $k = 3$ and $k = 4$ absorbed laser pulses are also shown in table 4.1, from which we can obtain that

$$\begin{aligned} N(1, 3) = 6 \quad ; \quad N(2, 3) = 2 \quad ; \quad N(3, 3) = 0 \\ N(1, 4) = 3 \quad ; \quad N(2, 4) = 0 \quad ; \quad N(3, 4) = 0 \end{aligned}$$

Hence, using Eq. (4.24) we obtain

$$\begin{aligned} f_1(4, p_{\text{abs}} = 0.4) &= 0.63\overline{8} \\ f_2(4, p_{\text{abs}} = 0.4) &= 0.2\overline{7} \\ f_3(4, p_{\text{abs}} = 0.4) &= 0.08\overline{3}, \end{aligned}$$

Finally we use Eq. (4.25) to calculate

$$\begin{aligned} \mu_{\text{eff}}(p_{\text{abs}} = 0.4) &= 1 - 2\sin^2(\alpha) \sum_{\ell=1}^{3} \sin^2\left(\frac{\ell\tau\omega}{2}\right) f_\ell(n, p_{\text{abs}}) \\ &\simeq 1 - 2(0.63\overline{8}) \sin^2(\alpha) \end{aligned}$$

in contrast, $\mu = 1 - \sin^2(\alpha)$ for the non-stochastic case (perfect absorption $p_{\text{abs}} = 1.0$) [Eq. (4.13)].

Table 4.1: Illustrative example: Positions of the k absorbed laser pulses, marked with X, for $n = 4$ laser pulses. Each value of $k \in [2, 3, 4]$ is shown as a separated case. The last column in each case shows the number of time intervals between absorbed laser pulses, i.e., the number of dashed lines between X-markers.

$k = 2$

Absorption position				m
X	X	-	-	1
-	X	X	-	1
-	-	X	X	1
X	-	X	-	2
-	X	-	X	2
X	-	-	X	3

$k = 3$

Absorption position				m
X	X	X	-	1,1
-	X	X	X	1,1
X	-	X	X	2,1
X	X	-	X	1,2

$k = 4$

Absorption position				m
X	X	X	X	1,1,1

4.4 Conclusions

We explored the quantum energy exchange fluctuation relation for an open quantum system coupled to a tunable dissipative channel, and we investigated the interplay between quantum projective measurements and dissipation. For the studied two-level quantum system, the energy exchange fluctuation relation is formulated in terms of the pseudo-temperatures of the initial and asymptotic states of the system.

At the steady state, the final pseudo-temperature is indeed an invariant quantity, irrespective of the initial state. We have shown that this exchange fluctuation relation holds for any direction, with respect to the Hamiltonian, along which the intermediate quantum projective measurements are applied. In addition, we have observed that the exchange fluctuation relation is robust against the presence of randomness in the time intervals between measurements. Our experimental study is enabled by the use of a single NV center in diamond at room temperature. We exploit the high control on the spin degrees of freedom, under the effect of trains of short laser pulses that perform quantum projective measurements and controllably open the two-level system, through a dissipation channel whose interaction coupling with the external surroundings can be tuned. This work, therefore, establishes NV centers as a suitable platform to to explore the physics of an out-of-equilibrium open quantum system, and to verify quantum fluctuation relations.

4.E Appendix: Super-operator for ideal projective measurements

This appendix contains the proof by induction of the equality:

$$(\boldsymbol{MUM})^n = \frac{1}{2}\left[(1+\mu^n)\boldsymbol{M} + (1-\mu^n)\boldsymbol{N}\right] \tag{4.26}$$

Proof: By direct substitution in Eqs. (4.11) and (4.12), one can obtain that

$$\begin{aligned}
\boldsymbol{MUM} &= \begin{pmatrix} 1-\sin^2\alpha\ \sin^2\omega t & 0 & 0 & \sin^2\alpha\ \sin^2\omega t \\ 0 & 0 & 0 & 0 \\ 0 & 0 & 0 & 0 \\ \sin^2\alpha\ \sin^2\omega t & 0 & 0 & 1-\sin^2\alpha\ \sin^2\omega t \end{pmatrix} \\
&= \frac{1}{2}(1+\mu)\begin{pmatrix} 1 & 0 & 0 & 0 \\ 0 & 0 & 0 & 0 \\ 0 & 0 & 0 & 0 \\ 0 & 0 & 0 & 1 \end{pmatrix} + \frac{1}{2}(1-\mu)\begin{pmatrix} 0 & 0 & 0 & 1 \\ 0 & 0 & 0 & 0 \\ 0 & 0 & 0 & 0 \\ 1 & 0 & 0 & 0 \end{pmatrix} \\
&= \frac{1}{2}\left[(1+\mu)\boldsymbol{M} + (1-\mu)\boldsymbol{N}\right]
\end{aligned}$$

where $\mu \equiv 1 - 2\sin^2(\alpha)\sin^2(\frac{\omega\tau}{2})$. This proofs the validity of Eq. (4.26) for $n = 1$. Assuming it to be valid for $n-1$, and using the fact that $\boldsymbol{M}^2 = \boldsymbol{N}^2 = \boldsymbol{M}$ and $\boldsymbol{MN} = \boldsymbol{NM} = \boldsymbol{N}$, then:

$$\begin{aligned}
(\boldsymbol{MUM})^n &= (\boldsymbol{MUM})^{n-1}(\boldsymbol{MUM}) \\
&= \frac{1}{2}\left[(1+\mu^{n-1})\boldsymbol{M} + (1-\mu^{n-1})\boldsymbol{N}\right]\cdot\frac{1}{2}\left[(1+\mu)\boldsymbol{M} + (1-\mu)\boldsymbol{N}\right] \\
&= \frac{1}{4}\left[(1+\mu^{n-1})(1+\mu) + (1-\mu^{n-1})(1-\mu)\right]\boldsymbol{M} \\
&\quad + \frac{1}{4}\left[(1+\mu^{n-1})(1-\mu) + (1+\mu^{n-1})(1-\mu)\right]\boldsymbol{N} \\
&= \frac{1}{2}\left[(1+\mu^n)\boldsymbol{M} + (1-\mu^n)\boldsymbol{N}\right]
\end{aligned}$$

Q.E.D.

Corollary I: Eq. (4.14) is a direct consequence of equation (4.26).
Corollary II: If $\mu = 1$ then $(\boldsymbol{MUM})^n = \boldsymbol{M}$

4.F Appendix: Super-operator for z-QPMs and dissipation

This appendix is devoted to demonstrate the validity of Eq. (4.21).

The dissipation operator $\boldsymbol{\mathcal{D}}$ is obtained with Eq. (4.9) with the Lindbladian jump operator $\sqrt{\Gamma_{\mathcal{D}}}\,|0\rangle\langle 1|$, and neglecting the Hamiltonian terms (instantaneous action of the laser pulses with respect to the coherent driving). This results in

$$\boldsymbol{\mathcal{D}}^{1/2} = \begin{pmatrix} 1 & 0 & 0 & 1-\sqrt{k} \\ 0 & \sqrt[4]{k} & 0 & 0 \\ 0 & 0 & \sqrt[4]{k} & 0 \\ 0 & 0 & 0 & \sqrt{k} \end{pmatrix} \tag{4.27}$$

where $k \equiv e^{-t_{\mathrm{L}}\Gamma_{\mathcal{D}}}$. This means that

$$\boldsymbol{M}\boldsymbol{\mathcal{D}}^{1/2} = \begin{pmatrix} 1 & 0 & 0 & 1-\sqrt{k} \\ 0 & 0 & 0 & 0 \\ 0 & 0 & 0 & 0 \\ 0 & 0 & 0 & \sqrt{k} \end{pmatrix} \tag{4.28}$$

and

$$\boldsymbol{S}_{1/2} = \begin{pmatrix} 1-\sqrt{k}k_1 & 0 & 0 & 1-k-\sqrt{k}(1-2\sqrt{k})k_1 \\ 0 & 0 & 0 & 0 \\ 0 & 0 & 0 & 0 \\ \sqrt{k}k_1 & 0 & 0 & k+\sqrt{k}(1-2\sqrt{k})k_1 \end{pmatrix} \tag{4.29}$$

where $\boldsymbol{S}_{1/2} \equiv \boldsymbol{M}\boldsymbol{\mathcal{D}}^{1/2}\boldsymbol{U}\boldsymbol{\mathcal{D}}^{1/2}\boldsymbol{M}$ and $k_1 = \sin^2(\alpha)\sin^2(\frac{\omega\tau}{2})$ are defined to simplify notation. Introducing for calculation purposes the matrices

$$\boldsymbol{B}_1 \equiv \frac{1}{2}\begin{pmatrix} 1 & 0 & 0 & 1 \\ 0 & 0 & 0 & 0 \\ 0 & 0 & 0 & 0 \\ 1 & 0 & 0 & 1 \end{pmatrix} \; ; \; \boldsymbol{B}_2 \equiv \frac{1}{2}\begin{pmatrix} 1 & 0 & 0 & -1 \\ 0 & 0 & 0 & 0 \\ 0 & 0 & 0 & 0 \\ -1 & 0 & 0 & 1 \end{pmatrix} \; ; \; \boldsymbol{B}_3 \equiv \frac{1}{2}\begin{pmatrix} 1 & 0 & 0 & 1 \\ 0 & 0 & 0 & 0 \\ 0 & 0 & 0 & 0 \\ -1 & 0 & 0 & -1 \end{pmatrix}, \tag{4.30}$$

we can rewrite equations (4.28) and (4.29) as

$$\boldsymbol{M}\boldsymbol{\mathcal{D}}^{1/2} = \boldsymbol{B}_1 + \sqrt{k}\boldsymbol{B}_2 + (1-\sqrt{k})\boldsymbol{B}_3 \tag{4.31}$$

$$\boldsymbol{S}_{1/2} = \boldsymbol{B}_1 + k\mu\boldsymbol{B}_2 + (1-k\mu-\sqrt{k}(1-\mu))\boldsymbol{B}_3. \tag{4.32}$$

Note that these $\boldsymbol{B}$ matrices have the properties:

$$\begin{gathered} \boldsymbol{B}_1^2 = \boldsymbol{B}_1 \quad ; \quad \boldsymbol{B}_2^2 = \boldsymbol{B}_2 \quad ; \quad \boldsymbol{B}_3\boldsymbol{B}_1 = \boldsymbol{B}_2\boldsymbol{B}_3 = \boldsymbol{B}_3 \\ \boldsymbol{B}_3^2 = \boldsymbol{B}_1\boldsymbol{B}_3 = \boldsymbol{B}_3\boldsymbol{B}_2 = \boldsymbol{B}_1\boldsymbol{B}_2 = \boldsymbol{B}_2\boldsymbol{B}_1 = \mathbb{0}_{3\times 3}, \end{gathered}$$

therefore

$$\begin{aligned} (\boldsymbol{S}_{1/2})^2 &= \boldsymbol{B}_1 + (k\mu)^2\boldsymbol{B}_2 + (1-k\mu-\sqrt{k}(1-\mu))(1+k\mu)\boldsymbol{B}_3 \\ (\boldsymbol{S}_{1/2})^3 &= \boldsymbol{B}_1 + (k\mu)^3\boldsymbol{B}_2 + (1-k\mu-\sqrt{k}(1-\mu))(1+k\mu+(k\mu)^2)\boldsymbol{B}_3 \\ (\boldsymbol{S}_{1/2})^4 &= \boldsymbol{B}_1 + (k\mu)^4\boldsymbol{B}_2 + (1-k\mu-\sqrt{k}(1-\mu))(1+k\mu+(k\mu)^2+(k\mu)^3)\boldsymbol{B}_3 \\ &\vdots \\ (\boldsymbol{S}_{1/2})^n &= \boldsymbol{B}_1 + (k\mu)^n\boldsymbol{B}_2 + (1-k\mu-\sqrt{k}(1-\mu))\left(\sum_{i=0}^{n}(k\mu)^i\right)\boldsymbol{B}_3 \end{aligned}$$

Hence, using the equation of the sum of the first n terms of a geometric series, we obtain

$$(\boldsymbol{S}_{1/2})^n = \boldsymbol{B}_1 + (k\mu)^n\boldsymbol{B}_2 + (1-k\mu-\sqrt{k}(1-\mu))\left(\frac{1-(k\mu)^n}{1-k\mu}\right)\boldsymbol{B}_3 \tag{4.33}$$

Combining equations (4.31) and (4.33), and using the properties of matrices $\boldsymbol{B}$, we can obtain the super-operator for the global dynamical evolution [Eq. (4.20)]

$$\begin{aligned} \boldsymbol{S}_{\boldsymbol{\mathcal{D}}}^n &= \boldsymbol{M}\boldsymbol{\mathcal{D}}^{1/2}(\boldsymbol{S}_{1/2})^{n-1}\boldsymbol{\mathcal{D}}^{1/2}\boldsymbol{M} \\ &= \boldsymbol{B}_1 + k^n\mu^{n-1}\boldsymbol{B}_2 + R_n\boldsymbol{B}_3, \end{aligned} \tag{4.34}$$

where $R_n \equiv (1-k)\left(\frac{1-(k\mu)^n}{1-k\mu}\right)$.

The propagator given in Eq. (4.34) can be used to estimate the conditional probabilities $P^{(n)}_{\uparrow|\substack{\uparrow\\ \downarrow}}$ for the initial energy eigenstates $\varrho_\uparrow$ [Eq. (4.16)] and $\varrho_\downarrow$ [Eq. (4.17)]

$$\begin{aligned} P^{(n)}_{\uparrow|\substack{\uparrow\\ \downarrow}} &= \mathrm{Tr}\left[\varrho_\uparrow \ \mathrm{col}^{-1}(\boldsymbol{S}^n_{\boldsymbol{\mathcal{D}}}\,\mathrm{col}(\varrho_{\substack{\uparrow\\ \downarrow}}))\right] \\ &= \frac{1}{2}\left(1 + R_n\cos\alpha \pm k^n\mu^{n-1}\cos^2\alpha\right), \end{aligned} \tag{4.35}$$

which is exactly the expression in Eq. (4.21).

Chapter 5

Thermodynamics of non-thermal quantum dissipation

The study of stochastic dissipative quantum dynamics has been subject of an enduring interest, and it plays a key role for the characterization of open quantum systems dynamics [176]. A purely quantum way of inducing stochastic dynamics is realized, as presented in Chapter 4, by performing projective measurements or, possibly, sequences of them. In such a case, the system evolves following random trajectories, since after each measurement the system notoriously collapses in an eigenstate of the measured observable with an assigned probability [177, 178]. Thus, to compute the average values of physical quantities, one needs to average over all the different trajectories. In this context, it becomes evident how useful it is to have an experimental setting in which both the stochasticity and dissipation are present, and even tunable from weak to strong coupling between the system and its environment. Whilst two-level systems, such as the spin qubit discussed in Chapter 4, grant the possibility of studying pseudo-thermalizing dynamics, a quantum system with higher dimension provides an ideal playground towards the study of non-thermal dissipative dynamics.

In this chapter, we will focus on the simplest physical system in which one can address the issue of characterizing non-thermal states, including quantum fluctuation relations, namely a three-level quantum system (3LS). In particular, our open 3LS is realized by the three electronic spin projections within the orbital ground state of an NV center in diamond at room temperature. Similarly to the scheme that I have discussed for a spin qubit, stochasticity is introduced by applying a sequence of projective measurements with finite probability to occur, while at the same time dissipation is provided by the irreversible optical pumping and non-radiative decay processes associated with the experimental realization of the projective measurements. The implemented stochastic dissipative quantum dynamics is then characterized by computing the expectation values of quantities ascribable to energy changes of the 3LS with respect to the initial (reference) state. In this way, we will study the effects that the stochastic dissipative map have in the probability distribution of energy variation, by resorting to the Jarzynski-Sagawa-Ueda (JSU) formalism for systems with feedback [144, 179] and exchange fluctuation relations for open quantum systems [19, 38, 162, 167, 180].

Section 5.1 discusses the implementation of the stochastic dissipative map with a spin qutrit, formed by the orbital ground state of an NV center. The description of the protocol to measure the energy variation statistics is given in Sec. 5.2, together with the experimental results of the energy jump probabilities. Section 5.3 presents

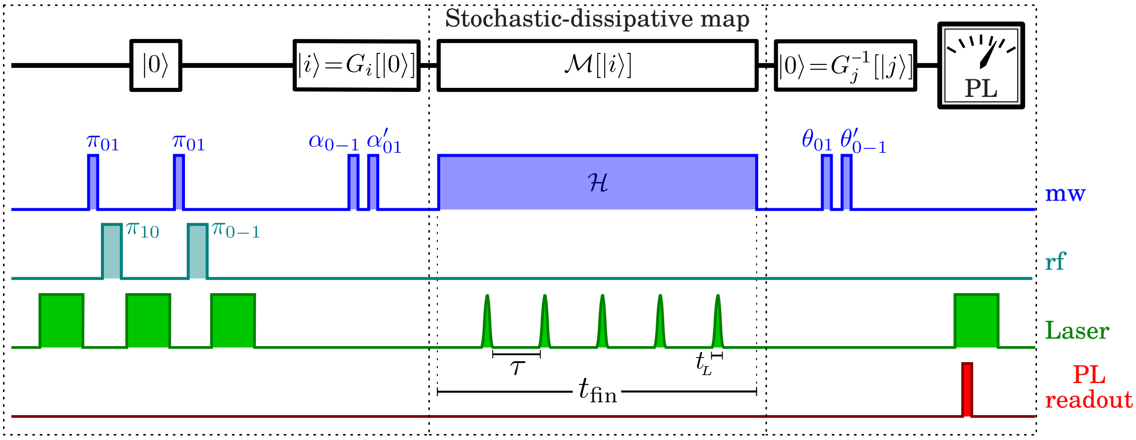

Figure 5.1: Protocol to measure energy conditional probabilities. The stochastic-dissipative map $\mathcal{M}$ is a combination of a train of N_{L} equidistant short laser pulses and a continuous driving under the Hamiltonian $\mathcal{H}$ that can be either $\mathcal{H}_{\text{NV}}$ or $\mathcal{H}_{\text{mw}}$ (see text). The initialization of the NV $|0\rangle$ state require some coherent control to polarize the nitrogen nuclear spin (see appendix 5.G for details). The gates $G_i : |0\rangle \to |i\rangle$, with $|i\rangle$ being one of the Hamiltonian eigenstates, enable to prepare and readout the Hamiltonian eigenstates, by exploiting the optical properties of the NV center (see appendix 5.H for details).

a model developed to predict the dynamics of the 3LS in the presence of unitary evolution, intermediate measurements and dissipation. In Sec. 5.4, this model is used to demonstrate the validity of a generalized version of the JSU relation, that includes irreversible dissipation processes. In addition we prove that the computation of the quantities involved in this relation can be significantly simplified. Moreover, we use the experimental data of the energy jump probabilities to reconstruct the characteristic function of the energy variation probability, and experimentally verify the generalized JSU relation. In Sec. 5.5, a theoretical analysis and the experimental data are used to show that it is possible to define an energy scale factor such that the characteristic function of the energy variation probability remains constant in time, under the assumption that the system is subject to dissipative (not necessarily thermalizing) dynamics. Section 5.6 contains the conclusions of this chapter.

5.1 Experimental implementation

In contrast with Chapter 4, here we use a three level system formed by the three spin projections of the $S = 1$ ground state of an NV center. The intrinsic Hamiltonian of the spin triplet reads (see Eq. (1.2))

$$\mathcal{H}_{\text{NV}} = \Delta S_z^2 + \gamma_e B S_z\,. \tag{5.1}$$

The zero-field-splitting $\Delta \simeq 2.87$ GHz removes the degeneracy of the $m_S = 0$ ($|0\rangle$) spin projection, while the product of the electron gyromagnetic ratio γ_e with the amplitude of an external bias magnetic field B, aligned with the NV center axis, removes the degeneracy of the spin projections $m_S = \pm 1$ ($|\pm 1\rangle$).

The spin qutrit is coherently driven using double-resonant microwave (mw) radiation. We use monochromatic mw signals to apply two level gates involving the states $|0\rangle$ and $|+1\rangle$ (respectively $|0\rangle$ and $|-1\rangle$), and bi-chromatic signals, with frequency components $\Omega_{\pm 1} = \Delta \pm \gamma_e B$, to apply a continuous double driving described by the following Hamiltonian in the microwave rotating frame:

$$\mathcal{H}_{\mathrm{mw}} \equiv \omega S_x \tag{5.2}$$

where ω is the Rabi frequency.[1] For the experiments shown in this chapter, we have used $\omega/2\pi \simeq 1.18$ MHz.

In a similar fashion to what I have presented in Chapter 4, the dissipative map $\mathcal{M}$ consists in a unitary evolution $U = \exp -i\mathcal{H}t_{\mathrm{fin}}$ during the time of the experiment t_{fin}, and a set of equidistant short laser pulses. We have separately explored the cases of $\mathcal{H} = \mathcal{H}_{\mathrm{mw}}$ and $\mathcal{H} = \mathcal{H}_{\mathrm{NV}}$. Even when the time between laser pulses is fixed, the low absorption probability implies that the time interval between two consecutive absorptions follows a binomial distribution with probability p_{abs}. Thus, we model the interaction with a short laser pulse as follows: If the laser pulse is not absorbed, the state of the system remains unchanged and there is no dissipation. If the laser pulse is absorbed, the system is subjected to a projective measurement in the S_z-basis [71] that is then followed by a dissipation towards the $|0\rangle$ state. This interaction between the 3LS and short laser pulses can be thus described by a positive operator valued measure (POVM) followed by a dissipation operator depending on the result of the POVM, as will be shown in Sec. 5.3.1.

5.1.1 Nuclear spin polarization

Owing to technical specifications on the microwave generator, the difference in frequency between the two components of the bi-chromatic microwave signal is set to $|\Omega_{+1} - \Omega_{-1}|/2 \leq 130$ MHz (see Sec. 1.2.1). This imposes a limit on the amplitude of the external bias field. In particular we set it to be $B \simeq 100$ MHz$/\gamma_e \simeq 35.7$ G. This magnetic field is far away from the excited-state level anti-crossing (ESLAC) [Sec. 1.5], hence the optical initialization of the NV electronic spin has almost no effect on the nitrogen nuclear spin polarization (see for example Fig. 1.2). The hyperfine coupling between the NV electronic spin (orbital ground state) and the unpolarized nitrogen nuclear spin results in a $3 \times 3 = 9$ level system. To reduce it to be the three level system described by Eq. (5.1), we polarize the nuclear spin at the beginning of each experimental realization by applying a set of mw and rf pulses as depicted in Fig. 5.1 and detailed in appendix 5.G. Notice that the nitrogen nuclear spin lifetime is of the order of milliseconds [5, 6], hence much longer that the duration of a single experimental realization, which in average is ~ 10 μs.

5.2 Measurement protocol

The effect of the map $\mathcal{M}$ on the energy of the system can be characterized by measuring the energy jump probabilities, i.e., the conditional probabilities associated with the energy variation in a given time interval. For this purpose, we use the following procedure:

(a) Initialize the spin into one of the Hamiltonian eigenstates, say $|i\rangle$.

(b) Evolve the spin under the map $\mathcal{M}$ up to the time instant t_{fin}.

(c) Read out the probability of the spin to be in the Hamiltonian eigenstate $|j\rangle$ at $t = t_{\mathrm{fin}}$.

---

[1] We remind the reader that, in the S_z basis, $S_x = \frac{1}{\sqrt{2}}\begin{pmatrix} 0 & 1 & 0 \\ 1 & 0 & 1 \\ 0 & 1 & 0 \end{pmatrix}$.

(d) repeat the procedure for each initial and final Hamiltonian eigenstates.
The conditional probability $P_{j|i}$ associated with each of the initial and final eigenstates is obtain by repeating this procedure several times ($\sim 10^6$). This protocol is schematized in Fig. 5.1. After optically initializing the system into $|0\rangle$, we apply a quantum gate G_i to prepare the Hamiltonian eigenstate $|i\rangle$. To measure the probability that the final state of the system is $|j\rangle$, we apply a second quantum gate G_j^{-1} that rotates $|j\rangle$ into $|0\rangle$, and finally we perform the optical readout. In other words, for a given final state $\rho = \mathcal{M}_{(t_{\text{fin}})}[|i\rangle\langle i|]$, we want to measure the probability $P_{j|i} = \text{Tr}[|j\rangle\langle j|\,\rho]$, however, the optical readout (measurement of the NV photoluminescence intensity) corresponds to a measurement of the probability of finding the system in the $m_S = 0$ state ($\text{Tr}[|0\rangle\langle 0|\,\rho]$). By applying a quantum gate to the state before its optical readout we measure $\text{Tr}[|0\rangle\langle 0|\; G_j^{-1}\rho G_j] = \text{Tr}[G_j\,|0\rangle\langle 0|\,G_j^{-1}\;\rho] = \text{Tr}[|j\rangle\langle j|\,\rho] = P_{j|i}$, which is the probability we are interested in measuring. Notice that the gates G_j are unitary transformations done with coherent mw driving. The description of these gates can be found in appendix 5.H.

We used the protocol explained above to measure the complete set of conditional probabilities for two different dissipative maps $\mathcal{M}$:

1. Double driving of the spin, the unitary part of the map $\mathcal{M}$ is ruled by the Hamiltonian $\mathcal{H}_{\text{mw}}$ as defined in Eq. (5.2), with eigenstates
$$|\pm\omega\rangle \equiv (|{-1}\rangle \pm \sqrt{2}\,|0\rangle + |1\rangle)/2 \;\text{ and }\; |\emptyset\rangle \equiv (|{-1}\rangle - |1\rangle)\,/\sqrt{2}\,.$$
2. Fee evolution of the spin (no driving), such that the Hamiltonian is $\mathcal{H}_{\text{NV}}$ with eigenstates $|\pm 1\rangle$ and $|0\rangle$.

The results of these measurements are shown in Fig. 5.2, where the x-axis represents the number of laser pulses N_{L} applied before performing the readout. The shown experimental data is accompanied by a simulation, the details of which will be described in Sec. 5.3.

From the results shown in Fig. 5.2, note that the conditional probabilities $P_{j|i}$ tend to a single constant value for long times $t_{\text{fin}} = \tau N_{\text{L}}$ (with large N_{L}). This is equivalent to state that the system asymptotically approaches a *steady state in the energy basis* (SSE) that does not depend on the initial state, thus confirming the dissipative nature of the map $\mathcal{M}$. In the case of $\mathcal{H} = \mathcal{H}_{\text{NV}}$ (see Fig. 5.2(b)), the asymptotic state is $|0\rangle$ that is obtained by applying several laser pulses without driving the system. This result is confirmed by the equivalence of this protocol with the procedure used to optically initialize the system into $|0\rangle$. On the other hand, if $\mathcal{H} = \mathcal{H}_{\text{mw}}$ (see Fig. 5.2(a)), the asymptotic state is not $|0\rangle = \frac{1}{\sqrt{2}}\,(|{+\omega}\rangle - |{-\omega}\rangle)$. Although the interaction with each laser pulse tends to bring the system into $|0\rangle$, the double driving after each laser pulse performs a partial Rabi oscillation, hence changing the SSE for long times.

Asymptotic state for $\mathcal{H}_{\text{mw}}$

The dissipative nature of the map implies that the fixed point of $\mathcal{M}$ coincides with the asymptotic state of the dynamics. Since the map is inside a TPM scheme, this means that we need to find the state ρ^∞ such that the diagonal elements of $\mathcal{M}[\rho^\infty]$ remain unaltered during the dynamics. Assuming that the fixed-point is a state written in its spectral decomposition as $\rho^\infty = \sum_\ell P_\ell^\infty\,|\ell\rangle\langle\ell|$, where the sum is done

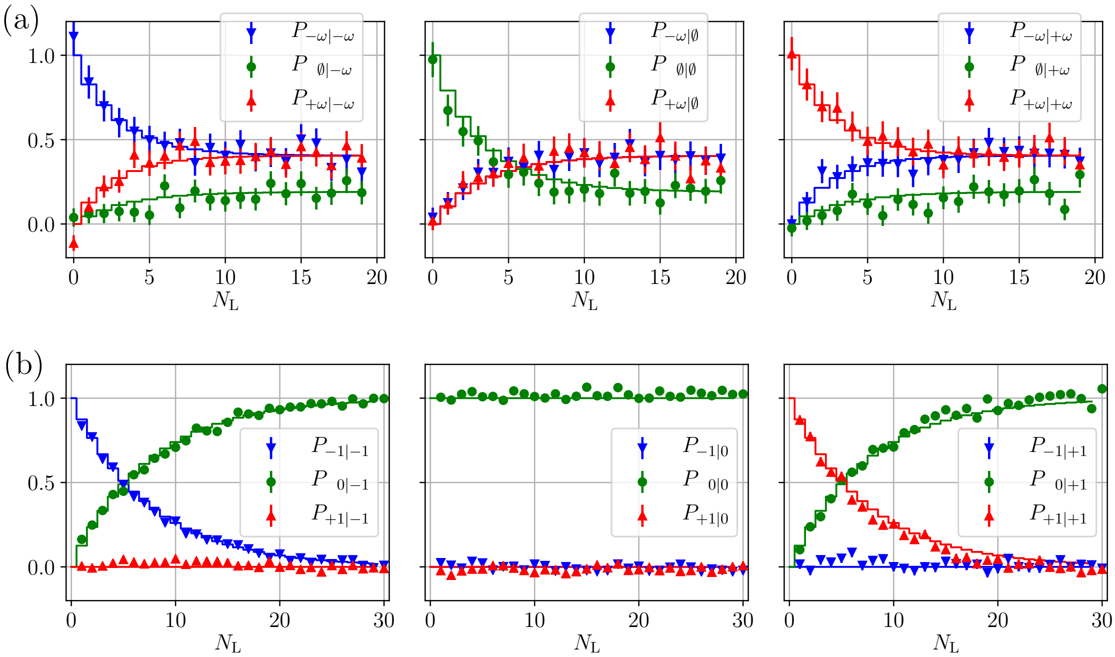

Figure 5.2: Probability of measuring the state $|j\rangle$ after applying the map $\mathcal{M}$ to the state $|i\rangle$ as a function of the number of laser pulses N_L, where $|i\rangle$ and $|j\rangle$ represent each of the eigenstates of the $3LS$ Hamiltonian **(a)** $\mathcal{H}_\mathrm{mw}$ and **(b)** $\mathcal{H}_\mathrm{NV}$. In both cases, the laser pulses duration is $t_\mathrm{L} = 41$ ns, and the time between pulses is $\tau = 424$ ns. Each plot in panels **(a)** and **(b)** shows the three energy jump probabilities for the same initial state. The markers represent the experimental data, with error bars given by the photon shot noise. The solid line represents the simulation of the dynamics (see Sec. 5.3).

over $\ell \in \{+\omega, \emptyset, -\omega\}$, then the diagonal elements of $\mathcal{M}[\rho^\infty]$ after N_L pulses are written as

$$P_m(N_\mathrm{L}) = \sum_\ell P_{m,\ell} = \sum_\ell P_{m|\ell}\, P_\ell^\infty, \tag{5.3}$$

for $m = \pm\omega, \emptyset$. Therefore, by combining the measured conditional probabilities, shown in each panel of Fig. 5.2(b), as indicated by equation (5.3) we can find the correct weight factors $P_{\pm\omega}^\infty, P_\emptyset^\infty$ such that $P_m(N_\mathrm{L})$ is constant regardless of the value of N_L. Operationally, we achieve this by minimizing the sum of square residuals of $\sum_\ell P_{m|\ell}\, P_\ell^\infty$ with respect to its mean value, separately for each m, using as free parameters $P_{\pm\omega}^\infty$, and $P_\emptyset^\infty$. The resulting asymptotic state probabilities, in the case of $\mathcal{H}_\mathrm{mw}$, are [2]

$$\text{(experiment)}\quad P_{\pm\omega}^\infty = (0.39 \pm 0.04),\ \ P_\emptyset^\infty = (0.22 \pm 0.04) \tag{5.4}$$

A more precise estimation of the asymptotic state can be obtained from the simulation of the dynamics. In sec. 5.3, I will show how the dynamics of the system can be modeled by a concatenation of POVMs, and Lindbladian (dissipative) *or* unitary evolution operators, conditional on the POVM result. Using this model, the predicted asymptotic state is defined in terms of the probabilities [3]

$$\text{(simulation)}\quad P_{\pm\omega}^\infty = (0.40469 \pm 0.00003),\ \ P_\emptyset^\infty = (0.19067 \pm 0.00001) \tag{5.5}$$

Having measured the energy jump conditional probabilities is useful not only to estimate the asymptotic state, but also to study the energy variation characteristic function $G(\varepsilon) \equiv \langle e^{-\varepsilon \Delta E}\rangle$. As detailed in sections 3.3.1 and 4.1.1, it is possible to reconstruct $G(\varepsilon)$ using the adapted TPM scheme, i.e., by measuring the energy jump conditional probabilities $P_{j|i}$, and combine the results multiplying them by the probabilities $P_i = \exp(-\beta E_i)/Z$ of a virtual initial thermal state, to be seen as weight factors. In sections 5.4 and 5.5 we will reconstruct the characteristic function with the experimental data, and we will study how to interpret the results with two different fluctuation relations. But before studying the behavior of the characteristic function, in section 5.3 we will describe in detail how to model the dissipative map.

5.3 Model of the dissipative map

In this section I will show a model of the dynamics induced by the stochastic-dissipative map used in the experiment (see Fig. 5.1). The unitary evolution between laser pulses is described by a unitary operator $U \equiv e^{-i\tau\mathcal{H}}$, either for $\mathcal{H} = \mathcal{H}_\mathrm{mw}$ (double driving), or $\mathcal{H} = \mathcal{H}_\mathrm{NV}$ (free evolution). The interaction with the short laser pulses can be modeled as Lindbladian dynamics (representing the optical pumping towards $m_S = 0$) conditioned by the result of a previously applied POVM. In section 5.3.1, I will describe in detail the interaction with a short laser pulse, and I will introduce a superoperator formalism that is very convenient when dealing with Lindbladian dynamics. In section 5.3.2, I will show the complete model of the stochastic-dissipative map.

---

[2] The error bars in Eq. (5.4) result from the error propagation of the experimental data (see Fig. 5.2(a)) during the minimization of the sum of square residuals.

[3] The error bars in Eq. (5.5) represent the confidence interval associated with the minimization operation on the simulated dynamics.

5.3.1 Short laser pulses interaction as POVM and dissipation

As explained in Sec. 1.4, the interaction between the NV center and a green laser pulse can modeled with a master equation that involves the NV center orbital excited and metastable states. For the purposes of the present chapter, i.e., to measure energy variations in a quantum three level system, this interaction is modeled as a POVM followed by dissipation, as described below. In the following description, we ignore the coherent evolution of the system state caused by the Hamiltonian, this is justified by the fact that the Rabi periods associated with the unitary evolution of the system are much longer than the duration of a short laser pulse.

The interaction of the NV spin qutrit with a short laser pulse is modeled as follows: If the laser pulse is not absorbed, the state of the system remains unchanged and there is no dissipation. If the laser pulse is absorbed, the system is subject to a quantum projective measurement in the S_z basis, hence projecting its state into one of the spin states, after which, the system is subject to a dissipation operator, modeled with a Lindbladian master equation. From now on, we will use the Liouville formalism to write operators in their matrix representation (in the S_z basis) such that

$$|-1\rangle\langle-1| = \begin{pmatrix} 0 & 0 & 0 \\ 0 & 0 & 0 \\ 0 & 0 & 1 \end{pmatrix} \; ; \; |0\rangle\langle 0| = \begin{pmatrix} 0 & 0 & 0 \\ 0 & 1 & 0 \\ 0 & 0 & 0 \end{pmatrix} \; ; \; |+1\rangle\langle+1| = \begin{pmatrix} 1 & 0 & 0 \\ 0 & 0 & 0 \\ 0 & 0 & 0 \end{pmatrix}, \tag{5.6}$$

hence we will use indistinguishably the term matrix or operator, unless otherwise specified. In addition, we will use the formalism described in Ref. [175] for superoperators represented as $N^2 \times N^2$ matrices, where $N = 3$ is the dimension of the Hilbert space of the quantum system. A given density matrix ρ_0 after the interaction with a laser pulse of duration t_{L} is transformed into:

$$\mathrm{col}[\rho(t_{\mathrm{L}})] = \sum_{j=1}^{4} \boldsymbol{\mathcal{D}}_j^{(t_{\mathrm{L}})} \boldsymbol{m}_j \,\mathrm{col}[\rho_0] \tag{5.7}$$

where col$[\rho]$ denotes the result of stacking the columns of ρ to form a 'column' vector, $\boldsymbol{m}_j \equiv m_j \otimes m_j$ is one of the measurement super-operator associated with the POVM $\{m_1, m_2, m_3, m_4\}$, where

$$m_1 \equiv \sqrt{p_{\mathrm{abs}}}\, |-1\rangle\langle-1| \tag{5.8}$$

$$m_2 \equiv \sqrt{p_{\mathrm{abs}}}\, |0\rangle\langle 0| \tag{5.9}$$

$$m_3 \equiv \sqrt{p_{\mathrm{abs}}}\, |+1\rangle\langle+1| \tag{5.10}$$

$$m_4 \equiv \sqrt{(1 - p_{\mathrm{abs}})} \mathbb{1}_{3\times3}, \tag{5.11}$$

such that $\sum_{j=1}^{4} m_j m_j^\dagger = \mathbb{1}_{3\times3}$, and $\boldsymbol{\mathcal{D}}_j^{(t_{\mathrm{L}})}$ represents the action of a superoperator conditioned to the result of the POVM:

$$\boldsymbol{\mathcal{D}}_j^{(t_{\mathrm{L}})} = \begin{cases} \mathbb{1}_{9\times9}, & \text{if } j = 4 \\ \boldsymbol{\mathcal{L}}^{(t_{\mathrm{L}})}, & \text{otherwise} \end{cases} \tag{5.12}$$

with

$$\boldsymbol{\mathcal{L}}^{(t_{\mathrm{L}})} \equiv \exp\left(t_{\mathrm{L}} \sum_{\ell=0}^{1} L_\ell^* \otimes L_\ell - \frac{1}{2} \mathbb{1}_{3\times3} \otimes L_\ell^\dagger L_\ell - \frac{1}{2} (L_\ell^\dagger L_\ell)^* \otimes \mathbb{1}_{3\times3} \right) \tag{5.13}$$

where $(\cdot)^*$ denotes complex conjugate, $\otimes$ denotes the Kronecker product, and L_ℓ are the Lindblad jump operators $\{L_0, L_1\} \equiv \{\sqrt{\Gamma}\,|0\rangle\langle+1|\,, \sqrt{\Gamma}\,|0\rangle\langle-1|\}$, which describe the dissipation towards the state $|0\rangle$. The case of $j = 4$ corresponds to the case where the laser pulse is not absorbed, while the other three cases represent the absorption of a laser pulse, involving the Lindbladian dissipation super-operator

$$\boldsymbol{\mathcal{L}}^{(t_\mathrm{L})} = \begin{pmatrix} k & 0 & 0 & 0 & 0 & 0 & 0 & 0 & 0 \\ 0 & \sqrt{k} & 0 & 0 & 0 & 0 & 0 & 0 & 0 \\ 0 & 0 & k & 0 & 0 & 0 & 0 & 0 & 0 \\ 0 & 0 & 0 & \sqrt{k} & 0 & 0 & 0 & 0 & 0 \\ 1-k & 0 & 0 & 0 & 1 & 0 & 0 & 0 & 1-k \\ 0 & 0 & 0 & 0 & 0 & \sqrt{k} & 0 & 0 & 0 \\ 0 & 0 & 0 & 0 & 0 & 0 & k & 0 & 0 \\ 0 & 0 & 0 & 0 & 0 & 0 & 0 & \sqrt{k} & 0 \\ 0 & 0 & 0 & 0 & 0 & 0 & 0 & 0 & k \end{pmatrix} \tag{5.14}$$

where $k \equiv e^{-t_\mathrm{L}\Gamma}$. The product between the effective decay rate and the laser duration Γt_L dictates how strong is the dissipation towards $|0\rangle$. Using short laser pulses with $t_\mathrm{L} = 41$ ns, we characterized the strength of this decay rate resulting in a value such that $\Gamma t_\mathrm{L} \simeq 1/2$. It is important to mention that, given the effective nature of this model, the value of Γ might vary for different NV centers and under different experimental conditions.

Notice that for a long laser pulse ($t_\mathrm{L}\Gamma \gg 1$) any given state ρ would be transformed into $\boldsymbol{\mathcal{L}}^{(t_\mathrm{L})}\,\mathrm{col}[\rho] = \mathrm{col}[|0\rangle\langle 0|]$, being consistent with the usual protocol employed to optically initialize the electronic spin state.

5.3.2 The stochastic-dissipative map

The stochastic-dissipative map $\mathcal{M}$ can be decomposed as a sequence of blocks, each representing a unitary evolution $U \equiv e^{-i\tau\mathcal{H}}$ followed by the interaction of the system with a short laser pulse [Sec. 5.3.1]. In the superoperator formalism [175], the unitary evolution operation applied to a given state ρ is described as $\mathrm{col}[U\rho U^\dagger] = \boldsymbol{U}\,\mathrm{col}[\rho]$, with $\boldsymbol{U} \equiv \exp(-i\tau(\mathcal{H}\otimes \mathbb{1}_{3\times3} - \mathbb{1}_{3\times3}\otimes\mathcal{H}^*))$. Therefore, the superoperator describing a single block of the dynamics corresponds to (see Eq. (5.7))

$$\boldsymbol{\mathcal{B}} \equiv \sum_{j=1}^{4} \boldsymbol{\mathcal{D}}_j^{(t_\mathrm{L})} \boldsymbol{m}_j \boldsymbol{U} \equiv \boldsymbol{\mathcal{A}}\boldsymbol{U}, \tag{5.15}$$

where the superoperator $\boldsymbol{\mathcal{A}}$ represents the mean effect of a single short laser pulse.[4] The overall effect of the dissipative map $\mathcal{M}$, after N_L laser pulses, is then modeled as $\boldsymbol{\mathcal{B}}^{N_\mathrm{L}}$. To grasp a better idea of the effect of dissipative map, in appendix 5.J, the superoperator $\boldsymbol{\mathcal{A}}$ is computed explicitly from the definitions of $\boldsymbol{\mathcal{D}}_j$ and $\boldsymbol{m}_j$.

In the experimental protocol described in Sec. 5.2, the initial state (one of the three Hamiltonian eigenstates) is subject to the dissipative map $\mathcal{M}$, and finally is subject to an energy measurement, modeled with the action of the Hamiltonian eigenstates projectors $\mathcal{P}_i \equiv |E_i\rangle\langle E_i|$. Hence, the energy jump conditional probability to measure E_f in the final energy measurement, after N_L laser pulses, when the initial state is $\mathrm{col}[|E_i\rangle\langle E_i|]$ is given by

$$P_{f|i} = \mathrm{Tr}_{3\times3}[\boldsymbol{\mathcal{P}}_f\, \boldsymbol{\mathcal{B}}^{N_\mathrm{L}}\ \mathrm{col}[|E_i\rangle\langle E_i|]] \tag{5.16}$$

---

[4] From now on, the superindex $^{(t_\mathrm{L})}$ in $\boldsymbol{\mathcal{D}}_j^{(t_\mathrm{L})}$ will be removed to simplify the notation.

where the trace is calculated after performing the inverse operation to create the 'column' vector, i.e., $\mathrm{Tr}_{3\times3}[\mathrm{col}[\cdot]] \equiv \mathrm{Tr}[\cdot]$, and $\boldsymbol{\mathcal{P}}_f \equiv \mathcal{P}_f \otimes \mathcal{P}_f$.[5] Notice that the projectors $\mathcal{P}_i$ are defined by the specific Hamiltonian used during the experimental protocol. The time between laser pulses is fixed, and the dissipation 'strength' was previously characterized to be $e^{-t_{\mathrm{L}}\Gamma} \simeq e^{-1/2}$ [Sec. 5.3.1]. Therefore, the only free parameter in this model is the absorption probability p_{abs}, which is fitted to the experimental data shown in Fig. 5.2. This figure shows as solid lines the predicted dynamics using Eq. (5.16). The fitted absorption probability was $p_{\mathrm{abs}} \simeq 0.3$ (for $\mathcal{H} = \mathcal{H}_{\mathrm{mw}}$) and $p_{\mathrm{abs}} \simeq 0.32$ (for $\mathcal{H} = \mathcal{H}_{\mathrm{NV}}$).

5.4 Generalized Jarzynski-Sagawa-Ueda relation

As mentioned before, the interaction with the laser can be modeled by a POVM and then the application of a dissipation operator, depending on the result of the POVM (see Sec. 5.3.1). Thus, dissipation can be interpreted as an intrinsic feedback process, defined by the properties of the NV center. For this reason, the fluctuations resulting from the evolution under the dissipative map $\mathcal{M}$ are well characterized by a generalized Jarzynski-Sagawa-Ueda (G-JSU) relation

$$\langle e^{-\beta\Delta E}\rangle = \gamma\,, \tag{5.17}$$

where γ is a parameter that defines the effectiveness of the feedback process [144, 179]. The definition of the parameter γ, and the demonstration of equation (5.17) are shown in section 5.4.1. The validity of Eq. (5.17) is experimentally demonstrated with our experimental platform in section 5.4.3. In this regard, notice that the quantum JSU relation was originally proposed for a feedback protocol without dissipation [144]. Here, we developed a variation of the quantum JSU relation that is very similar to the one reported in Ref. [145], where irreversible dynamics are allowed, but in our case for non-thermal dissipative dynamics.

5.4.1 Proof of the G-JSU – theory

In this section I will describe how to calculate the value of the γ, defined for the generalized Jarzynski-Sagawa-Ueda (JSU) relation [Eq. (5.17)], for the qutrit under the stochastic-dissipative map $\mathcal{M}$, and while doing so I will demonstrate the validity of such relation for this kind of dissipative interaction. This proof extends the results shown in Refs. [144, 145] to the case of dissipative dynamics.

Assuming a TPM scheme, the system energy is measured at the beginning of the protocol, then the system evolves under the map $\mathcal{M}$, and finally its energy is measured again. An energy measurement is modeled with the action of the Hamiltonian eigenstates projectors $\mathcal{P}_i \equiv |E_i\rangle\langle E_i|$. In agreement with the superoperator formalism introduced in Sec. 5.3.1, the state after an ideal energy measurement is given by $\mathrm{col}[\mathcal{P}_i\rho\mathcal{P}_i] = \boldsymbol{\mathcal{P}}_i\,\mathrm{col}[\rho]$, with $\boldsymbol{\mathcal{P}}_i \equiv \mathcal{P}_i\otimes\mathcal{P}_i$. For now we will restrict ourselves to the case of a single "block" of the map $\mathcal{M}$ formed by a unitary evolution followed by the interaction with a single short laser pulse. The probability to obtain E_i in the first energy measurement, E_f in the final energy measurement, and to obtain the j-th value in the intermediate POVM, is written as

$$P(f,j,i) = \mathrm{Tr}_{3\times3}[\boldsymbol{\mathcal{P}}_f\,\boldsymbol{\mathcal{D}}_j\boldsymbol{m}_j\,\boldsymbol{U}\,\boldsymbol{\mathcal{P}}_i\;\mathrm{col}[\rho^{\mathrm{th}}]] \qquad (\text{for } N_{\mathrm{L}} = 1) \tag{5.18}$$

---

[5] The probability to measure E_f for a given state ρ is $\mathrm{Tr}[\mathcal{P}_f\rho] = \mathrm{Tr}[\mathcal{P}_f^2\rho] = \mathrm{Tr}[\mathcal{P}_f\rho\mathcal{P}_f] = \mathrm{Tr}_{3\times3}[\boldsymbol{\mathcal{P}}_f\,\mathrm{col}[\rho]]$.

where $\rho^{\rm th}$ is the initial thermal state, $\mathrm{Tr}_{3\times 3}[\mathrm{col}[\cdot]] \equiv \mathrm{Tr}[\cdot]$, and the superoperators $\boldsymbol{U}$, $\boldsymbol{m}_j$ and $\boldsymbol{\mathcal{D}}_j$ are defined in Sec. 5.3. To include more laser pulses separated by unitary evolution periods, we just repeat the block $\boldsymbol{\mathcal{B}}_j \equiv \boldsymbol{\mathcal{D}}_j \boldsymbol{m}_j \boldsymbol{U}$ as many times as the number of short laser pulses. For example, for $N_{\rm L}$ laser pulses, the probability associated with a single trajectory of the system is

$$P(f, j_{N_{\rm L}}, \ldots, j_2, j_1, i) = \mathrm{Tr}_{3\times 3}[\boldsymbol{\mathcal{P}}_f \, \boldsymbol{\mathcal{B}}_{j_{N_{\rm L}}} \cdots \boldsymbol{\mathcal{B}}_{j_2} \boldsymbol{\mathcal{B}}_{j_1} \, \boldsymbol{\mathcal{P}}_i \; \mathrm{col}[\rho^{\rm th}]] \tag{5.19}$$

This means that the left-hand-side of the JSU relation [Eq. (5.17)] can be written as

$$\langle e^{-\beta \Delta E} \rangle = \sum_{i,f=1}^{3} \; \sum_{j_{N_{\rm L}},\ldots,j_1=1}^{4} P(f, j_{N_{\rm L}}, \ldots, j_1, i) e^{-\beta(E_f - E_i)} \tag{5.20}$$

Using the cyclic property of the trace and writing the initial thermal state in its spectral decomposition $\rho^{\rm th} \equiv \sum_{k=1}^{3} \mathcal{P}_k e^{-\beta E_k}/Z$, with $Z \equiv \sum_{k=1}^{3} e^{-\beta E_k}$, it is easy to demonstrate that

$$\langle e^{-\beta \Delta E} \rangle = \gamma \tag{5.21}$$

where

$$\gamma \equiv \sum_{j_{N_{\rm L}},\ldots,j_1=1}^{4} \mathrm{Tr}_{3\times 3}[\boldsymbol{\mathcal{B}}_{j_1}^{\dagger} \boldsymbol{\mathcal{B}}_{j_2}^{\dagger} \cdots \boldsymbol{\mathcal{B}}_{j_{N_{\rm L}}}^{\dagger} \; \mathrm{col}[\rho^{\rm th}]], \tag{5.22}$$

is an equilibrium quantity that can be different from one, and represents the probabilities of applying a 'backwards' protocol starting from the thermal state with the same inverse temperature β. Instead of the formalism used here, this demonstration can also be done using the Kraus operator sum representation instead of the superoperator formalism,[6] in which case the proof is completely analogous to the ones in Refs. [144, 145]. Notice that this proof is trivially generalized for systems of higher dimension, since we have not used any particular property of the single block propagator $\boldsymbol{\mathcal{B}}_j$. Notice also that in our case the Hamiltonian is time invariant, however, for a more general case, the thermal state in Eq. (5.19) (respectively Eq. (5.22)) would represent the thermal state for the Hamiltonian at the time of the initial (respectively final) energy measurement. The 'backwards' block $\boldsymbol{\mathcal{B}}_j^{\dagger} = \boldsymbol{U}^{\dagger} \boldsymbol{m}_j^{\dagger} \boldsymbol{\mathcal{D}}_j^{\dagger}$ can be understood as follows: The superoperator $\boldsymbol{U}^{\dagger}$ corresponds to the time reverse operation of the unitary evolution, the POVM superoperator remains unaltered $\boldsymbol{m}_j^{\dagger} = \boldsymbol{m}_j$, as well as $\boldsymbol{\mathcal{D}}_4^{\dagger} = \boldsymbol{\mathcal{D}}_4$. However, for $j \neq 4$ the superoperator $\boldsymbol{\mathcal{D}}_j^{\dagger} = \boldsymbol{\mathcal{L}}^{\dagger}$ is not trace preserving, which is a clear sign of the non-reversibility process associated with the dissipation [145]. Instead, in the limit case of no dissipation, i.e., a system under stochastically distributed projective measurements, the 'backwards' block represent the inverse time-evolution.

5.4.2 Simplified G-JSU relation for superoperators

Computing the value of γ as written in Eq. (5.22), involves calculating every possible (backwards) trajectory originated by the stochastic-dissipative map $\mathcal{M}$ and specifically by the sequence of measurements. Given the four possible results of each POVM, the number of different trajectories grows exponentially with the number of laser pulses as $4^{N_{\rm L}}$, thus imposing a computational limit on the calculation. However, the superoperator formalism leads to a simplification on this calculation:

---

[6] See appendix 5.I for the Kraus operator sum representation for the Lindbladian dynamics.

using the linear property of the trace, and the distributive property of the matrix product, we can rewrite Eq. (5.22) as:

$$\begin{aligned}\gamma &\equiv \sum_{j_{N_\mathrm{L}},\ldots,j_1=1}^{4} \mathrm{Tr}_{3\times3}[\boldsymbol{\mathcal{B}}^\dagger_{j_1}\boldsymbol{\mathcal{B}}^\dagger_{j_2}\cdots\boldsymbol{\mathcal{B}}^\dagger_{j_{N_\mathrm{L}}}\ \mathrm{col}[\rho^{\mathrm{th}}]] \\ &= \mathrm{Tr}_{3\times3}\left[\left(\sum_{j_1=1}^{4}\boldsymbol{\mathcal{B}}^\dagger_{j_1}\right)\left(\sum_{j_2=1}^{4}\boldsymbol{\mathcal{B}}^\dagger_{j_2}\right)\cdots\left(\sum_{j_{N_\mathrm{L}}=1}^{4}\boldsymbol{\mathcal{B}}^\dagger_{j_{N_\mathrm{L}}}\right)\ \mathrm{col}[\rho^{\mathrm{th}}]\right] \\ &= \mathrm{Tr}_{3\times3}[(\boldsymbol{\mathcal{B}}^\dagger)^{N_\mathrm{L}}\ \mathrm{col}[\rho^{\mathrm{th}}]], \end{aligned} \tag{5.23}$$

where $\boldsymbol{\mathcal{B}} \equiv \sum_{j=1}^{4}\boldsymbol{\mathcal{B}}_j$ (see also Eq. (5.15)) is a superoperator that describes the effect of applying a unitary evolution followed by a single laser pulse, including all the possible results of the POVM and the associated (Lindbladian) dissipation. Using equation (5.23), the complexity on the computation of the value of γ is significantly reduced, with respect to Eq. (5.22).

Notice that it is always possible to find a superoperator associated with the dynamics described by Kraus operators (see equations (1) and (2) in Ref. [175]). Therefore, this simplification on the calculation of γ can be adapted to be valid for any protocol with POVMs and feedback described by completely positive maps.

As a summary, the simplified version of the generalized JSU relation for a quantum system that is subject to intermediate measurements (POVMs) and a feedback process depending on the result of these measurements, is written as [Eqs. (5.17), (5.23), (5.19), and (5.20)]

$$\langle e^{-\beta\Delta E}\rangle = \gamma$$

where

$$\gamma = \mathrm{Tr}_{3\times3}[(\boldsymbol{\mathcal{B}}^\dagger)^{N_\mathrm{L}}\ \mathrm{col}[\rho^{\mathrm{th}}]]$$

$$\langle e^{-\beta\Delta E}\rangle = \sum_{i,f=1}^{3}\mathrm{Tr}_{3\times3}[\boldsymbol{\mathcal{P}}_f\,\boldsymbol{\mathcal{B}}^{N_\mathrm{L}}\,\boldsymbol{\mathcal{P}}_i\,\mathrm{col}[\rho^{\mathrm{th}}]]e^{-\beta(E_f-E_i)}$$

where $\boldsymbol{\mathcal{B}}$ is the superoperator propagator that describes the mean effect of all possible outcomes of the POVM+feedback for each single intermediate measurement.

Analytic expression in the case of $\mathcal{H}_{\mathrm{NV}}$

In the case of a Hamiltonian $\mathcal{H}_{\mathrm{NV}}$, an analytic expression for γ [Eq. (5.23)] can be found. Due to the fact that $\mathcal{H}_{\mathrm{NV}}$ is diagonal in the S_z basis [Eq. (5.1)], then the superoperator $\boldsymbol{U}$ (and $\boldsymbol{U}^\dagger$) has no effect on the spin population, i.e., on the elements in the diagonal of the density matrix describing the state of the system.[7] It only affects the coherence part of the system state. However, in Eq. (5.22) the quantity of interest is the trace of the density operator, so the coherence of the final state is irrelevant, as one could expect from a TPM scheme. Moreover, the effect of the short laser pulses (POVM+dissipation) is to partially destroy the system coherence in the S_z basis. All these considerations are combined to result in

$$\gamma = \mu^{N_\mathrm{L}} + 3(1-\mu^{N_\mathrm{L}})/Z. \tag{5.24}$$

---

[7] We remind that the operators matrix representation is written in terms of the S_z basis.

where $\mu \equiv 1 - (1 - e^{-t_{\rm L}\Gamma})p_{\rm abs}$, and $Z \equiv \sum_{k=-1}^{1} e^{-\beta E_i}$. The mathematical proof of this is given in appendix 5.K. As one would expect, $\gamma = 1$ in the case of $p_{\rm abs} = 0$ (closed system) or in the case of $e^{-t_{\rm L}\Gamma} = 1$ (no dissipation, i.e., no feedback).

Notice that Eq. (5.24) is only valid for a Hamiltonian that is diagonal in the S_z basis. For a Hamiltonian with components along S_x or S_y, the TPM scheme will still be insensitive to the coherence of the final (and initial) state. However, the coherence induced by $\boldsymbol{U}$ will modify the probability of the system to be in each of the S_z eigenstates, which will modify the state of the system after the POVM+dissipation superoperator. In any case, Eq. (5.23) can be used to calculate the value of γ.

5.4.3 Proof of the G-JSU – experiment

As mentioned in Sec. 5.4.1, the parameter γ is defined in terms of non-trace preserving operators. Although it is not possible to independently measure γ, it is possible to calculate γ theoretically, and to compute the values of the characteristic function $G(\beta) = \langle e^{-\beta\Delta E}\rangle$ experimentally, as shown in Fig. 5.3. This completes the experimental demonstration of the validity of Eq. (5.17).

In the case of $\mathcal{H} = \mathcal{H}_{\rm mw}$, the values of γ were calculated with equation (5.23). The inverse temperature of the initial virtual state was $\beta = 3/\omega \simeq 2.54$ MHz^{-1} ($\hbar = 1$).[8] The estimation of the asymptotic state in the case of $\mathcal{H}_{\rm mw}$ is not trivial, but it can be achieved using the experimental data [Eq. (5.4)]. With the correct propagation of error, the experimental data predicts an asymptotic value of $G(\beta)$ shown in Fig. 5.3(a) as a blue shaded area. The asymptotic value of γ is obtained by fitting an exponential decay function to its simulated values (with Eq. (5.23)) for a very large number of pulses ($N_{\rm L} \in [0, 100]$). The result, $\lim_{N_{\rm L}\to\infty} \gamma = 1.18362 \pm 0.00004$, is shown as a red dashed line in Fig. 5.3(a).

The case of $\mathcal{H} = \mathcal{H}_{\rm NV}$ is simpler. The values of γ were calculated using the analytic expression in Eq. (5.24), from which we can also obtain its asymptotic value $\lim_{N_{\rm L}\to\infty} \gamma = 3/Z$, with $Z \equiv \sum_{k=-1}^{1} e^{-\beta E_i}$, shown as a dashed line in Fig. 5.3(b). The value of the inverse temperature of the initial state was set to be $\beta = 0.297/E_{+1} \simeq 0.1$ GHz^{-1} ($\hbar = 1$),[9] with $E_{+1} = \Delta + \gamma_e B \simeq 2.97$ GHz [Sec. 5.1].

The measurement precision in the case of $\mathcal{H}_{\rm NV}$ is higher than the one in the case of $\mathcal{H}_{\rm mw}$. This is related to experimental imperfections of the mw and rf pulses used to realize the electronic and nuclear spin gates (compare also figures 5.2(a) and 5.2(b)). It is worth noting that the majority of values of the characteristic function $G(\beta) = \langle e^{-\beta\Delta E}\rangle$ are different from one, in both cases.

5.5 Fluctuation relation for stationary steady states

In this section, the energy variation characteristic function [Eq. (3.10)] $G(\varepsilon) \equiv \langle \exp(-\varepsilon\Delta E)\rangle$ is analyzed, where ε is an arbitrary scale factor that brings information on the statistical moments of ΔE, and, specifically in this case, on the energetics of an out-of-equilibrium system under dissipation. For values of ε chosen without a specific criterion, $\langle \exp(-\varepsilon\Delta E)\rangle$ is a time-varying quantity, strictly dependent on the choice of the initial state of the system and its parameters. This aspect has been experimentally confirmed also by the computation of the average $\langle \exp(-\beta\Delta E)\rangle$ for

---

[8] This value of β corresponds to an initial spin temperature of approximately 3 μK.

[9] This value of β corresponds to an initial spin temperature of approximately 76 mK.

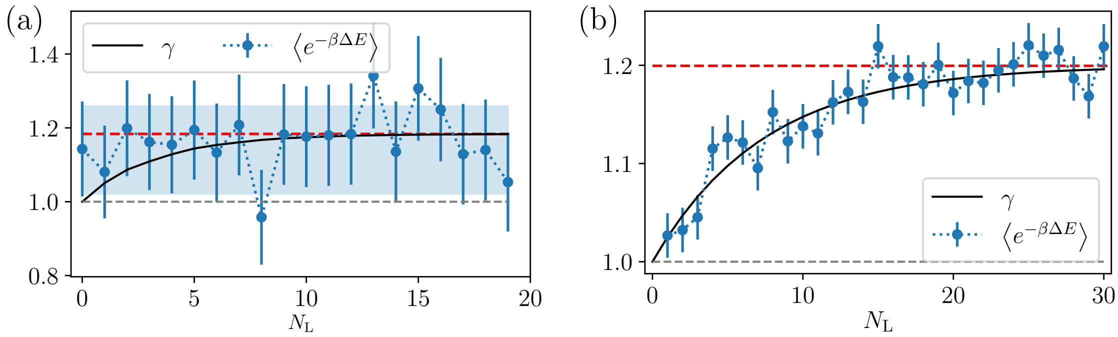

Figure 5.3: Energy variation in terms of the number of laser pulses for a 3LS under the stochastic-dissipative map $\mathcal{M}$ with Hamiltonian **(a)** $\mathcal{H}_{\mathrm{mw}}$ and **(b)** $\mathcal{H}_{\mathrm{NV}}$ respectively. The blue circles represent the measured values of the left-hand-side of the generalized Jarzynski-Sagawa-Ueda relation (5.17), and the continuous black line denotes the theoretical estimation of γ, namely the right-hand-side of the same equation. The asymptotic value of γ is marked by a red dashed line. In **(a)**, the blue area represents the value of $G(\beta)$, with the error propagation, computed for the asymptotic state [Eq. (5.4)]. The value of the inverse temperature of the initial state is **(a)** $\beta = 3/\omega$, and **(b)** $\beta = 0.297/E_{+1}$ ($\hbar = 1$, see text for more details).

the G-JSU fluctuation relation (see Fig. 5.3). In the latter, indeed, γ is a time-dependent function depending on the number of laser pulses applied during the experimental realizations of the protocol. In this regard, we aim to identify the conditions under which $\langle\exp(-\varepsilon\Delta E)\rangle$ could be constant, irrespective of the specific trajectory developed by the system. More specifically, we are seeking for the energy scaling factor ε_c allowing for the equality

$$\langle e^{-\varepsilon_c \Delta E}\rangle = 1 \tag{5.25}$$

irrespective of the initial state and the dimension of the analyzed system. Eq. (5.25) corresponds to the *stationary* regime in which on average the open system does not exchange energy with the external environment, despite the active presence of interaction dynamics (i.e., the quantum system is not closed). In other terms, understanding when $\langle\exp(-\varepsilon\Delta E)\rangle = 1$ lead to the identification of the SSE of the system, whereby the expectation value of the system Hamiltonian is independent of time.

I have theoretically proved (see appendix 5.L) that, for a generic n-dimensional quantum system at the SSE, there exists one finite single time-independent ε_c such that $\langle\exp(-\varepsilon_c\Delta E)\rangle = 1$. This steady state is originated by the action of a dissipative channel, bringing the system into a density operator with constant energy in time that does not depend on the initial state. After the energy measurement at the end of the protocol, the quantum system is in a mixed state that in general is *not* thermal. This means that the effects of the dissipative channel on the analyzed 3LS may *not* be modeled by the effective interaction of the system with a thermal reservoir. Meaning that this interaction is not compatible with the XFR for a system under thermalizing dynamics [167] (see Eq. (3.4)). However, also in this general non-thermal dissipative dynamics, the validity of Eq. (5.25) is ensured and, specifically, related to the existence of a *unique constant finite* value of ε_c depending on the populations of the density matrix of both the initial state and the steady state.

The unique constant value of ε_c can be determined by numerically solving an algebraic equation (see appendix 5.L.1). The data in Fig. 5.4 constitutes the exper-

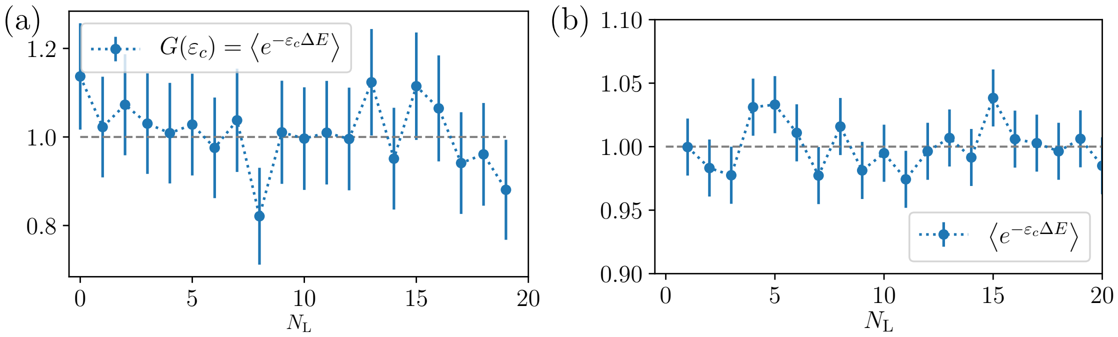

Figure 5.4: Energy variation in terms of the number of laser pulses for a 3LS under the stochastic-dissipative map $\mathcal{M}$ with Hamiltonians **(a)** $\mathcal{H}_\mathrm{mw}$ and **(b)** $\mathcal{H}_\mathrm{NV}$ respectively. The blue circles represent represent the measured values of the LHS of Eq. (5.25). The grey horizontal dashed line, at vertical axis equal to one, is a guide for the eye. **(a)** $\varepsilon_c \simeq 2.814/\omega$ and $\beta = 3/\omega$ ($\hbar = 1$). **(b)** In this particular case, the only value of ε for which $G(\varepsilon) = 1$ is $\varepsilon = 0$, hence $\varepsilon_c = 0$. This means that the data represents the sum of all the energy variation joint probabilities.

imental verification of Eq. (5.25). In this regard, it is worth noting that Eq. (5.25) is valid for any value of N_L, as we experimentally verified, which suggests that the dissipation process must fulfill some sort of generalized detailed balance condition. However, in contrast with the case of the two level system (see Sec. 4.2.3), the dissipation cannot be directly connected with a pseudo-thermalizing process, because the asymptotic state cannot be written as an effective thermal state. It is worth mentioning that, in theory, in the limit where the asymptotic SSE can be written as a pseudo-thermal state, with inverse pseudo-temperature β_∞, the fluctuation relation for thermalizing dynamics [167], $\langle \exp(-\Delta\beta\Delta E) \rangle = 1$ would be recovered, where $\Delta\beta \equiv \beta - \beta_\infty$.

5.5.1 FRs as witness of non-unitality

The value of the parameters γ or ε_c, can be used as *witnesses of non-unitality*. A map describing the dynamics of a system is considered to be unital if and only if the identity is a fixed point of the map. Given the dissipative nature of the dynamics, the asymptotic state is independent of the initial state. Hence, unital dissipative dynamics implies that the asymptotic density operator is proportional to the identity, which implies that $\langle e^{-\beta\Delta E} \rangle = 1$ (see corollary in appendix 5.L). The contrapositive of the statement reads: If $\langle e^{-\beta\Delta E} \rangle \neq 1$, then the dissipative map $\mathcal{M}$ is non-unital. Therefore, *either the value of* $\gamma \neq 1$ *or* $\varepsilon_c \neq \beta$ *directly implies non-unital dynamics*. The inverse is not necessarily true in general. This is consistent with the findings made by other studies [145, 181].

5.6 Conclusions

In this chapter we have studied the short and long time dynamics of a quantum three level system (3LS) that asymptotically approaches a non-Gibbsian state, namely a non-thermal mixed state. The analyzed quantum system, formed by the ground state of an NV center in diamond at room temperature, is coherently driven by a time-independent Hamiltonian and is subject to dissipation – an irreversible process

– originated by the interaction with short laser pulses. The asymptotic non-Gibbsian state entailed by dissipation is independent of the initial state, but depends on the specific Hamiltonian that defines the continuous driving of the system. Since the dissipation operator is diagonal in the S_z basis, the fixed point of the map depends on whether or not such Hamiltonian commutes with S_z.

The non-thermalizing dynamics of the system falls under the category of open quantum system dynamics, which we analyzed within the quantum thermodynamics framework. In particular, we used quantum fluctuation relations (FR) to understand and describe how the system achieves the asymptotic state that is stationary if evaluated along the energy basis of the system. For this reason the acronym SSE, steady state in the energy basis, has been introduced. Exploiting the POVM formalism to describe the qutrit interaction with the short laser pulses, we have demonstrated that intermittent stochastic dissipation can be modeled as an intrinsic feedback process. This suggested us the use of a generalized Jarzynski-Sagawa-Ueda (JSU) relation to derive the statistics of the system energy variation. In this regard, the comparison between experimental data and theory leads us to conclude that a generalized JSU relation, involving Lindbladian operators, is suitable for dissipative non-thermal irreversible dynamics.

In addition, using a superoperator formalism, we found a simplified version of the JSU relation, for which the value of the parameter γ can be easily computed [Eq. (5.23)], without requiring to operate with all possible trajectories of the system. This simplification should be valid for any protocol involving measurements and feedback, as long as the evolution between measurements is given by a completely positive map. The importance of this result is that it permits a fast computation of γ even for a large number of intermediate measurements, which was impractical before due to the fact that the number of different trajectories increases exponentially with the number of intermediate measurements.

We have also used a second FR based on the identification of an energy scale factor ε_c such that the average exponentiated negative energy variation $\langle e^{-\varepsilon_c \Delta E} \rangle$ is always equal to one for any value of time. In the case of an asymptotic non-Gibbsian state, the energy scale factor ε_c is not an inverse temperature but a parameter that characterizes the dissipative map, solely depending on the initial and asymptotic states of the system.

Our results pave the way for the use of NV centers in diamond for the study of quantum systems interacting with reservoirs in non-equilibrium states [182–184], where quantum correlations may affect the total amount of quantum-heat during the interaction processes.

5.G Appendix: Nitrogen nuclear spin initialization

The electronic spin of the NV center is intrinsically coupled to the nuclear spin of the nitrogen atom. The NV center we work with is coupled to a ^{14}N atom with nuclear spin $I = 1$. For that reason each of the electronic spin levels is split into three hyperfine sublevels for the nuclear spin projections $m_I = 0, \pm 1$. In order to obtain a genuine three-level system of the electronic spin, we polarize the nuclear spin in the $m_I = -1$ projection. This is done with a sequence of selective microwave and radio-frequency π-pulses, as illustrated schematically in figure 5.5. We assume to have as initial state a completely mixed state involving the nine hyperfine sublevels, although this polarizing protocol is adequate for any initial state. The NV center electronic spin is initialized into the $m_S = 0$ state by means of a long laser pulse. The external magnetic field is far away from the excited-state level anti-crossing (ESLAC) [Sec. 1.5], hence the nuclear spin is unaffected by the interaction with laser pulses. From now on we adopt the notation $|m_S, m_I\rangle$ to describe a state of the joint system. In the first step, the population of $|0,1\rangle$ is transferred to $|1,1\rangle$ by a controlled-NOT operation on the electronic spin (selective mw π-pulse) and subsequently transferred to $|1,0\rangle$ by a controlled-NOT operation on the nuclear spin (selective RF π-pulse). Then a long laser pulse pumps the population to $|0,0\rangle$ while leaving unchanged the population that was already in the $m_S = 0$ level. Analogously, in a second step the resulting population in $|0,0\rangle$ is transferred to $|0,-1\rangle$ passing through $|1,0\rangle$ and $|1,-1\rangle$. Among the possibilities of initializing a different m_I using different controlled-NOT operations, we have chosen the described one as it gave the best polarization result. We have achieved an initialization fidelity of 79%, measured with a standard electron spin resonance (ESR) experiment, figure 5.6. This imperfect nuclear spin polarization is taken into account when normalizing the photoluminescence intensity in the main experiments of this chapter.

5.H Appendix: Hamiltonian eigenstate preparation and final readout gates

As shown in Fig. 5.1, the preparation of the Hamiltonian initial eigenstate requires the application of the quantum gate $G_i : |0\rangle \rightarrow |i\rangle$, while the readout of the proba-

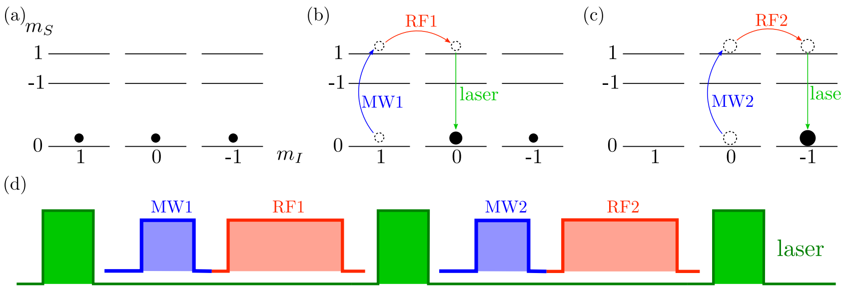

Figure 5.5: **Scheme for nuclear spin initialization of the ^{14}N nucleus. (a)** Initially the population is distributed among the $m_I = 0, \pm 1$. **(b, c)** With selective mw and RF pulses the population is first transferred from $m_I = +1$ to $m_I = 0$ and then to $m_I = -1$ to initialize/polarize the nuclear spin. The laser is used to pump population in $m_S = 1$ back to $m_S = 0$.

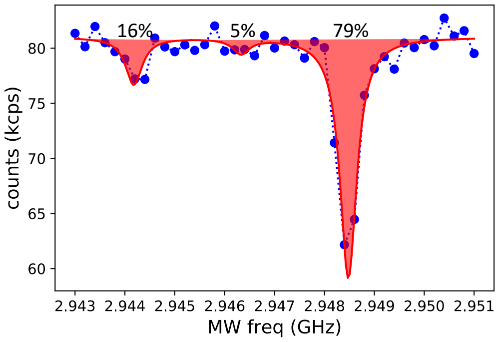

Figure 5.6: **Nitrogen nuclear spin polarization**. Results from an electron spin resonance (ESR) experiment performed immediately after the nuclear spin polarization protocol.

bility that the system is in the eigenstate $|j\rangle$ requires a second quantum gate, i.e., $G_j^{-1} : |j\rangle \to |0\rangle$. In this section we describe these gates for each of the possible states $|i\rangle$ and $|j\rangle$.

There are two possibilities for preparing the Hamiltonian eigenstates. One is with a double-driving microwave (mw) gate driving transitions between $|0\rangle$ and $|\pm 1\rangle$, and the other is with two mw pulses applied subsequently to transfer parts of the population from $|0\rangle$ to $|-1\rangle$ and $|+1\rangle$ separately. In our experimental setup we have opted for the latter method due to easier handling of the mw operations. To induce the transition $|0\rangle \to |\emptyset\rangle \equiv \frac{1}{\sqrt{2}}(|-1\rangle - |+1\rangle)$, the population in $|0\rangle$ has to be transferred in equal parts to $|\pm 1\rangle$ where both parts have an opposite phase. This is achieved by applying a $\pi/2$-pulse that transfers half of the population to $|-1\rangle$, and subsequently applying a π-pulse to transfer the remaining population in $|0\rangle$ to $|+1\rangle$. To obtain the correct phase between the $|\pm 1\rangle$, it is required that the phase of both pulses is $\pi/2$ (or $-\pi/2$), as one can verify by calculation. Also the preparation of $|\pm\omega\rangle \equiv \frac{1}{2}\left(|-1\rangle \pm \sqrt{2}\,|0\rangle + |+1\rangle\right)$ works in a very similar way. A $\pi/3$-pulse has to be applied to transfer one quarter of the population to $|-1\rangle$ and, then, an $\arccos(1/3)$-pulse transfers another one quarter of population from $|0\rangle$ to $|+1\rangle$. Calculation shows that the phases of the mws have to be $\mp\pi/2$ and $\pm\pi/2$, respectively for the first and second mw, if we aim to prepare $|\pm\omega\rangle$.

The second quantum gate G_j^{-1} applies the reversed process with respect to the preparation one. Thus G_j^{-1} is obtained by performing the operations of the state preparation in reversed order and assigning to the implemented mw pulses an opposite phase.

5.I Appendix: Kraus operators associated with dissipation

As explained in Sec. 5.3.1, the master equation that describes the absorption of a single laser pulse can be recast into a Lindbladian superoperator $\boldsymbol{\mathcal{L}}$ (see Eq. (5.14)). Given the fact that $\boldsymbol{\mathcal{L}}$ describes a completely positive map, it is possible to find a set of Kraus operators associated with the system's dynamics. Finding the Kraus operators is not always trivial task, however, a simple recipe can be found in Ref. [175] to go from Lindbladian superoperators to Kraus sum representation, and vice versa. The idea is to find the eigenvalues v_m and eigenvectors V_n of the *Choi* matrix associated with $\boldsymbol{\mathcal{L}}$. The Kraus operators are then expressed as $A_n = \sqrt{v_n}\,\mathrm{col}^{-1}(V_n)^\intercal$, where col^{-1} is the opposite operation of column stacking, i.e., it converts the N^2-length vector into an $N \times N$ matrix. More details about this procedure can be found in Ref. [175]. In the present case, the corresponding Kraus operators are:

$$\begin{aligned}
A_0 &= \mathbb{1}_{3\times 3} - \left(1 - \sqrt{e^{-t_\mathrm{L}\Gamma}}\right) S_z^2 \\
A_1 &= \sqrt{1 - e^{-t_\mathrm{L}\Gamma}}\, |0\rangle\!\langle -1| \\
A_2 &= \sqrt{1 - e^{-t_\mathrm{L}\Gamma}}\, |0\rangle\!\langle +1|\,.
\end{aligned} \tag{5.26}$$

Note: The theory used throughout this chapter was based on the superoperator formalism. Finding the set of Kraus operators that generate the same dynamics as the Lindbladian superoperator $\boldsymbol{\mathcal{L}}$ was done only as an exercise, and to offer to the reader the possibility of using this alternative formalism.

5.J Appendix: Mean effect of laser pulses

As explained in section 5.3.1 and 5.3.2, the effect of applying a single laser pulse is described by the superoperator

$$\boldsymbol{\mathcal{A}} \equiv \sum_{j=1}^{4} \boldsymbol{\mathcal{D}}_j \boldsymbol{m}_j \tag{5.27}$$

This superoperator can be computed explicitly from the definitions of $\boldsymbol{\mathcal{D}}_j$ and $\boldsymbol{m}_j$ [Sec. 5.3.1]. Introducing the auxiliary matrices

$$\boldsymbol{A}_1 \equiv \begin{pmatrix}
1&0&0&0&0&0&0&0&0\\
0&0&0&0&0&0&0&0&0\\
0&0&0&0&0&0&0&0&0\\
0&0&0&0&0&0&0&0&0\\
0&0&0&0&1&0&0&0&0\\
0&0&0&0&0&0&0&0&0\\
0&0&0&0&0&0&0&0&0\\
0&0&0&0&0&0&0&0&0\\
0&0&0&0&0&0&0&0&1
\end{pmatrix} ; \quad
\boldsymbol{A}_2 \equiv \begin{pmatrix}
0&0&0&0&0&0&0&0&0\\
0&0&0&0&0&0&0&0&0\\
0&0&0&0&0&0&0&0&0\\
0&0&0&0&0&0&0&0&0\\
1&0&0&0&1&0&0&0&1\\
0&0&0&0&0&0&0&0&0\\
0&0&0&0&0&0&0&0&0\\
0&0&0&0&0&0&0&0&0\\
0&0&0&0&0&0&0&0&0
\end{pmatrix} ; \quad
\boldsymbol{A}_3 \equiv \mathbb{1}_{9\times 9} - \boldsymbol{A}_1,$$

then

$$\boldsymbol{\mathcal{A}} = \mu \boldsymbol{A}_1 + (1-\mu)\boldsymbol{A}_2 + \boldsymbol{A}_3(1 - p_\mathrm{abs}), \tag{5.28}$$

$$\text{where } \; \mu \equiv 1 - (1 - e^{-t_\mathrm{L}\Gamma})p_\mathrm{abs}. \tag{5.29}$$

It is no surprising that, if $p_\mathrm{abs} = 0$ then $\boldsymbol{\mathcal{A}}_{(p_\mathrm{abs}=0)} = \mathbb{1}_{9\times 9}$. On the other hand, if $p_\mathrm{abs} = 1$ then the POVM is actually a quantum projective measurement (QPM) in the S_z basis, which is why $\boldsymbol{\mathcal{A}}_{(p_\mathrm{abs}=1)} = e^{-t_\mathrm{L}\Gamma}\boldsymbol{A}_1 + (1 - e^{-t_\mathrm{L}\Gamma})\boldsymbol{A}_2$ is almost equal to the Lindbladian dissipation super-operator $\boldsymbol{\mathcal{L}}$ [Eq. (5.14)], but without the terms involving coherences, a signature of the QPM. Another special case occurs when $e^{-t_\mathrm{L}\Gamma} = 1$, meaning the case without dissipation, where equation (5.28) is rewritten as $\boldsymbol{\mathcal{A}} = \boldsymbol{A}_1 p_\mathrm{abs} + \mathbb{1}_{9\times 9}(1 - p_\mathrm{abs})$, which represents the mean effect of applying a QPM of S_z with a probability p_abs.

Writing $\boldsymbol{\mathcal{A}}$ as in Eq. (5.28) is very useful, because the following properties

$$\begin{aligned}
\boldsymbol{A}_i^2 &= \boldsymbol{A}_i\,, \quad \text{for } i \in \{1,2,3\} \\
\boldsymbol{A}_1\boldsymbol{A}_3 = \boldsymbol{A}_3\boldsymbol{A}_1 &= \boldsymbol{A}_2\boldsymbol{A}_3 = \boldsymbol{A}_3\boldsymbol{A}_2 = \mathbb{0}_{9\times 9} \\
\boldsymbol{A}_1\boldsymbol{A}_2 &= \boldsymbol{A}_2\boldsymbol{A}_1 = \boldsymbol{A}_2
\end{aligned}$$

imply that

$$\boldsymbol{\mathcal{A}}^{N_{\mathrm{L}}} = \mu^{N_{\mathrm{L}}}\boldsymbol{A}_1 + (1-\mu^{N_{\mathrm{L}}})\boldsymbol{A}_2 + \boldsymbol{A}_3(1-p_{\mathrm{abs}})^{N_{\mathrm{L}}}, \tag{5.30}$$

which describes the effect of applying N_{L} short laser pulses one after each other. Notice that (excepting the special cases mentioned before), $\lim_{N_{\mathrm{L}}\to\infty}\mu^{N_{\mathrm{L}}} = 0$, meaning that $\lim_{N_{\mathrm{L}}\to\infty}\boldsymbol{\mathcal{A}}^{N_{\mathrm{L}}} = \boldsymbol{A}_2$, which is the superoperator that 'pumps' any state into the $m_S = 0$ state, i.e., the NV spin is optically initialized.

5.K Appendix: Parameter γ in the case of $\mathcal{H}_{\mathrm{NV}}$

In this appendix we demonstrate Eq. (5.24). In the particular case of $\mathcal{H} = \mathcal{H}_{\mathrm{NV}}$, the unitary superoperator is written as

$$\begin{aligned}\boldsymbol{U}(\tau) &\equiv \exp(-i\tau(\mathcal{H}\otimes\mathbb{1}_{3\times3} - \mathbb{1}_{3\times3}\otimes\mathcal{H}))\\ &= \begin{pmatrix} 1 & 0 & 0 & 0 & 0 & 0 & 0 & 0 & 0\\ 0 & e_+ & 0 & 0 & 0 & 0 & 0 & 0 & 0\\ 0 & 0 & \frac{e_+}{e_-} & 0 & 0 & 0 & 0 & 0 & 0\\ 0 & 0 & 0 & \frac{1}{e_+} & 0 & 0 & 0 & 0 & 0\\ 0 & 0 & 0 & 0 & 1 & 0 & 0 & 0 & 0\\ 0 & 0 & 0 & 0 & 0 & \frac{1}{e_-} & 0 & 0 & 0\\ 0 & 0 & 0 & 0 & 0 & 0 & \frac{e_-}{e_+} & 0 & 0\\ 0 & 0 & 0 & 0 & 0 & 0 & 0 & e_- & 0\\ 0 & 0 & 0 & 0 & 0 & 0 & 0 & 0 & 1 \end{pmatrix}\end{aligned} \tag{5.31}$$

where $e_\pm \equiv e^{-i\tau E_{\pm1}}$. Hence, using equations (5.15) and (5.28), we can write $\boldsymbol{\mathcal{B}} = \mu\boldsymbol{A}_1 + (1-\mu)\boldsymbol{A}_2 + \boldsymbol{U}_1(\tau)(1-p_{\mathrm{abs}})$, where

$$\boldsymbol{U}_1(\tau) \equiv \boldsymbol{U}(\tau) - \boldsymbol{A}_1. \tag{5.32}$$

Notice that $(\boldsymbol{U}_1(\tau))^n = \boldsymbol{U}_1(n\tau)$, and $\boldsymbol{A}_i\boldsymbol{U}_1(\tau) = \boldsymbol{U}_1(\tau)\boldsymbol{A}_i = \boldsymbol{A}_i$, for $i\in\{1,2\}$. In analogy to the case of $\boldsymbol{\mathcal{A}}$ presented in appendix 5.J, we can therefore obtain

$$\boldsymbol{\mathcal{B}}^{N_{\mathrm{L}}} = \mu^{N_{\mathrm{L}}}\boldsymbol{A}_1 + (1-\mu^{N_{\mathrm{L}}})\boldsymbol{A}_2 + \boldsymbol{U}_1(N_{\mathrm{L}}\tau)(1-p_{\mathrm{abs}}). \tag{5.33}$$

Since $\mathcal{H} = \mathcal{H}_{\mathrm{NV}}$, then a thermal state is written as

$$\mathrm{col}(\rho^{\mathrm{th}}) = \frac{1}{Z}\,\mathrm{col}\left(\begin{bmatrix} e^{-\beta E_{+1}} & 0 & 0\\ 0 & 1 & 0\\ 0 & 0 & e^{-\beta E_{-1}}\end{bmatrix}\right) = \frac{1}{Z}\begin{pmatrix} e^{-\beta E_{+1}}\\ 0\\ 0\\ 0\\ 1\\ 0\\ 0\\ 0\\ e^{-\beta E_{-1}}\end{pmatrix}, \tag{5.34}$$

with $Z \equiv \sum_{k=-1}^{1} e^{-\beta E_i}$. Finally, using the fact that $\boldsymbol{A}_1^\dagger\,\mathrm{col}(\rho^{\mathrm{th}}) = (\boldsymbol{U}_1(N_{\mathrm{L}}\tau))^\dagger\,\mathrm{col}(\rho^{\mathrm{th}}) = \mathrm{col}(\rho^{\mathrm{th}})$, and $\boldsymbol{A}_2^\dagger\,\mathrm{col}(\rho^{\mathrm{th}}) = \mathrm{col}(\mathbb{1}_{3\times3})/Z$, we can combine Eq. (5.33) together with Eq. (5.23) and obtain:

$$\gamma = \mu^{N_{\mathrm{L}}} + 3(1-\mu^{N_{\mathrm{L}}})/Z. \tag{5.35}$$

Q.E.D.

5.L Appendix: Energy steady state regime enabling fluctuation relations

In this appendix we demonstrate that the existence of a stationary state in the energy basis SSE for map applied to an arbitrary (discrete-variable) quantum system implies the existence of a unique finite and time-independent value of ε obeying the fluctuation relation $G(\varepsilon) \equiv \langle \exp(-\varepsilon \Delta E) \rangle = 1$.

The proof (sketched below) is based on demonstrating that, under the hypothesis of the existence of a stationary state in the energy basis for large times, (i) for a generic open quantum system the function $\langle \exp(-\varepsilon \Delta E) \rangle$ is always convex with respect to the energy scale ε, and (ii) for any dissipative quantum dynamics, the steady state regime implies that the unique finite zero of $G(\varepsilon) - 1$ only depends on the initial state and the stationary one.

As a first step, let us show the convexity of $G(\varepsilon) = \sum_{i,j} P_{j|i} P_i e^{-\varepsilon \Delta E_{i,j}}$ where $\Delta E_{i,j} \equiv E_j - E_i$, P_i denotes the probability of measuring E_i at the beginning of the TPM protocol, $P_{j|i}$ is the conditional probability of measuring E_j at the end of the protocol, and the sum $\sum_{i,j}$ is performed over all the possible initial i and final j measured energies. These probabilities are defined by the probability distribution $P_{\Delta E}$ as obtained by applying the two-point measurement protocol. $G(\varepsilon)$ is a twice differentiable real-valued function with positive concavity. Indeed,

$$\frac{\partial^2 G(\varepsilon)}{\partial \varepsilon^2} = \sum_{i,j} P_{j|i} P_i e^{-\varepsilon (E_j - E_i)} (E_j - E_i)^2 \tag{5.36}$$

is always equal or larger than zero. Said this, we need to verify the validity of the following two conditions: (i) $\varepsilon = 0$ is a zero of $g(\varepsilon) \equiv G(\varepsilon) - 1 = 0$; (ii) the minimum value of $g(\varepsilon)$ is equal or smaller than zero. If both these conditions hold, being $G(\varepsilon)$ and $g(\varepsilon)$ functions with positive concavity, then $g(\varepsilon)$ has only another zero $\varepsilon \neq 0$. Condition (i) is straightforwardly verified, since $\varepsilon = 0$ is the trivial solution of the fluctuation relation $G(\varepsilon) = 1$. Instead, to verify the validity of condition (ii), we just need to check if the derivative $\partial g(\varepsilon)/\partial \varepsilon$ evaluated in $\varepsilon = 0$ is different from zero for all system parameters, except for special cases. One has that

$$\left. \frac{\partial g(\varepsilon)}{\partial \varepsilon} \right|_{\varepsilon = 0} = -\langle E_\infty \rangle + \langle E_{\rm in} \rangle, \tag{5.37}$$

which is zero if and only if $\langle E_\infty \rangle = \langle E_{\rm in} \rangle$, namely the initial and final mean energy values are the same. This happens when the effects of the presence of the dissipative channel are negligible, e.g., when the steady state reached by the system is thermal with the same temperature than the initial thermal state, i.e., $\beta_\infty = \beta$. We have thus proven that $G(\varepsilon)$ is a convex function, and its minimum value is necessarily equal or smaller than 1. These properties imply the existence of a unique value of ε different from zero and obeying the fluctuation relation $G(\varepsilon) = 1$.

As a second step, we assume that the quantum system is at the steady state. The energy steady state is attained when the current state of the system, solution of the dynamical equation of motion, has constant energy and does not depend on the initial state. This condition can be translated in a property of $\langle \exp(-\varepsilon \Delta E) \rangle$. In the SSE, the conditional probabilities $P_{j|i}$ are invariant with respect to the initially measured energy value, with the result that

$$P_{j|1} = P_{j|2} = \ldots = P_{j|n} \equiv \widetilde{P}_j \tag{5.38}$$

for any j, with n dimension of the quantum system. By assuming the validity of Eq. (5.38), we can decompose $\langle\exp(-\varepsilon\Delta E)\rangle$ as

$$\langle\exp(-\varepsilon\Delta E)\rangle = \left(\sum_i P_i e^{\varepsilon E_i}\right)\left(\sum_j \widetilde{P}_j e^{-\varepsilon E_j}\right) \tag{5.39}$$

that is still a convex function with respect to ε. Thus, there exists a unique value of ε different from zero that verifies the equality $\langle\exp(-\varepsilon\Delta E)\rangle = 1$. From the decomposition of Eq. (5.39), one can state that ε depends only on the set of probabilities $\{P_i\}$ and $\{\widetilde{P}_j\}$, corresponding to the initial and the stationary states.

Corollary: If the dissipation is such that the asymptotic state is a completely mixed state, then $\varepsilon = \beta$ is the non trivial solution of $g(\varepsilon) = 0$. This can be easily proven by making the substitution $\varepsilon = \beta$ and $\widetilde{P}_j = 1/3$ in Eq. (5.39).

5.L.1 An algebraic recipe to get ε with experimental data

Let us consider a 3LS initialized in the thermal state $\rho_0 \equiv \exp(-\beta_{\rm in}\mathcal{H})/Z_{\beta_{\rm in}}$ with $Z_{\beta_{\rm in}} = {\rm Tr}[\exp(-\beta_{\rm in}\mathcal{H})]$. By diagonalizing the system Hamiltonian as $\mathcal{H} = \sum_i E_i|E_i\rangle\langle E_i|$, the thermal initial state equals to

$$\rho_0 = \sum_i \frac{e^{-\beta_{\rm in}E_i}}{Z_{\beta_{\rm in}}}|E_i\rangle\langle E_i| = \sum_i P_i|E_i\rangle\langle E_i|$$

with $P_i \equiv \exp(-\beta_{\rm in}E_i)/Z_{\beta_{\rm in}}$. Then, let us introduce the mean value of the exponentiated energy variation ΔE, i.e.,

$$\langle\exp(-\varepsilon\Delta E)\rangle = \sum_{i,j} P_i P_{j|i} e^{-\varepsilon(E_j-E_i)}$$

depending on the energy scaling factor ε. Note that the average $\langle\exp(-\varepsilon\Delta E)\rangle$ is defined by the sets $\{P_i\}$ and $\{P_{j|i}\}$, corresponding respectively to the probabilities to measure the initial energies of the system and the conditional probabilities to get E_j at the end of the procedure having already measured E_i.

In the SSE regime, the conditional probabilities $P_{j|i}$ does not depend in the initially measured energies E_i. This entails that $P_{j|1} = P_{j|2} = P_{j|3} \equiv \widetilde{P}_j$ for any j such that

$$\langle\exp(-\varepsilon\Delta E)\rangle = \sum_{i,j} P_i \widetilde{P}_j e^{-\varepsilon(E_j-E_i)} \tag{5.40}$$

whereby the quantum state $\rho_{\rm fin}$ after the application of the 2nd energy projective measurement of the measurement protocol (here, the TPM scheme) is a mixed state, not necessarily thermal but completely described by the probabilities $\widetilde{P}_j$:

$$\rho_{\rm fin} = \sum_j \widetilde{P}_j|E_j\rangle\langle E_j|.$$

Case 1: $\mathcal{H}_{\rm NV}$

In this case, the asymptotic state is $|0\rangle\langle 0|$, hence $\widetilde{P}_{\pm 1} = 0$ and $\widetilde{P}_0 = 1$. This means that equation (5.40) is written as $\langle\exp(-\varepsilon\Delta E)\rangle = \sum_i e^{\varepsilon E_i}e^{-\beta_{\rm in}E_i}/Z_{\beta_{\rm in}}$. Assuming that $\langle\exp(-\varepsilon\Delta E)\rangle = 1$, then $Z_{\beta_{\rm in}} = \sum_i e^{-(\beta_{\rm in}-\varepsilon)E_i}$. This last equality can be rearranged into

$$0 = e^{-\beta_{\rm in}E_{-1}}(e^{\varepsilon E_{-1}} - 1) + e^{-\beta_{\rm in}E_{+1}}(e^{\varepsilon E_{+1}} - 1). \tag{5.41}$$

The only possible solution of this equation is $\varepsilon = 0$, for the following reason: We know that $E_{+1} > 0$ and $E_{-1} > 0$. If $\varepsilon > 0$ then both terms in Eq. (5.41) are positive and cannot sum zero. Similarly, if $\varepsilon < 0$ then both terms in Eq. (5.41) are negative and cannot sum up to zero. Therefore, in the case of $\mathcal{H}_{\rm NV}$, the only solution of $G(\varepsilon) = 1$ is the trivial one, $\varepsilon = 0$.

Case 2: $\mathcal{H}_{\rm mw}$

The asymptotic state in this case is not as simple as in the previous case. For this reason, it is convenient to decompose each probability $\widetilde{P}_j$ as the product of two contributions: one is thermal and is associated to an inverse temperature $\beta_{\rm fin}$, while the other is a correction term that accounts for the (geometric) distance λ concerning $\rho_{\rm fin}$ from being thermal [180]. Specifically, given the set $\{E_j\}$ of the system energies after the application of the measurement protocol, $\widetilde{P}_j$ can be written as

$$\widetilde{P}_1 = \frac{e^{-\beta_{\rm fin}E_1}e^{\lambda(E_2-E_3)^2}}{Z_{\beta_{\rm fin}}(\lambda)}; \quad \widetilde{P}_2 = \frac{e^{-\beta_{\rm fin}E_2}e^{\lambda(E_3-E_1)^2}}{Z_{\beta_{\rm fin}}(\lambda)}; \quad \widetilde{P}_3 = \frac{e^{-\beta_{\rm fin}E_3}e^{\lambda(E_1-E_2)^2}}{Z_{\beta_{\rm fin}}(\lambda)}, \tag{5.42}$$

where $Z_{\beta_{\rm fin}}(\lambda) = e^{-\beta_{\rm fin}E_1}e^{\lambda(E_2-E_3)^2} + e^{-\beta_{\rm fin}E_2}e^{\lambda(E_3-E_1)^2} + e^{-\beta_{\rm fin}E_3}e^{\lambda(E_1-E_2)^2}$, denotes the corresponding discrete partition function. Here, it is worth noting that the probabilities $\widetilde{P}_1$, $\widetilde{P}_2$ and $\widetilde{P}_3 = 1 - \widetilde{P}_1 - \widetilde{P}_2$ are written as a function of two free-parameters. Thus, known the energies E_j and experimentally obtained the values of the probabilities $\widetilde{P}_j$ with $j = 1, 2, 3$, $\beta_{\rm fin}$ and λ can be derived by means of standard non-linear regression techniques. Furthermore, to make our derivation accordant with the experimental setup, we assume that the energy values are symmetric around zero, namely: $E_1 = -\bar{E}$, $E_2 = 0$ and $E_3 = \bar{E}$, with $\bar{E}$ constant value (in the experiment $\bar{E} = \omega/2$ for $\mathcal{H}_{\rm mw}$, $(\hbar = 1)$).

In this way, by substituting the relations of Eq. (5.42) into Eq. (5.40) and imposing $G(\varepsilon) = 1$, after simple calculations one ends up in the following equality corresponding to the *non-equilibrium steady-state condition* for the analyzed open 3LS:

$$Z_{\beta_{\rm in}}Z_{\beta_{\rm fin}}(\lambda) + C(\lambda)\left(3 - Z_{\beta_{\rm in}+\beta_{\rm fin}}\right) = C(\lambda)\left(Z_{(\beta_{\rm in}-\beta_{\rm fin})-2\varepsilon} + Z_{\beta_{\rm fin}+\varepsilon}\right) + C(\lambda)^4 Z_{\beta_{\rm in}-\varepsilon} \tag{5.43}$$

where

$$C(\lambda) = e^{\lambda\bar{E}^2}; \quad Z_{\beta_{\rm in}-\varepsilon} = \sum_{k=-1}^{1} e^{-k\bar{E}(\beta_{\rm in}-\varepsilon)};$$

$$Z_{\beta_{\rm fin}+\varepsilon} = \sum_{k=-1}^{1} e^{-k\bar{E}(\beta_{\rm fin}+\varepsilon)}; \quad Z_{(\beta_{\rm in}-\beta_{\rm fin})-2\varepsilon} = \sum_{k=-1}^{1} e^{-k\bar{E}((\beta_{\rm in}-\beta_{\rm fin})-2\varepsilon)}.$$

Let us observe that $\varepsilon = 0$ is always solution of Eq. (5.43) for any value of λ, while for $\lambda = 0$ the non-trivial solution ε_c of Eq. (5.43) is $\varepsilon_c = \beta_{\rm in} - \beta_{\rm fin}$ in perfect agreement with the Jarzynski-Wójcik relation [155]. Instead, for a value of $\lambda \neq 0$, Eq. (5.43) is numerically solved as a function of ε, whereby the non-trivial solution ε_c is provided by the real and positive value of ε obeying the energy exchange fluctuation relation $\langle \exp(-\varepsilon \Delta E) \rangle = 1$.

5.M Appendix: Comment on the selected time between laser pulses

In the experiments presented throughout the present chapter, the time between laser pulses was set to be $\tau = 424$ ns. The reason for this was that the Rabi frequency associated with the mw driving was $\omega/2\pi = \nu = 1.18$ MHz [Eq. (5.2)], therefore $1/(2\nu) \simeq 424$ ns. However, one must notice that this time does not corresponds to a half Rabi nutation, because of the $1/\sqrt{2}$ factor in the definition of S_x. As some sort of cheat sheet, here we include the unitary evolution operator, written in its matrix form in the S_z basis, for $\mathcal{H} = \omega S_x = \frac{\omega}{\sqrt{2}}\begin{pmatrix} 0 & 1 & 0 \\ 1 & 0 & 1 \\ 0 & 1 & 0 \end{pmatrix}$, as well as its meaning for particular cases.

$$U = e^{-i\mathcal{H}t} = \begin{pmatrix} \cos^2\theta & -\frac{i}{\sqrt{2}}\sin 2\theta & -\sin^2\theta \\ -\frac{i}{\sqrt{2}}\sin 2\theta & \cos 2\theta & -\frac{i}{\sqrt{2}}\sin 2\theta \\ -\sin^2\theta & -\frac{i}{\sqrt{2}}\sin 2\theta & \cos^2\theta \end{pmatrix} \tag{5.44}$$

with $\theta \equiv \frac{\omega t}{\sqrt{2}}$.
Simple case 1 (full period): $t = \frac{1}{\sqrt{2}\nu} \simeq 600\,\text{ns} \Rightarrow \theta = \pi \Rightarrow U = \text{Id}$

Simple case 2 (flip $m_S = \pm 1$): $t = \frac{1}{2\sqrt{2}\nu} \simeq 300\,\text{ns} \Rightarrow \theta = \frac{\pi}{2} \Rightarrow U = \begin{pmatrix} 0 & 0 & -1 \\ 0 & -1 & 0 \\ -1 & 0 & 0 \end{pmatrix}$.

Simple case 3 (half period for $m_S = 0$): $t = \frac{1}{4\sqrt{2}\nu} \simeq 150\,\text{ns} \Rightarrow \theta = \frac{\pi}{4} \Rightarrow U = \begin{pmatrix} 1/2 & -i/\sqrt{2} & -1/2 \\ -i/\sqrt{2} & 0 & -i/\sqrt{2} \\ -1/2 & -i/\sqrt{2} & 1/2 \end{pmatrix}$.

For the experiment we set $t = \frac{1}{2\nu} \simeq 424\,\text{ns} \Rightarrow \theta = \frac{\pi}{\sqrt{2}}$.

Conclusions and perspectives

The main objective of this thesis was to explore single NV spins in diamond as open quantum systems, and characterize the interaction with their own environment. The thesis was divided into two parts, in order to independently discuss two different types of couplings between the quantum system and its environment. The NV center was used as a spin qubit, or as a spin qutrit, realized by the whole set or a subset of ground-state spin projections of an NV center in diamond at room temperature. The spin degree of freedom of this system offers a high degree of control, optical initialization and readout.

In the first part of the thesis, the NV center was used to characterize the physical environment around it, formed by the nuclear spin of ^{13}C atoms randomly distributed in the diamond. Specifically, I demonstrate a protocol used for the spectral characterization of this decoherent environment. The protocol uses quantum control sequences to achieve a frequency selective dynamical decoupling (DD) from the environment, in order to reconstruct each component of the noise spectrum.

The results show that the coupling strength between the spin qubit and the spin bath gives origin to two different regimes. In the weak coupling regime, the noise spectrum of the quantum environment is modeled by a stochastic classical field with a spectral distribution centered at the ^{13}C Larmor frequency. In this regime, I demonstrated that the acquired information from the noise spectroscopy was enough to predict the dynamics of the NV spin qubit under any kind of DD sequence. In the strong coupling regime the classic description of the environment fails, due to the back action of the NV spin in the dynamics of the nuclear spin bath during the quantum control of the NV spin itself. The model can be used to describe the dynamics of the NV spin, but its predictive capabilities are not as robust as for the other regime. Finally, the same noise spectroscopy protocol was used to detect three nearby single nuclear spins. These nuclear spins were resolved from the noisy environment, and I was able to characterize their individual coupling with the NV spin.

The acquired knowledge of the decoherent environment is critical to design opportunely tailored control protocols of the spin dynamics, in order to protect the spin against noise, which is the key to prolong the NV coherence and to improve its performance in practical applications, in particular as quantum sensor of magnetic fields that is one of the most prominent quantum applications of NV centers. The predictability of the NV spin dynamics could also be combined with optimization algorithms in order to find optimal quantum control sequences that filter out the noise while increase the signal acquired by the qubit due to the interaction with a target field. This optimization algorithm could be implemented in a machine learning protocol to develop a closed-loop autonomous quantum sensors. In addition, once that the coherent coupling with nearby nuclear spins was characterized, it would be possible to use these nuclear spin as ancillary systems, opening the door for studies on how to build quantum registers [9], improve the capabilities of the quantum sensor, perform single-shot readout of the system state, and more.

The research presented in the second part of the thesis establishes the NV spin as a novel experimental platform for exploring the rapidly emerging field of experimental quantum thermodynamics. During my thesis work, I have focused on the characterization of the energy exchange between the NV spin and an engineered pseudo-thermal or purely quantum reservoir, effectively realized by driving the spin dynamics by means of short laser pulses. This study has enable the first experimental characterization of quantum fluctuation relations (FR) for an open quantum system. In practice, the dissipative map was based on the combined effect of unitary evolution, projective measurements and optical pumping mechanisms. The verification of quantum fluctuation relations was carried out by measuring the characteristic function of the spin energy variation during the thermodynamic process, which accounts for the average over a statistically relevant set of quantum trajectories (around 10^7). My experimental and theoretical findings, have brought new insight on the energy exchange mechanisms in open quantum systems.

In a two level system, the energy exchange induced by the dissipative map is completely analogous to that one induced by the interaction with a pseudo-thermal reservoir. The dissipative protocol that we have realized is compatible with a description in terms of an energy exchange fluctuation relation for pseudo-thermalizing dynamics. Such FR is defined by the inverse pseudo-temperature of the initial and asymptotic states.

In contrast with the two level system case, for a three level system under an equivalent kind of dissipative dynamics, there is no way to find an analogous pseudo-thermal reservoir that would be emulated by the dissipative map. However, as for the two level case, the interplay of projective measurements and dissipation defines a non-equilibrium stationary energy state reached by the spin qutrit for large times. I demonstrated the existence of a unique constant energy scale factor such that the characteristic function of the energy variation is time-independent. Such scaling factor, only depending on the initial and asymptotic states, defines a generalized energy exchange fluctuation relation for non-thermal dissipative dynamics. In the limit where the stationary state is a thermal state, the original FR for thermalizing dynamics [167] is recovered.

The dissipative map can be described by an intrinsic feedback process. Therefore, the energy exchange probability distribution gives origin to a generalized Jarzynski-Sagawa-Ueda (G-JSU) relation, that includes irreversible dissipation processes. I verified experimentally the validity of this FR. Moreover, using a superoperator formalism [175], I was able to recast the G-JSU relation in terms of mean trajectories, instead of single trajectories, which significantly simplifies the computation of the quantities involved in this relation. Finally, I have shown that the value of the parameters that define the FRs mentioned before, provides information on the non-unitality of the implemented stochastic dissipative dynamics.

To the best of my knowledge, this research, partially published in Refs. [19, 58], represents the first ever use of an NV center for the study of quantum fluctuation relations, thus establishing the NV center in diamond as an effective experimental platform in the rapidly-emerging field of quantum thermodynamics. In addition, this work is the first study of FRs for open quantum systems with dimensions higher than two. These kind of studies are fundamental to correctly interpret pure quantum phenomena in the field of quantum thermodynamics, in particular to study the interaction between quantum systems and reservoirs in non-equilibrium states [182, 183].

The results of my research sets the ground to further experimental studies in the field of quantum thermodynamics with diamond NV centers. A current challenge to be addressed is the exploration of processes where the system not only exchanges energy with its surroundings because of a thermal gradient, but also with an external work source. This situation is of central interest, since occurs e.g. during the operation of a heat engine. In this setting, the verification of quantum fluctuation relation poses significant difficulties, as typical quantum platforms allow to experimentally access the system energy change, but not the individual terms contribution of work and heat flux. In this respect, the flexibility of the NV center spin could be an asset to devise new schemes. Another interesting topic is the realization of a non-Gibbsian quantum heat engine [184], where quantum correlations may affect the total amount of quantum-heat during the interaction processes.

In addition, the proposed experimental protocol to measure energy variation statistics can be adjusted to one-time measurements schemes [185–187] or to quasi-probability measurements [188] in order to investigate the role of coherence in energy exchange mechanisms, with the final goal of understanding the effects of pure quantum features in thermodynamic variables. Other forms of quantum fluctuation relations based on observables that do not commute with the system Hamiltonian may be explored and measured, with potential use to investigate quantum synchronization [189] and its relation with quantum mutual information and with entanglement between the system and its dissipative environment.

Such kind of studies could also be realized for a bipartite spin system, where the characterized interaction between a single nuclear spin and the NV center electronic spin, as presented in the first part of this thesis, permits to create entangled states. Moreover, having characterized the interaction with several nearby impurities in the diamond sets the basis to implement state-of-the-art techniques to create multipartite entangled systems [22]. The high degree of control and long coherence time for such complex spin systems could represent a very useful test-bed for the relation of quantum information and quantum thermodynamics at the nanoscales.

Bibliography

[1] V. Dobrovitski, G. Fuchs, A. Falk, C. Santori, and D. Awschalom, Quantum Control over Single Spins in Diamond, Annual Review of Condensed Matter Physics **4**, 23 (2013).

[2] M. W. Doherty, N. B. Manson, P. Delaney, F. Jelezko, J. Wrachtrup, and L. C. L. Hollenberg, The nitrogen-vacancy colour centre in diamond, Phys. Rep. **528**, 1 (2013).

[3] F. Jelezko, T. Gaebel, I. Popa, A. Gruber, and J. Wrachtrup, Observation of Coherent Oscillations in a Single Electron Spin, Phys. Rev. Lett. **92**, 076401 (2004).

[4] J. Harrison, M. Sellars, and N. Manson, Optical spin polarisation of the N-V centre in diamond, Journal of Luminescence **107**, 245 (2004), proceedings of the 8th International Meeting on Hole Burning, Single Molecule, and Related Spectroscopies: Science and Applications.

[5] G. Balasubramanian, P. Neumann, D. Twitchen, M. Markham, R. Kolesov, N. Mizuochi, J. Isoya, J. Achard, J. Beck, J. Tissler, V. Jacques, P. R. Hemmer, F. Jelezko, and J. Wrachtrup, Ultralong spin coherence time in isotopically engineered diamond, Nat. Mater. **8**, 383 (2009).

[6] N. Bar-Gill, L. M. Pham, A. Jarmola, D. Budker, and R. L. Walsworth, Solid-state electronic spin coherence time approaching one second, Nat. Commun. **4**, 1743 (2013).

[7] I. Aharonovich and E. Neu, Diamond Nanophotonics, Advanced Optical Materials **2**, 911 (2014).

[8] P. Neumann, N. Mizuochi, F. Rempp, P. Hemmer, H. Watanabe, S. Yamasaki, V. Jacques, T. Gaebel, F. Jelezko, and J. Wrachtrup, Multipartite Entanglement Among Single Spins in Diamond, Science **320**, 1326 (2008).

[9] C. E. Bradley, J. Randall, M. H. Abobeih, R. C. Berrevoets, M. J. Degen, M. A. Bakker, M. Markham, D. J. Twitchen, and T. H. Taminiau, A Ten-Qubit Solid-State Spin Register with Quantum Memory up to One Minute, Phys. Rev. X **9**, 031045 (2019).

[10] L. Rondin, A. Tetienne, T. Hingant, J. F. Roch, M. P., and V. Jacques, Magnetometry with nitrogen-vacancy defects in diamond, Reports on Progress in Physics **77**, 056503 (2014).

[11] J. F. Barry, M. J. Turner, J. M. Schloss, D. R. Glenn, Y. Song, M. D. Lukin, H. Park, and R. L. Walsworth, Optical magnetic detection of single-neuron

action potentials using quantum defects in diamond, Proceedings of the National Academy of Sciences **113**, 14133 (2016).

[12] T. Wolf, P. Neumann, K. Nakamura, H. Sumiya, T. Ohshima, J. Isoya, and J. Wrachtrup, Subpicotesla Diamond Magnetometry, Phys. Rev. X **5**, 041001 (2015).

[13] F. Dolde, H. Fedder, M. W. Doherty, T. Nobauer, F. Rempp, G. Balasubramanian, T. Wolf, F. Reinhard, L. C. L. Hollenberg, F. Jelezko, and J. Wrachtrup, Electric-field sensing using single diamond spins, Nat. Phys. **7**, 459 (2011).

[14] V. M. Acosta, E. Bauch, M. P. Ledbetter, A. Waxman, L.-S. Bouchard, and D. Budker, Temperature Dependence of the Nitrogen-Vacancy Magnetic Resonance in Diamond, Phys. Rev. Lett. **104**, 070801 (2010).

[15] P. Neumann, I. Jakobi, F. Dolde, C. Burk, R. Reuter, G. Waldherr, J. Honert, T. Wolf, A. Brunner, J. H. Shim, D. Suter, H. Sumiya, J. Isoya, and J. Wrachtrup, High-Precision Nanoscale Temperature Sensing Using Single Defects in Diamond, Nano Letters **13**, 2738 (2013).

[16] M. P. Ledbetter, K. Jensen, R. Fischer, A. Jarmola, and D. Budker, Gyroscopes based on nitrogen-vacancy centers in diamond, Phys. Rev. A **86**, 052116 (2012).

[17] J. Teissier, A. Barfuss, P. Appel, E. Neu, and P. Maletinsky, Strain Coupling of a Nitrogen-Vacancy Center Spin to a Diamond Mechanical Oscillator, Phys. Rev. Lett. **113**, 020503 (2014).

[18] J. Klatzow, J. N. Becker, P. M. Ledingham, C. Weinzetl, K. T. Kaczmarek, D. J. Saunders, J. Nunn, I. A. Walmsley, R. Uzdin, and E. Poem, Experimental Demonstration of Quantum Effects in the Operation of Microscopic Heat Engines, Phys. Rev. Lett. **122**, 110601 (2019).

[19] S. Hernández-Gómez, S. Gherardini, F. Poggiali, F. S. Cataliotti, A. Trombettoni, P. Cappellaro, and N. Fabbri, Experimental test of exchange fluctuation relations in an open quantum system, Phys. Rev. Research **2**, 023327 (2020).

[20] A. Jarmola, V. M. Acosta, K. Jensen, S. Chemerisov, and D. Budker, Temperature- and Magnetic-Field-Dependent Longitudinal Spin Relaxation in Nitrogen-Vacancy Ensembles in Diamond, Phys. Rev. Lett. **108**, 197601 (2012).

[21] N. Zhao, J.-L. Hu, S.-W. Ho, J. T. K. Wan, and R. B. Liu, Atomic-scale magnetometry of distant nuclear spin clusters via nitrogen-vacancy spin in diamond. Nat. Nanotech. **6**, 242 (2011).

[22] M. H. Abobeih, J. Randall, C. E. Bradley, H. P. Bartling, M. A. Bakker, M. J. Degen, M. Markham, D. J. Twitchen, and T. H. Taminiau, Atomic-scale imaging of a 27-nuclear-spin cluster using a quantum sensor, Nature **576**, 411 (2019).

[23] N. Zhao, J. Honert, B. Schmid, M. Klas, J. Isoya, M. Markham, D. Twitchen, F. Jelezko, R.-B. Liu, H. Fedder, and J. Wrachtrup, Sensing single remote nuclear spins. Nat. Nanotech. **7**, 657 (2012).

[24] T. H. Taminiau, J. J. T. Wagenaar, T. van der Sar, F. Jelezko, V. V. Dobrovitski, and R. Hanson, Detection and control of individual nuclear spins using a weakly coupled electron spin, Phys. Rev. Lett. **109**, 137602 (2012).

[25] S. Kolkowitz, Q. P. Unterreithmeier, S. D. Bennett, and M. D. Lukin, Sensing Distant Nuclear Spins with a Single Electron Spin, Phys. Rev. Lett. **109**, 137601 (2012).

[26] J. F. Barry, J. M. Schloss, E. Bauch, M. J. Turner, C. A. Hart, L. M. Pham, and R. L. Walsworth, Sensitivity optimization for NV-diamond magnetometry, Rev. Mod. Phys. **92**, 015004 (2020).

[27] C. L. Degen, F. Reinhard, and P. Cappellaro, Quantum sensing, Rev. Mod. Phys. **89**, 035002 (2017).

[28] F. Poggiali, P. Cappellaro, and N. Fabbri, Optimal Control for One-Qubit Quantum Sensing, Phys. Rev. X **8**, 021059 (2018).

[29] G. S. Uhrig, Keeping a Quantum Bit Alive by Optimized π-Pulse Sequences, Phys. Rev. Lett. **98**, 100504 (2007).

[30] P. Rembold, N. Oshnik, M. M. Mller, S. Montangero, T. Calarco, and E. Neu, Introduction to quantum optimal control for quantum sensing with nitrogen-vacancy centers in diamond, AVS Quantum Science **2**, 024701 (2020).

[31] D. Layden and P. Cappellaro, Spatial noise filtering through error correction for quantum sensing, npj Quantum Information **4**, 30 (2018).

[32] G. Goldstein, P. Cappellaro, J. R. Maze, J. S. Hodges, L. Jiang, A. S. Sorensen, and M. D. Lukin, Environment Assisted Precision Measurement, Phys. Rev. Lett. **106**, 140502 (2011).

[33] M. H. Abobeih, J. Cramer, M. A. Bakker, N. Kalb, M. Markham, D. J. Twitchen, and T. H. Taminiau, One-second coherence for a single electron spin coupled to a multi-qubit nuclear-spin environment, Nature Communications **9** (2018).

[34] A. Cooper, W. K. C. Sun, J.-C. Jaskula, and P. Cappellaro, Identification and Control of Electron-Nuclear Spin Defects in Diamond, Phys. Rev. Lett. **124**, 083602 (2020).

[35] D. J. Evans, E. G. D. Cohen, and G. P. Morriss, Probability of second law violations in shearing steady states, Phys. Rev. Lett. **71**, 2401 (1993).

[36] G. Gallavotti and E. G. D. Cohen, Dynamical Ensembles in Nonequilibrium Statistical Mechanics, Phys. Rev. Lett. **74**, 2694 (1995).

[37] M. Esposito, U. Harbola, and S. Mukamel, Nonequilibrium fluctuations, fluctuation theorems, and counting statistics in quantum systems, Rev. Mod. Phys. **81**, 1665 (2009).

[38] M. Campisi, P. Hänggi, and P. Talkner, Colloquium: Quantum fluctuation relations: Foundations and applications, Rev. Mod. Phys. **83**, 771 (2011).

[39] J. M. R. Parrondo, J. M. Horowitz, and T. Sagawa, Thermodynamics of information, Nat. Phys. **11**, 131 (2015).

[40] J. Goold, M. Huber, A. Riera, L. del Rio, and P. Skrzypczyk, The role of quantum information in thermodynamics—a topical review, J. Phys. A: Math. Theor. **49**, 143001 (2016).

[41] R. Livi and P. Politi, *Nonequilibrium Statistical Physics: A Modern Perspective* (Cambridge: Cambridge University Press, 2017).

[42] M. Campisi, P. Talkner, and P. Hänggi, Fluctuation Theorem for Arbitrary Open Quantum Systems, Phys. Rev. Lett. **102**, 210401 (2009).

[43] D. Kafri and S. Deffner, Holevo's bound from a general quantum fluctuation theorem, Phys. Rev. A **86**, 044302 (2012).

[44] A. E. Rastegin, Non-equilibrium equalities with unital quantum channels, J. Stat. Mech. **2013**, P06016 (2013).

[45] T. Albash, D. A. Lidar, M. Marvian, and P. Zanardi, Fluctuation theorems for quantum processes, Phys. Rev. E **88**, 032146 (2013).

[46] G. Manzano, J. M. Horowitz, and J. M. R. Parrondo, Nonequilibrium potential and fluctuation theorems for quantum maps, Phys. Rev. E **92**, 032129 (2015).

[47] J. Åberg, Fully Quantum Fluctuation Theorems, Phys. Rev. X **8**, 011019 (2018).

[48] D. von Lindenfels, O. Gräb, C. T. Schmiegelow, V. Kaushal, J. Schulz, M. T. Mitchison, J. Goold, F. Schmidt-Kaler, and U. G. Poschinger, Spin Heat Engine Coupled to a Harmonic-Oscillator Flywheel, Phys. Rev. Lett. **123**, 080602 (2019).

[49] S. Toyabe, T. Sagawa, M. Ueda, E. Muneyuki, and M. Sano, Experimental demonstration of information-to-energy conversion and validation of the generalized Jarzynski equality, Nat. Phys. **6**, 988 (2010).

[50] J. V. Koski, V. F. Maisi, T. Sagawa, and J. P. Pekola, Experimental Observation of the Role of Mutual Information in the Nonequilibrium Dynamics of a Maxwell Demon, Phys. Rev. Lett. **113**, 030601 (2014).

[51] S. An, J.-N. Zhang, M. Um, D. Lv, Y. Lu, J. Zhang, Z.-Q. Yin, H. T. Quan, and K. Kim, Experimental test of the quantum Jarzynski equality with a trapped-ion system, Nat. Phys. **11**, 193 (2015).

[52] A. Smith, Y. Lu, S. An, X. Zhang, J.-N. Zhang, Z. Gong, H. T. Quan, C. Jarzynski, and K. Kim, Verification of the quantum nonequilibrium work relation in the presence of decoherence, New J. Phys. **20**, 013008 (2018).

[53] T. P. Xiong, L. L. Yan, F. Zhou, K. Rehan, D. F. Liang, L. Chen, W. L. Yang, Z. H. Ma, M. Feng, and V. Vedral, Experimental Verification of a Jarzynski-Related Information-Theoretic Equality by a Single Trapped Ion, Phys. Rev. Lett. **120**, 010601 (2018).

[54] Z. Zhang, T. Wang, L. Xiang, Z. Jia, P. Duan, W. Cai, Z. Zhan, Z. Zong, J. Wu, L. Sun, Y. Yin, and G. Guo, Experimental demonstration of work fluctuations along a shortcut to adiabaticity with a superconducting Xmon qubit, New J. Phys. **20**, 085001 (2018).

[55] F. Cerisola, Y. Margalit, S. Machluf, A. Roncaglia, J. Paz, and R. Folman, Using a quantum work meter to test non-equilibrium fluctuation theorems, Nat. Comm. **8**, 1241 (2017).

[56] T. B. Batalhão, A. M. Souza, L. Mazzola, R. Auccaise, R. S. Sarthour, I. S. Oliveira, J. Goold, G. De Chiara, M. Paternostro, and R. M. Serra, Experimental Reconstruction of Work Distribution and Study of Fluctuation Relations in a Closed Quantum System, Phys. Rev. Lett. **113**, 140601 (2014).

[57] S. Pal, T. S. Mahesh, and B. K. Agarwalla, Experimental demonstration of the validity of the quantum heat-exchange fluctuation relation in an NMR setup, Phys. Rev. A **100**, 042119 (2019).

[58] S. Hernández-Gómez, S. Gherardini, N. Staudenmaier, F. Poggiali, A. Trombettoni, M. Campisi, P. Cappellaro, F. S. Cataliotti, and N. Fabbri, Non-thermal energy fluctuations of a diamond spin qutrit with feedback-controlled dissipative dynamics, (in preparation).

[59] P. Talkner, M. Campisi, and P. Hnggi, Fluctuation theorems in driven open quantum systems, Journal of Statistical Mechanics: Theory and Experiment **2009**, P02025 (2009).

[60] M. Weissbluth, *Atoms and Molecules* (Elsevier Science, 1978) Chap. 28.4, pp. 672–677.

[61] N. B. Manson, J. P. Harrison, and M. J. Sellars, Nitrogen-vacancy center in diamond: Model of the electronic structure and associated dynamics, Phys. Rev. B **74**, 104303 (2006).

[62] N. J. Stone, Table of nuclear magnetic dipole and electric quadrupole moments, Atomic Data and Nuclear Data Tables **90**, 75 (2005).

[63] B. Smeltzer, J. McIntyre, and L. Childress, Robust control of individual nuclear spins in diamond, Phys. Rev. A **80**, 050302 (2009).

[64] M. Steiner, P. Neumann, J. Beck, F. Jelezko, and J. Wrachtrup, Universal enhancement of the optical readout fidelity of single electron spins at nitrogen-vacancy centers in diamond, Phys. Rev. B **81**, 035205 (2010).

[65] M. Pfender, N. Aslam, P. Simon, D. Antonov, G. Thiering, S. Burk, F. Fvaro de Oliveira, A. Denisenko, H. Fedder, J. Meijer, J. A. Garrido, A. Gali, T. Teraji, J. Isoya, M. W. Doherty, A. Alkauskas, A. Gallo, A. Grneis, P. Neumann, and J. Wrachtrup, Protecting a Diamond Quantum Memory by Charge State Control, Nano Letters **17**, 5931 (2017), pMID: 28872881.

[66] B. Rose, C. Weis, A. Tyryshkin, T. Schenkel, and S. Lyon, Spin coherence and 14N ESEEM effects of nitrogen-vacancy centers in diamond with X-band pulsed ESR, Diamond and Related Materials **72**, 32 (2017).

[67] M. Chen, M. Hirose, and P. Cappellaro, Measurement of transverse hyperfine interaction by forbidden transitions, Phys. Rev. B **92**, 020101 (2015).

[68] F. Poggiali, *Single nitrogen-vacancy centers in diamond for spin quantum control*, Ph.D. thesis, Università degli Studi di Firenze (2018).

[69] S. Hernández-Gómez, *ELvls.py,* `https://github.com/shgaeo/MisPys/blob/master/lens/ELvls.py` (2020).

[70] M. Hirose, *Quantum Control of Spin Systems in Diamond*, Ph.D. thesis, Department of Nuclear Science and Engineering at the Massachusetts Institute of Technology (2015).

[71] J. Wolters, M. Strauß, R. S. Schoenfeld, and O. Benson, Quantum Zeno phenomenon on a single solid-state spin, Phys. Rev. A **88**, 020101 (2013).

[72] V. Jacques, P. Neumann, J. Beck, M. Markham, D. Twitchen, J. Meijer, F. Kaiser, G. Balasubramanian, F. Jelezko, and J. Wrachtrup, Dynamic Polarization of Single Nuclear Spins by Optical Pumping of Nitrogen-Vacancy Color Centers in Diamond at Room Temperature, Phys. Rev. Lett. **102**, 057403 (2009).

[73] J.-P. Tetienne, L. Rondin, P. Spinicelli, M. Chipaux, T. Debuisschert, J.-F. Roch, and V. Jacques, Magnetic-field-dependent photodynamics of single NV defects in diamond: an application to qualitative all-optical magnetic imaging, New Journal of Physics **14**, 103033 (2012).

[74] F. Poggiali, P. Cappellaro, and N. Fabbri, Measurement of the excited-state transverse hyperfine coupling in NV centers via dynamic nuclear polarization, Phys. Rev. B **95**, 195308 (2017).

[75] L. M. Pham, N. Bar-Gill, C. Belthangady, D. Le Sage, P. Cappellaro, M. D. Lukin, A. Yacoby, and R. L. Walsworth, Enhanced solid-state multispin metrology using dynamical decoupling, Phys. Rev. B **86**, 045214 (2012).

[76] S. Hernndez-Gmez and N. Fabbri, Quantum Control for Nanoscale Spectroscopy With Diamond Nitrogen-Vacancy Centers: A Short Review, Frontiers in Physics **8**, 652 (2021).

[77] S. Hernández-Gómez, F. Poggiali, P. Cappellaro, and N. Fabbri, Noise spectroscopy of a quantum-classical environment with a diamond qubit, Phys. Rev. B **98**, 214307 (2018).

[78] S. Hernández-Gómez, F. Poggiali, P. Cappellaro, and N. Fabbri, in *Proceedings of the International School of Physics "Enrico Fermi"*, Vol. 204, Societa' Italiana di Fisica (IOS Press, 2020) pp. 245 – 249, research article.

[79] S. Hernández-Gómez, F. Poggiali, P. Cappellaro, and N. Fabbri, in *Quantum Nanophotonic Materials, Devices, and Systems 2019*, Vol. 11091, International Society for Optics and Photonics (SPIE, 2019) pp. 31 – 39.

[80] F. Poggiali, S. Hernández-Gómez, P. Cappellaro, and N. Fabbri, in *Quantum Information and Measurement (QIM) V: Quantum Technologies* (Optical Society of America, 2019) p. S3C.2.

[81] R. Kimmich and E. Anoardo, Field-cycling NMR relaxometry, Progress in Nuclear Magnetic Resonance Spectroscopy **44**, 257 (2004).

[82] S. Steinert, F. Ziem, L. T. Hall, A. Zappe, M. Schweikert, N. Gutz, A. Aird, G. Balasubramanian, L. Hollenberg, and J. Wrachtrup, Magnetic spin imaging under ambient conditions with sub-cellular resolution, Nature Communications **4**, 1607 (2013).

[83] B. A. Myers, A. Das, M. C. Dartiailh, K. Ohno, D. D. Awschalom, and A. C. Bleszynski Jayich, Probing Surface Noise with Depth-Calibrated Spins in Diamond, Phys. Rev. Lett. **113**, 027602 (2014).

[84] T. Rosskopf, A. Dussaux, K. Ohashi, M. Loretz, R. Schirhagl, H. Watanabe, S. Shikata, K. M. Itoh, and C. L. Degen, Investigation of Surface Magnetic Noise by Shallow Spins in Diamond, Phys. Rev. Lett. **112**, 147602 (2014).

[85] T. van der Sar, F. Casola, R. Walsworth, and A. Yacoby, Nanometre-scale probing of spin waves using single electron spins, Nat. Commun. **6**, 7886 (2015).

[86] A. Stark, N. Aharon, T. Unden, D. Louzon, A. Huck, A. Retzker, U. L. Andersen, and F. Jelezko, Narrow-bandwidth sensing of high-frequency fields with continuous dynamical decoupling, Nat. Commun. **8**, 1105 (2018).

[87] I. Almog, Y. Sagi, G. Gordon, G. Bensky, G. Kurizki, and N. Davidson, Direct measurement of the system-environment coupling as a tool for understanding decoherence and dynamical decoupling, J. Phys. B: At., Mol. Opt. Phys. **44**, 154006 (2011).

[88] T. Yuge, S. Sasaki, and Y. Hirayama, Measurement of the noise spectrum using a multiple-pulse sequence, Phys. Rev. Lett. **107**, 170504 (2011).

[89] G. A. Álvarez and D. Suter, Measuring the spectrum of colored noise by dynamical decoupling, Phys. Rev. Lett. **107**, 230501 (2011).

[90] S. Kotler, N. Akerman, Y. Glickman, A. Keselman, and R. Ozeri, Single-ion quantum lock-in amplifier. Nature **473**, 61 (2011).

[91] K. C. Young and K. B. Whaley, Qubits as spectrometers of dephasing noise, Phys. Rev. A **86**, 012314 (2012).

[92] L. Viola and S. Lloyd, Dynamical suppression of decoherence in two-state quantum systems, Phys. Rev. A **58**, 2733 (1998).

[93] L. Cywiński, R. M. Lutchyn, C. P. Nave, and S. DasSarma, How to enhance dephasing time in superconducting qubits, Phys. Rev. B **77**, 174509 (2008).

[94] L. Faoro and L. Viola, Dynamical suppression of $1/f$ noise processes in qubit systems, Phys. Rev. Lett. **92**, 117905 (2004).

[95] M. J. Biercuk, A. C. Doherty, and H. Uys, Dynamical decoupling sequence construction as a filter-design problem, Journal of Physics B: Atomic, Molecular and Optical Physics **44**, 154002 (2011).

[96] F. Reinhard, F. Shi, N. Zhao, F. Rempp, B. Naydenov, J. Meijer, L. T. Hall, L. Hollenberg, J. Du, R.-B. Liu, and J. Wrachtrup, Tuning a spin bath through the quantum-classical transition, Phys. Rev. Lett. **108**, 200402 (2012).

[97] N. Bar-Gill, L. Pham, C. Belthangady, D. Le Sage, P. Cappellaro, J. Maze, M. Lukin, A. Yacoby, and R. Walsworth, Suppression of spin-bath dynamics for improved coherence of multi-spin-qubit systems, Nat. Commun. **3**, 858 (2012).

[98] Y. Romach, C. Müller, T. Unden, L. J. Rogers, T. Isoda, K. M. Itoh, M. Markham, A. Stacey, J. Meijer, S. Pezzagna, B. Naydenov, L. P. McGuinness, N. Bar-Gill, and F. Jelezko, Spectroscopy of surface-induced noise using shallow spins in diamond, Phys. Rev. Lett. **114**, 017601 (2015).

[99] F. Yoshihara, Y. Nakamura, F. Yan, S. Gustavsson, J. Bylander, W. D. Oliver, and J.-S. Tsai, Flux qubit noise spectroscopy using Rabi oscillations under strong driving conditions, Phys. Rev. B **89**, 020503 (2014).

[100] S. Kotler, N. Akerman, Y. Glickman, and R. Ozeri, Nonlinear Single-Spin Spectrum Analyzer, Phys. Rev. Lett. **110**, 110503 (2013).

[101] J. T. Muhonen, J. P. Dehollain, A. Laucht, F. E. Hudson, R. Kalra, T. Sekiguchi, K. M. Itoh, D. N. Jamieson, J. C. McCallum, A. S. Dzurak, and A. Morello, Storing quantum information for 30 seconds in a nanoelectronic device, Nat Nano **9**, 986 (2014).

[102] G. A. Álvarez and D. Suter, Localization effects induced by decoherence in superpositions of many-spin quantum states, Phys. Rev. A **84**, 012320 (2011).

[103] T. Gullion, D. B. Baker, and M. S. Conradi, New, compensated Carr-Purcell sequences, J. Mag. Res. **89**, 479 (1990).

[104] E. L. Hahn, Spin Echoes, Phys. Rev. **80**, 580 (1950).

[105] H. Y. Carr and E. M. Purcell, Effects of Diffusion on Free Precession in Nuclear Magnetic Resonance Experiments, Phys. Rev. **94**, 630 (1954).

[106] S. Meiboom and D. Gill, Modified Spin-Echo Method for Measuring Nuclear Relaxation Times, Rev. Sc. Instr. **29**, 688 (1958).

[107] A. Abragam, *Principles of Nuclear Magnetism* (Oxford Univ. Press, 1961).

[108] J. M. Taylor, P. Cappellaro, L. Childress, L. Jiang, D. Budker, P. R. Hemmer, A. Yacoby, R. Walsworth, and M. D. Lukin, High-sensitivity diamond magnetometer with nanoscale resolution, Nat. Phys. **4**, 810 (2008).

[109] J. R. Maze, P. L. Stanwix, J. S. Hodges, S. Hong, J. M. Taylor, P. Cappellaro, L. Jiang, A. Zibrov, A. Yacoby, R. Walsworth, and M. D. Lukin, Nanoscale magnetic sensing with an individual electronic spin qubit in diamond, Nature **455**, 644 (2008).

[110] J. Helm, W. T. Strunz, S. Rietzler, and L. E. Würflinger, Characterization of decoherence from an environmental perspective, Phys. Rev. A **83**, 042103 (2011).

[111] D. Crow and R. Joynt, Classical simulation of quantum dephasing and depolarizing noise, Phys. Rev. A **89**, 042123 (2014).

[112] G. S. Uhrig, Exact results on dynamical decoupling by π pulses in quantum information processes, New Journal of Physics **10**, 083024 (2008).

[113] M. Hirose and P. Cappellaro, Coherent feedback control of a single qubit in diamond, Nature **532**, 77 (2016).

[114] J. Cramer, N. Kalb, M. A. Rol, B. Hensen, M. S. Blok, M. Markham, D. J. Twitchen, R. Hanson, and T. H. Taminiau, Repeated quantum error correction on a continuously encoded qubit by real-time feedback, Nature Communications **7**, 11526 (2016).

[115] H. Taminiau, J. Cramer, T. van der Sar, V. Dobrovitski, and R. Hanson, Universal control and error correction in multi-qubit spin registers in diamond, Nat Nano **9**, 171 (2014).

[116] G. Waldherr, Y. Wang, S. Zaiser, M. Jamali, T. Schulte-Herbruggen, H. Abe, T. Ohshima, J. Isoya, J. F. Du, P. Neumann, and J. Wrachtrup, Quantum error correction in a solid-state hybrid spin register, Nature **506**, 204 (2014).

[117] H. Qi, J. P. Dowling, and L. Viola, Optimal digital dynamical decoupling for general decoherence via Walsh modulation, Quantum Information Processing **16**, 272 (2017).

[118] M. J. Biercuk, H. Uys, A. P. VanDevender, N. Shiga, W. M. Itano, and J. J. Bollinger, Optimized dynamical decoupling in a model quantum memory. Nature **458**, 996 (2009).

[119] G. Quiroz and D. A. Lidar, Optimized dynamical decoupling via genetic algorithms, Phys. Rev. A **88**, 052306 (2013).

[120] D. Farfurnik, A. Jarmola, L. M. Pham, Z. H. Wang, V. V. Dobrovitski, R. L. Walsworth, D. Budker, and N. Bar-Gill, Optimizing a dynamical decoupling protocol for solid-state electronic spin ensembles in diamond, Phys. Rev. B **92**, 060301 (2015).

[121] J. Casanova, Z.-Y. Wang, J. F. Haase, and M. B. Plenio, Robust dynamical decoupling sequences for individual-nuclear-spin addressing, Phys. Rev. A **92**, 042304 (2015).

[122] A. M. Souza, G. A. Álvarez, and D. Suter, Robust Dynamical Decoupling for Quantum Computing and Quantum Memory, Phys. Rev. Lett. **106**, 240501 (2011).

[123] N. Zhao, J. Wrachtrup, and R.-B. Liu, Dynamical decoupling design for identifying weakly coupled nuclear spins in a bath, Phys. Rev. A **90**, 032319 (2014).

[124] R. Alicki and M. Fannes, Entanglement boost for extractable work from ensembles of quantum batteries, Phys. Rev. E **87**, 042123 (2013).

[125] F. Campaioli, F. A. Pollock, F. C. Binder, L. Céleri, J. Goold, S. Vinjanampathy, and K. Modi, Enhancing the Charging Power of Quantum Batteries, Phys. Rev. Lett. **118**, 150601 (2017).

[126] G. M. Andolina, M. Keck, A. Mari, M. Campisi, V. Giovannetti, and M. Polini, Extractable Work, the Role of Correlations, and Asymptotic Freedom in Quantum Batteries, Phys. Rev. Lett. **122**, 047702 (2019).

[127] H. B. Callen and T. A. Welton, Irreversibility and Generalized Noise, Phys. Rev. **83**, 34 (1951).

[128] R. Kubo, Statistical-Mechanical Theory of Irreversible Processes. I. General Theory and Simple Applications to Magnetic and Conduction Problems, Journal of the Physical Society of Japan **12**, 570 (1957).

[129] C. Jarzynski, Nonequilibrium Equality for Free Energy Differences, Phys. Rev. Lett. **78**, 2690 (1997).

[130] G. E. Crooks, Entropy production fluctuation theorem and the nonequilibrium work relation for free energy differences, Phys. Rev. E **60**, 2721 (1999).

[131] H. Tasaki, Jarzynski Relations for Quantum Systems and Some Applications, arXiv:cond-mat/0009244v2 (2000).

[132] J. Kurchan, A Quantum Fluctuation Theorem, arXiv:cond-mat/0007360v2 (2000).

[133] S. Mukamel, Quantum Extension of the Jarzynski Relation: Analogy with Stochastic Dephasing, Phys. Rev. Lett. **90**, 170604 (2003).

[134] S. Hernández-Gómez, N. Staudenmaier, M. Campisi, and N. Fabbri, Experimental test of fluctuation relations for driven open quantum systems with an NV center, arXiv:2103.03904 [quant-ph] (2021).

[135] S. Deffner and S. Campbell, Quantum Thermodynamics: An introduction to the thermodynamics of quantum information, arXiv:1907.01596 (2019).

[136] F. Binder, L. Correa, C. Gogolin, J. Anders, and G. Adesso, *Thermodynamics in the Quantum Regime: Fundamental Aspects and New Directions*, Fundamental Theories of Physics, Vol. 195 (Springer International Publishing, 2018).

[137] *Entropy, Relative Entropy, and Mutual Information,* in *Elements of Information Theory* (John Wiley & Sons, Ltd, 2005) Chap. 2, pp. 13–55, https://onlinelibrary.wiley.com/doi/pdf/10.1002/047174882X.ch2 .

[138] S. Vinjanampathy and J. Anders, Quantum thermodynamics, Contemporary Physics **57**, 545 (2016).

[139] K. Maruyama, F. Nori, and V. Vedral, Colloquium: The physics of Maxwell's demon and information, Rev. Mod. Phys. **81**, 1 (2009).

[140] J. Goold, M. Paternostro, and K. Modi, Nonequilibrium Quantum Landauer Principle, Phys. Rev. Lett. **114**, 060602 (2015).

[141] K. Jacobs, Quantum measurement and the first law of thermodynamics: The energy cost of measurement is the work value of the acquired information, Phys. Rev. E **86**, 040106 (2012).

[142] C. Elouard, D. A. Herrera-Martí, M. Clusel, and A. Auffeves, The role of quantum measurement in stochastic thermodynamics, npj Quantum Information **3** (2017), 10.1038/s41534-017-0008-4.

[143] F. Reif, *Fundamentals of Statistical and Thermal Physics* (McGraw-Hill, Inc., 1965) Chap. 9.15, pp. 383–384.

[144] Y. Morikuni and H. Tasaki, Quantum Jarzynski-Sagawa-Ueda Relations, Journal of Statistical Physics **143**, 1 (2011).

[145] M. Campisi, J. Pekola, and R. Fazio, Feedback-controlled heat transport in quantum devices: theory and solid-state experimental proposal, New Journal of Physics **19**, 053027 (2017).

[146] U. Seifert, Stochastic thermodynamics, fluctuation theorems and molecular machines, Reports on Progress in Physics **75**, 126001 (2012).

[147] F. Binder, L. Correa, C. Gogolin, J. Anders, and G. Adesso, *Thermodynamics in the Quantum Regime: Fundamental Aspects and New Directions*, Fundamental Theories of Physics, Vol. 195 (Springer International Publishing, 2018) Chap. 16, pp. 395–410.

[148] J. Liphardt, S. Dumont, S. B. Smith, I. Tinoco, and C. Bustamante, Equilibrium Information from Nonequilibrium Measurements in an Experimental Test of Jarzynski's Equality, Science **296**, 1832 (2002), https://science.sciencemag.org/content/296/5574/1832.full.pdf .

[149] D. Collin, F. Ritort, C. Jarzynski, S. B. Smith, I. Tinoco, and C. Bustamante, Verification of the Crooks fluctuation theorem and recovery of RNA folding free energies, Nature **437**, 231 (2005).

[150] F. Douarche, S. Ciliberto, A. Petrosyan, and I. Rabbiosi, An experimental test of the Jarzynski equality in a mechanical experiment, Europhysics Letters (EPL) **70**, 593 (2005).

[151] V. Blickle, T. Speck, L. Helden, U. Seifert, and C. Bechinger, Thermodynamics of a Colloidal Particle in a Time-Dependent Nonharmonic Potential, Phys. Rev. Lett. **96**, 070603 (2006).

[152] S. Ciliberto, R. Gomez-Solano, and A. Petrosyan, Fluctuations, Linear Response, and Currents in Out-of-Equilibrium Systems, Annual Review of Condensed Matter Physics **4**, 235 (2013).

[153] J. Gieseler, R. Quidant, C. Dellago, and L. Novotny, Dynamic relaxation of a levitated nanoparticle from a non-equilibrium steady state, Nature Nanotechnology **9**, 358 (2014).

[154] T. B. Batalhão, A. M. Souza, R. S. Sarthour, I. S. Oliveira, M. Paternostro, E. Lutz, and R. M. Serra, Irreversibility and the Arrow of Time in a Quenched Quantum System, Phys. Rev. Lett. **115**, 190601 (2015).

[155] C. Jarzynski and D. K. Wójcik, Classical and Quantum Fluctuation Theorems for Heat Exchange, Phys. Rev. Lett. **92**, 230602 (2004).

[156] D. Andrieux, P. Gaspard, T. Monnai, and S. Tasaki, The fluctuation theorem for currents in open quantum systems, New J. Phys. **11**, 043014 (2009).

[157] T. Sagawa and M. Ueda, Generalized Jarzynski Equality under Nonequilibrium Feedback Control, Phys. Rev. Lett. **104**, 090602 (2010).

[158] N. A. Sinitsyn, Fluctuation relation for heat engines, Journal of Physics A: Mathematical and Theoretical **44**, 405001 (2011).

[159] M. Campisi, Fluctuation relation for quantum heat engines and refrigerators, Journal of Physics A: Mathematical and Theoretical **47**, 245001 (2014).

[160] P. Talkner, E. Lutz, and P. Hänggi, Fluctuation theorems: Work is not an observable, Phys. Rev. E **75**, 050102 (2007).

[161] M. Perarnau-Llobet, E. Bäumer, K. V. Hovhannisyan, M. Huber, and A. Acin, No-Go Theorem for the Characterization of Work Fluctuations in Coherent Quantum Systems, Phys. Rev. Lett. **118**, 070601 (2017).

[162] M. Campisi, P. Talkner, and P. Hänggi, Fluctuation Theorems for Continuously Monitored Quantum Fluxes, Phys. Rev. Lett. **105**, 140601 (2010).

[163] S. Rana, S. Lahiri, and A. M. Jayannavar, Quantum Jarzynski equality with multiple measurement and feedback for isolated system, Pramana **79**, 233 (2012).

[164] S. K. Manikandan, C. Elouard, and A. N. Jordan, Fluctuation theorems for continuous quantum measurements and absolute irreversibility, Phys. Rev. A **99**, 022117 (2019).

[165] S. Gherardini, L. Buffoni, M. M. Müller, F. Caruso, M. Campisi, A. Trombettoni, and S. Ruffo, Nonequilibrium quantum-heat statistics under stochastic projective measurements, Phys. Rev. E **98**, 032108 (2018).

[166] J. Yi and Y. W. Kim, Nonequilibrium work and entropy production by quantum projective measurements, Phys. Rev. E **88**, 032105 (2013).

[167] M. Ramezani, F. Benatti, R. Floreanini, S. Marcantoni, M. Golshani, and A. T. Rezakhani, Quantum detailed balance conditions and fluctuation relations for thermalizing quantum dynamics, Phys. Rev. E **98**, 052104 (2018).

[168] M. Naghiloo, D. Tan, P. M. Harrington, J. J. Alonso, E. Lutz, A. Romito, and K. W. Murch, Heat and Work Along Individual Trajectories of a Quantum Bit, Phys. Rev. Lett. **124**, 110604 (2020).

[169] J. P. S. Peterson, T. B. Batalhão, M. Herrera, A. M. Souza, R. S. Sarthour, I. S. Oliveira, and R. M. Serra, Experimental Characterization of a Spin Quantum Heat Engine, Phys. Rev. Lett. **123**, 240601 (2019).

[170] R. J. de Assis, T. M. de Mendonça, C. J. Villas-Boas, A. M. de Souza, R. S. Sarthour, I. S. Oliveira, and N. G. de Almeida, Efficiency of a Quantum Otto Heat Engine Operating under a Reservoir at Effective Negative Temperatures, Phys. Rev. Lett. **122**, 240602 (2019).

[171] J. Roßnagel, S. T. Dawkins, K. N. Tolazzi, O. Abah, E. Lutz, F. Schmidt-Kaler, and K. Singer, A single-atom heat engine, Science **352**, 325 (2016).

[172] M. H. M. Passos, A. C. Santos, M. S. Sarandy, and J. A. O. Huguenin, Optical simulation of a quantum thermal machine, Phys. Rev. A **100**, 022113 (2019).

[173] J. Yi, P. Talkner, and G.-L. Ingold, Approaching infinite temperature upon repeated measurements of a quantum system, Phys. Rev. A **84**, 032121 (2011).

[174] M. Campisi, P. Talkner, and P. Hänggi, Influence of measurements on the statistics of work performed on a quantum system, Phys. Rev. E **83**, 041114 (2011).

[175] T. F. Havel, Robust procedures for converting among Lindblad, Kraus and matrix representations of quantum dynamical semigroups, Journal of Mathematical Physics **44**, 534 (2003).

[176] P. Strasberg, G. Schaller, T. Brandes, and M. Esposito, Quantum and Information Thermodynamics: A Unifying Framework Based on Repeated Interactions, Phys. Rev. X **7**, 021003 (2017).

[177] N. Gisin, Quantum Measurements and Stochastic Processes, Phys. Rev. Lett. **52**, 1657 (1984).

[178] K. Jacobs, *Quantum measurement theory and its applications* (Cambridge University Press, 2014).

[179] T. Sagawa and M. Ueda, Second Law of Thermodynamics with Discrete Quantum Feedback Control, Phys. Rev. Lett. **100**, 080403 (2008).

[180] G. Giachetti, S. Gherardini, A. Trombettoni, and S. Ruffo, Quantum-Heat Fluctuation Relations in Three-Level Systems Under Projective Measurements, Condensed Matter **5**, 17 (2020).

[181] B. Gardas and S. Deffner, Quantum fluctuation theorem for error diagnostics in quantum annealers, Scientific Reports **8**, 17191 (2018).

[182] R. Alicki and D. Gelbwaser-Klimovsky, Non-equilibrium quantum heat machines, New Journal of Physics **17**, 115012 (2015).

[183] W. Niedenzu, D. Gelbwaser-Klimovsky, A. G. Kofman, and G. Kurizki, On the operation of machines powered by quantum non-thermal baths, New Journal of Physics **18**, 083012 (2016).

[184] B. Gardas and S. Deffner, Thermodynamic universality of quantum Carnot engines, Phys. Rev. E **92**, 042126 (2015).

[185] S. Gherardini, A. Belenchia, M. Paternostro, and A. Trombettoni, The role of quantum coherence in energy fluctuations, arXiv:2006.06208 (2020).

[186] K. Micadei, G. T. Landi, and E. Lutz, Quantum Fluctuation Theorems beyond Two-Point Measurements, Phys. Rev. Lett. **124**, 090602 (2020).

[187] A. Sone, Y.-X. Liu, and P. Cappellaro, Quantum Jarzynski Equality in Open Quantum Systems from the One-Time Measurement Scheme, Phys. Rev. Lett. **125**, 060602 (2020).

[188] A. Levy and M. Lostaglio, Quasiprobability Distribution for Heat Fluctuations in the Quantum Regime, PRX Quantum **1**, 010309 (2020).

[189] A. Roulet and C. Bruder, Quantum Synchronization and Entanglement Generation, Phys. Rev. Lett. **121**, 063601 (2018).

Agradecimientos

Dedico esta tesis a mi esposa, Tania. Vivir contigo es una aventura, y no me queda más que agradecerte por todo. Es increíble todo lo que hemos logrado juntos.

Te amo...

Agradezco en primer lugar a mi madre, a quien amo con todo mi corazón y quien ha siempre sido para mi un ejmplo a seguir. A mi hermano, por su cariño, su amistad y por compartir conmigo incontables experiencias. A Sol y Emilio, quienes son ya parte esencial de mi vida, y a quienes quiero tanto. Y a toda mi familia, cada uno de ustedes ha sido una parte importante en mi desarrollo como persona. Si he llegado hasta donde estoy ahora, es gracias a todos ustedes.

Vorrei ringraziare Nicole, che negli ultimi tre anni è stata la guida del mio percorso accademico. A Paola per l'aiuto e la guida che mi ha dato. Ringrazio anche Nicolas, in questo breve periodo siamo diventati collaboratori, ma soprattutto amici. E a Francesco, con chi ho imparato tantissimo, ma soprattutto ti ringrazio perché mi hai subito fatto sentire a casa in un continente che non era il mio.

Voglio ringraziare anche tutti i miei amici italiani. A Matteo, Elettra, Zern e Francesco per condividere con me tanti pranzi alla mensa, che in un certo senso sono state le mie lezioni di italiano. A Tommy e Baccio, per tutte quelle serate organizzate all'improvviso. A Nicco, Bea, Elettra e Baccio, per tutte le cene che abbiamo condiviso, e per tutti i (due) trecking. A Mery, per avermi sempre preso in giro e, ovviamente, per tutte le birre che abbiamo bevuto insieme. Ringrazio anche i Bambini, che mi hanno fatto ridere tantissimo, ma soprattutto perché hanno organizzato il nostro matrimonio vero verissimo.

Agradezco también a mis *compas*, Juanfran, Luis, David, Santiago, Jero, Carlos, Andrés y Jerry. No quiero ni imaginar cómo sería mi vida si no hubiera crecido con ustedes. Están bien pinches cagados y los quiero un chingo. Y agradezco a la banda del rol, Martín, Jero, Luis, Natalia, Jerry y Tania, por tantas horas tan bien invertidas en escapar a otras realidades.

Finalmente, agradezco a mi abuela Rosa, quien siempre estuvo orgullosa de mi. Me hubiera gustado compartir este logro contigo, pero estoy seguro que nos veremos en otra vida.